TECHNISCHE
UNIVERSITÄT
WIEN
Vienna University of Technology

## Diplomarbeit

# Electrochemical reactions and transport paths of $SrTi_{0.7}Fe_{0.3}O_{3-\delta}$ thin film model electrodes in $H_2$ - $H_2O$ atmosphere

Ausgeführt am Institut für
chemische Technologien und Analytik,
Fachbereich Elektrochemie
der Technischen Universität Wien

Unter Anleitung von
Univ.Prof.Dipl.Phys.Dr. Jürgen Fleig
und Dipl.Ing. Dr.techn. Alexander Opitz

Durch
Andreas Nenning
Trubelgasse 7/18 1030 Wien

Abgegeben: 10. Dezember 2012

# Vorwort

Im Gegensatz zum irreführenden Namen dieses Kapitels stehe ich nun vor den letzten Zeilen meiner Arbeit. Ich führe diese Worte dennoch oben an, um den Leser dieses Werkes vorab wohlgesonnen zu stimmen. Aus diesem Grunde bedanke ich mich gesondert bei dir, lieber Leser, für dein Interesse an der schwierigen Materie der Festkrperelektrochemie und meiner Arbeit, und wünsche dir frohen Mut beim durchkauen der folgenden Kapitel.
Ich möchte mich generell bedanken für die fröhliche und lehrreiche Zeit, die mir in der Arbeitsgruppe Festkörperelektrochemie ermöglicht wurde.
Mein besonderer dank gilt zudem:

Jürgen Fleig, der mir die Forschung an Festoxidbrennstoffzellenreaktionen mit moderner Ausrüstung, viel persönlicher Gestaltungsfreiheit und engagierter Betreuung ermöglicht hat. Auch für die gesponsorte Teilnahme an der E-MRS 2012, möchte ich meinen Dank aussprechen.

O Co-Captain! My Co-Captain! - Ja Alex du bist gemeint. Auch dir gilt mein besonderer Dank für deine verlässliche Hilfsbereitschaft und deinen fundierten fachlichen Rat sowie dein freundliches und offenes Gemüt. Dankbar bin ich auch für die Unterstützung bei vielen Experimenten und in der nicht immer leichten Interpretation meiner Messungen, und die durchgeführten REM und XRD Messungen.

Außerdem möchte ich mich bei Martin Ahrens für die Einschulung an PLD, Ionenstrahlätzanlage und Lithographie, bedanken. Danke auch an Claudia Hradil für die Aufnahme der XRD Spektren, sowie Elisabeth Eitenberger für die Elektronenmikroskopaufnahmen am USTEM, sowie der Firma Rose für die Anfertigung der Fotomaske. Danke auch an Tobias Huber für den Bau und die Instandhaltung vieler Laborgeräte.

Ein großes Dankeschön auch an meine Bürokollegen Sandra (für Hilfe während meiner Einarbeitungszeit und lehrreiche sowie erheiterne Gespräche), Christoph (für hervorragenden kulinarischen Input), Lukas und Edvinas, sowie der gesamten Arbeitsgruppe aus Tobias, Tschisi, Markus,

Steffi, Georg, Gerald (beide), Christoph (der Andere), Hinnerk, Andreas, Sebastian, Dominik, Gregor und Bernhard, sowie bei jenen, die ich vergessen habe hier anzuführen.

Für die Rettung aus den Mühlen der Bürokratie, und die Betreuung der Laborgeräte und Gasflaschen bedanke ich mich bei Udo, Kurt Judith und Eva.

Ein kollektives Dankeschön geht auch an das Arbeitsklima und die Offenheit und Hilfsbereitschaft von jedem einzelnen, mit dem ich das Vergnügen hatte zu arbeiten.

# Abstract

$SrTi_{1-x}Fe_xO_{3-\delta}$ is a perovskite type mixed conductor with relatively low electronic conductivity, compared to other mixed conducting electrode materials such as Sr-doped $LaMnO_{3-\delta}$ (LSM) or $LaCoO_{3-\delta}$ (LSC). Nevertheless, it shows a highly catalytic surface for the Solid Oxide Fuel Cell (SOFC) cathode reaction. Its high stability under reducing conditions makes it also principally applicable as a SOFC anode or SOEC cathode. For potential practical application, high electrochemical surface activity, as well as electronic and ionic conductivity, chemical stability and low degradation are crucial. In order to investigate these properties, geometrically well defined thin film microelectrodes of $SrTi_{0.7}Fe_{0.3}O_{3-\delta}$ have been deposited on single crystalline yttria-stabilized zirconia substrates via pulsed laser deposition and photolithographic techniques. To achieve sufficient lateral electronic transport within the film, a thin film platinum grid was deposited on top or beneath the electrode. The electro- and defect chemical properties of these microelectrodes were investigated by means of impedance and DC-bias measurements as function of temperature in $H_2$-$H_2O$ atmosphere. Under equilibrium conditions, the electrode resistance is dominated by the electrochemical surface reaction. By applying a specific electrode and metal grid design with two separated metal structures on one microelectrode, the surface reaction rate, electronic and ionic conductivity as well as chemical capacitance can be identified on a single microelectrode. The results are discussed in terms of electronic and ionic defect models in solids.

# Kurzfassung

$SrTi_{1\text{-}x}Fe_xO_{3\text{-}\delta}$ (STFO) ist ein gemischter Leiter in Perovskitstruktur mit geringer elektronischer Leitfähigkeit, verglichen mit anderen häufig untersuchten gemischten Leitern (z.B. Sr-dotiertes $LaMnO_{3\text{-}\delta}$ (LSM) oder $LaCoO_{3\text{-}\delta}$ (LSC)). In Sauerstoffatmosphäre ist die Elektrodenkinetik jedoch für eine potentielle Anwendbarkeit als SOFC (Solid Oxide Fuel Cell) Kathode ausreichend. Da STFO auch in reduzierender Atmosphäre hohe chemsche Stabilität aufweist, ist es prinzipiell auch als Anodenmaterial verwendbar. Für eine mögliche Anwendung sind hohe elektronische und ionische Leitfähigkeit, sowie eine katalytisch aktive Oberfläche und geringe Degradation entscheidende Parameter. Um diese Parameter zu bestimmen, wurden Dünnschicht-Modellelektroden mit definierter Geometrie und Oberfläche untersucht. Dünnfilme aus $SrTi_{0.7}Fe_{0.3}O_{3\text{-}\delta}$ wurden mit *Pulsed Laser Deposition* auf einkristallinen Yttrium-stabilisierten Zirkoniumoxid Substraten abgeschieden, und anschließend photolithographisch mikrostrukturiert. Ein Dünnfilm Platin-Gitter wurde ober- oder unterhalb der Elektroden aufgetragen, um eine ausreichende Verteilung der Elektronen, trotz geringer elektronischer Leitfähigkeit, zu gewährleisten. In $H_2$-$H_2O$ - Atmosphäre wurden die elektrochemischen Eigenschaften und Defektkonzentrationen dieser Mikroelektroden mit Impedanzspektroskopie und Gleichstrommessungen untersucht. Im thermodynamischen Gleichgewicht ist die elektrochemische Wasserspaltungsreaktion ratenbestimmend. Eine für die Untersuchung von Mikroelektroden optimiertes Design von Metallgitter und Mikroelektroden mit zwei getrennten Metallstrukturen pro Elektrode wurde verwendet. Mit dieser Elektrodengeometrie können elektronische und ionische Leitfähigkeit, sowie die Reaktionsrate der Wasserspaltungsreaktion, und die chemische Kapazität an nur einer Mikroelektrode bestimmt werden.

# Contents

# 1 Introduction

The increasing amount of renewable electric power generation (e.g. wind, solar) causes large fluctuations and sometimes even excess in electricity generation, which leads to the need of large electric storage capacity and fast adjustment of conventional/fossil power generation [1, 2]. Reversible Solid Oxide Fuel/Electrolysis Cells (SOFCs/SOECs) are promising candidates in this field of application [3]. They offer high electrical efficiency and chemical energy storage with large capacity.

Different fuel cell types are characterised by their electrolyte materials. Most fuel cell types use a liquid electrolyte, which is conductive either for $H^+$ (Phosphoric Acid Fuel Cell (PAFC), Alkaline Fuel Cell (AFC)) or $O^{2-}$ (Molten Carbonate Fuel Cell (MCFC)) ions. Polymer Exchange Membrane Fuel Cells (PEMFCs) have a solid polymer electrolyte (typically Nafion®), but the $H^+$ conduction takes place in micro-channels filled with water. Therefore the electrolyte can either be considered solid (in mechanical terms) or liquid (in electrochemical terms).

SOFCs use a ceramic electrolyte instead, typically Yttria Stabilised Zirconia (YSZ). By doping the $ZrO_2$ crystal with $Y_2O_3$, oxygen vacancies are created. The exact mechanism is explained in section 2.3. At temperatures above approximately 500 °C, these vacancies become sufficiently mobile to enable the oxygen current density needed in a commercial fuel cell with a thin electrolyte. SOFCs exhibit some advantages over fuel cells with liquid electrolytes. The high operating temperature offers good catalytic activity without the need of expensive materials, like platinum. Also, relatively high tolerance to some catalyst poisons can be achieved, and a wide range of fuels can be processed [4, 5]. Since the oxygen ions are mobile in the electrolyte, theoretically any fuel can be used for electricity generation. This work is attributed to the anode hydrogen fuel, with the net reaction:

$$H_2 + \frac{1}{2}O_2 \rightleftharpoons H_2O \tag{1.1}$$

This is split into the half-cell reactions

$$Cathode: \quad \frac{1}{2}O_2 + 2e^- \rightleftharpoons O^{2-} \tag{1.2}$$

$$Anode: \quad O^{2-} + H_2 \rightleftharpoons 2e^- + H_2O \tag{1.3}$$

In mixed conducting anodes, electrons and oxygen ions are mobile, which principally allows oxygen exchange at the entire electrode surface (If the mobility of electrons and ions is sufficient for the given electrode geometry.) The recent development goes towards reduced operating temperature around 500-600 °C, compared to 900-1000 °C for some currently commercial systems. The goal is to achieve longer lifetime and enable the use of cheaper materials. Also, the equilibrium cell voltage, and therefore the theoretical efficiency increases at lower temperatures (see section 2.1). This results in the need of new electrode materials with high performance at lower temperature. Mixed conducting perovskite cathodes are believed to show high potential of application in solid oxide fuel cells and sufficient reactivity also for intermediate temperature applications. Some of these materials have high chemical stability under reducing conditions, which principally makes them also applicable as fuel cell anodes. Phenomenological studies on porous $(La_{0.75}Sr_{0.25})(Cr_{0.5}Mn_{0.5})O_{3-\delta}$(LSCM) anodes have been carried out [6, 7], where a low area specific resistance and high redox-cycle stability was demominstrated, but the reaction mechanism of water splitting and the rate limiting step could not be identified. Also mechanistic studies on samaria doped ceria (SDC) thin film anodes with platinum and nickel current collectors have been made [8]. For this setup, the site of catalytic activity could be identified to be the mixed conducting surface, and not the triple phase boundary. Fundamental investigations of relevant electrochemical as well as defect chemical parameters on different mixed conducting anode materials are therefore of high relevance for a mechanistic interpretation of the surface reaction as well as for an optimisation of commercial electrode designs.

In fundamental research, porous electrodes are difficult to investigate, since the effective surface area is hard to determine and the electrochemical transport and reaction paths are complicated, and not well known. Thin film electrodes in contrast offer well defined geometry and surface area, simple transport paths and good reproducibility. So, even though they are far away from a practically applicable electrode design, they offer better insight into the fundamental reactions taking place.

$SrTi_{1-x}Fe_xO_{3-\delta}$, a cubic perovskite with high stability in reducing atmosphere and mixed conduction, may be a promising SOFC anode material. It has already been investigated as a cathode material, revealing a highly catalytic surface in oxygen atmosphere [9]. Also mechanistic studies have been made [10, 11] for the cathodic oxygen reduction, but detailed studies on the performance as a fuel cell anode and investigation of the electrochemical reactions and defect chemistry on thin film model electrodes in $H_2$-$H_2O$ atmosphere have not been carried out so far.

For this work, thin films of the composition $SrTi_{0.7}Fe_{0.3}O_{3-\delta}$ with thickness ranging from 100 to 400 nm have been prepared on single crystalline YSZ substrates with pulsed laser deposition (PLD). Microelectrodes were produced via photolithographic techniques and ion beam etching. A thin film platinum grid was applied on top or beneath the electrode to serve as an electronic current collector. This work focusses on the identification and separation of individual elementary processes, which contribute to the polarisation resistance of thin film model electrodes in $H_2$–$H_2O$ atmosphere, which is measured by electrochemical impedance spectroscopy. In combination with a specifically designed microelectrodes and metal grid, crucial electrode parameters, such as electronic, and ionic conductivity and surface reaction rate can be measured on one single electrode.

# 2 Defect chemistry and thermodynamics of mixed conductors

The electronic, cationic and anionic conductivity of electroceramics is governed by the number and mobility of defects in the crystal structure. Mixed ionic and electronic conductors exhibit high ionic as well as electronic conductivity, which is achieved by generation of a large amount of mobile electronic defects and oxygen vacancies.

## 2.1 Thermodynamics of a hydrogen fuel cell

Under equilibrium conditions (i.e. no current is flowing), the cell voltage ($U_{cell}$) for a fuel/electrolysis cell is only depending on the change in Gibbs free energy ($\Delta_R G$) of the net reaction. Half cell reactions must not play a role due to the independence of thermodynamic potential changes to the reaction mechanism.

$$H_2 + \frac{1}{2}O_2 \longrightarrow H_2O$$

$$\begin{aligned} \Delta_R G &= -z_e F U_{cell} \\ U_{cell} &= -\frac{\Delta_R G}{z_e F} \\ U_{cell} &= -\frac{\Delta_R H - T\Delta_R S}{z_e F} \end{aligned} \tag{2.1}$$

- $\Delta_R H$, $\Delta_R S$: Reaction enthalpy and entropy change at cell temperature
- $z_e$: Number of elementary charge carriers (=2)
- $T$: Temperature
- $F$: Faraday constant

The specific reaction enthalpy and the specific reaction entropy are depending on the temperature. These dependences can be calculated by using

| $\Delta_R H^0$ | $S^0(H_2O)$ | $S^0(H_2)$ |
|---|---|---|
| $-285.8\,\mathrm{kJmol^{-1}}$ | $130.7\,\mathrm{Jmol^{-1}K^{-1}}$ | $205.1\,\mathrm{Jmol^{-1}K^{-1}}$ |

| $c_p(H_2O)(g)$ | $c_p(H_2)$ | $c_p(O_2)$ |
|---|---|---|
| $37.8\,\mathrm{Jmol^{-1}K^{-1}}$ | $29.01\,\mathrm{Jmol^{-1}K^{-1}}$ | $31.6\,\mathrm{Jmol^{-1}K^{-1}}$ |

| $S^0(O_2)$ | $c_p(H_2O)(l)$ | $\Delta H_{vap}(H_2O)$ |
|---|---|---|
| $69.9\,\mathrm{Jmol^{-1}K^{-1}}$ | $75.24\,\mathrm{Jmol^{-1}K^{-1}}$ | $42.91\,\mathrm{kJmol^{-1}}$ |

Table 2.1: Relevant material constants for the calculation of the equilibrium cell voltage.

the theoretical reaction path: cooling to standard temperature - chemical reaction - heating to operating temperature.

$$dH = c_p dT \tag{2.2}$$

$$dS = \frac{c_p dT}{T} \tag{2.3}$$

$$\Delta_R S = \Delta_R S^0 + \sum_i \nu_i \int\limits_{T_0}^{T_{cell}} \frac{c_{p,i}}{T} dT = \int\limits_{T_0}^{T_{cell}} \frac{c_p(H_2O) - (0.5c_p(O_2) + c_p(H_2))}{T} dT \tag{2.4}$$

$$\Delta_R H = \Delta_R H^0 + \sum_i \nu_i \int\limits_{T_0}^{T_{cell}} c_{p,i} dT = \int\limits_{T_0}^{T_{cell}} c_p(H_2O) - (0.5c_p(O_2) + c_p(H_2)) dT \tag{2.5}$$

$$\eta_{fc} = \frac{\Delta_R G}{\Delta_R H^0} \tag{2.6}$$

- $c_{p,i}$ Specific heat capacity at constant pressure of reactant i
- $\nu_i$ Stoichiometric coefficient of reactant i
- $\eta_{fc}$ Theoretical efficiency of a hydrogen fuel cell at a given temperature.
- $\Delta_R H^0$ and $\Delta_R S^0$: Reaction enthalpy and entropy change at standard conditions (25°C, 1013 mbar)

The values for reaction enthalpy and entropy, as well as the specific heat capacities were taken from the standard literature [12]. The reaction entropy change for water generation (liquid or steam) is negative, which means that

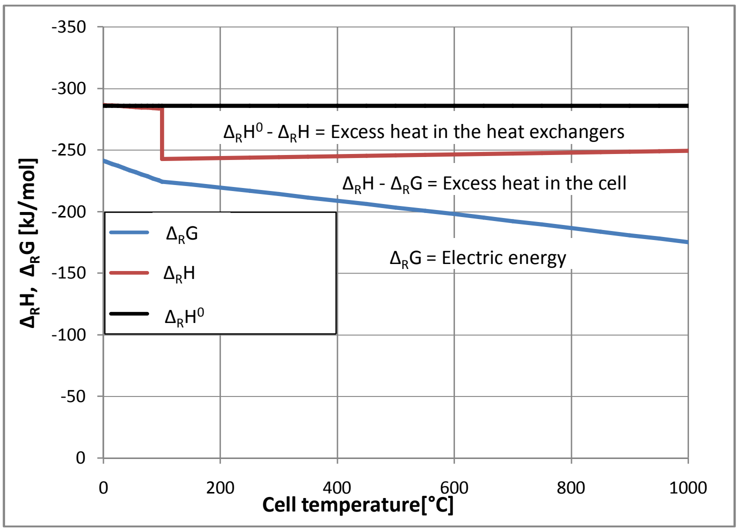

Figure 2.1: Reaction enthalpy and entropy of a hydrogen fuel cell as function of temperature.

the absolute of $\Delta_R G$ is smaller than the absolute of $\Delta_R H$. The temperature dependence of reaction entropy and reaction enthalpy is shown in figs. 2.1 and 2.2. At 100 ℃ the reaction enthalpy is reduced by the vaporisation enthalpy of water. However, the Gibbs free energy values of liquid and gas phase are equal at the boiling point, therefore the cell potential remains continuous.

The enthalpy difference $\Delta_R H^0 - \Delta_R H$ is equal to the excess heat in the gas inlet/outlet heat exchangers, since products and educts are normally stored at room temperature. The difference $\Delta_R H - \Delta_R G$ is the amount of (reversible) heat generated even in a lossless cell. This concludes, that the theoretical efficiency of a hydrogen fuel cell is 83% at 25 ℃, or 70% at 500 ℃. Nevertheless, the better kinetics at high temperature usually overcompensate the thermodynamic disadvantages.

Since the fuel cell reaction is fully reversible, the theoretical electrical efficiency of an electrolysis cell is given by $\eta_{ec} = 1/\eta_{fc}$ , which is around 143% at 500 ℃. In this case a non-electric heat source has to be available to maintain the cell temperature. If no other heat source is available, the electrical input energy has to be equal to the nominal reaction enthalpy,

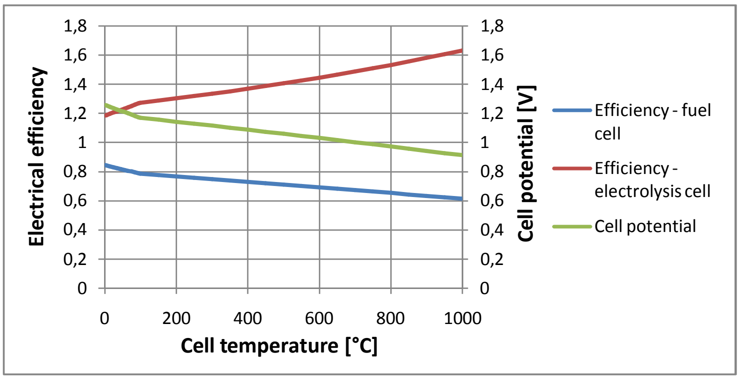

Figure 2.2: Theoretical efficiency and equilibrium voltage of a fuel cell without overpotential losses.

$\Delta_R H^0 = -z_e F U_{cell}$, in order to maintain the operating temperature. Therefore an electrolysis cell with considerable internal polarisation and transport losses can still achieve an electrical efficiency of 100%, compared to the upper caloric value of the hydrogen produced. For example the equilibrium cell voltage of an electrolysis cell at 500 °C is 1.04V, whereas the needed voltage to maintain the temperature is 1.48V, resulting in 0.44 V required overpotential.

### 2.1.1 Oxygen partial pressure as function of atmosphere and DC-bias

When a (thin film) fuel cell electrode has high electronic and ionic conductivity, transport losses are small, and the surface reaction is the rate limiting step. If this is the case, an applied electrical voltage causes a stoichiometric polarisation of the electrode bulk.

Under equilibrium conditions the chemical potential of products and educts of the oxygen exchange reaction has to be equal.

$$O_2 + 4e^- \rightleftharpoons 2O^{2-} \;\Rightarrow\; \mu^g_{O_2} = 2\mu_{O^{2-}} - 4\mu_{e^-} \tag{2.7}$$

$\mu^g_{O_2}$ and $p^g_{O_2}$ are the chemical potential and partial pressure of oxygen in the gas phase. Let us consider a working and counter electrode in the same gas atmosphere. When no bias is applied, full thermodynamic equilibrium will be reached. When the surface reaction of the working electrode is blocked, no steady state current will flow when a voltage ($\eta$) is applied to the working electrode (the counter electrode remains on zero potential). To calculate the oxygen partial pressure in the electrode, a chemical potential of molecular oxygen in the electrode has to be introduced:

$$\mu^{el}_{O_2} := 2\mu_{O^{2-}} - 4\mu_{e^-} = 2\tilde{\mu}_{O^{2-}} - 4\tilde{\mu}_{e^-} \qquad \Delta\mu^{el}_{O_2} = \mu^{el}_{O_2} - \mu^{g}_{O_2} \tag{2.8}$$

When a voltage is applied, the electrochemical potential of electrons in the electric contact is changed by $-F\eta$. This is also, the change in the electrochemical potential of electrons in the electrode ($\Delta\tilde{\mu}_{e^-} = -F\eta$).

The electrochemical potential of oxygen ions, on the other hand, is conductively connected with the counter electrode (which is still in equilibrium with the gas), and therefore remains unchanged($\Delta\tilde{\mu}_{O^{2-}} = 0$). This leads to stoichiometric polarisation.

$$\Delta\tilde{\mu}_{O^{2-}} = 0 \tag{2.9}$$

$$\Delta\tilde{\mu}e^{-} = -F\eta \tag{2.10}$$

$$\Delta\mu^{el}_{O_2} = 2\Delta\tilde{\mu}_{O^{2-}} - 4\Delta\tilde{\mu}_{e^-} = 4F\eta \tag{2.11}$$

$$\mu^{el}_{O_2} = \mu^{g}_{O_2} + RTln(\frac{p^{el}_{O_2}}{p^{g}_{O_2}}) \tag{2.12}$$

$$p^{el}_{O_2} = p^{g}_{O_2}e^{\frac{4F\eta}{RT}} \tag{2.13}$$

$p^{el}_{O_2}$ is the (associated) partial pressure in the electrode bulk, which describes the electrode bulk parameters, such as oxygen vacancy and electronic defect concentrations (and conductivity). The stoichiometric polarisation can therefore be understood as a step in the electrochemical potential of oxygen between the gas phase and the electrode. This step is not associated with an electrostatic potential, since the gas atmosphere is an insulator and therefore has no defined electric potential.

In the case of $H_2 - H_2O$ atmosphere, the oxygen partial pressure in the gas can be calculated by the mass-action law. This, combined with equation 2.13, can be used for an exact calculation of $p^{el}_{O_2}$. Thermodynamically, these equations are exact (in the case of a blocked working electrode), even though neither in hydrogen gas atmosphere nor in the electrode, a single $O_2$ molecule can be found.

$$\frac{p_{H_2O}}{p_{H_2}\sqrt{p_{O_2}}} = K_{eq} = e^{\frac{\Delta_R G}{RT}} \tag{2.14}$$

$$p^{g}_{O_2} = e^{\frac{2\Delta_R G}{RT}} \left(\frac{p_{H_2O}}{p_{H_2}}\right)^2 \tag{2.15}$$

$$p^{el}_{O_2} = e^{\frac{2\Delta_R G+4F\eta}{RT}} \left(\frac{p_{H_2O}}{p_{H_2}}\right)^2 \tag{2.16}$$

Here, $\Delta_R G$ is the Gibbs free energy change of the water generation reaction, when all gasses are at standard pressure (but not necessarily at standard temperature), according to equation 2.1. When the electrode surface does allow oxygen exchange, overpotential losses will also occur due to transport reactions (ionic transport through the electrolyte, etc.). To calculate the stoichiometric polarisation of the electrode bulk, these losses have to be measured (typically over impedance spectroscopy) and subtracted from the applied voltage. A detailed discussion on transport losses will be made in section 5.1

However, the surface adsorbate coverage and space charge potential may still be linked to the gas atmosphere, which is hard to determine experimentally [13].

## 2.2 The perovskite structure

This crystal structure is named after the crystal $CaTiO_3$, with trivial name *perovskite*. The elementary cell, $ABO_3$, consists of large $2^+$ charged (for strontium titanate) *"A-site cations"* at the corner positions, small $4^+$ charged (for strontium titantate) *"B-site cations"* at the body center position and $2^-$ charged Oxygen ions at the face centered positions. Perovskites exist in several different lattice point groups. The most simple is the cubic group, which is the case for $SrTiO_{3-\delta}$, or STFO. If the ionic radii do not exactly match the requirements of the crystal structure, the lattice is distorted, and pseudocubic tetragonal, orthorombic, rhomboedric structures are formed. Perovskites of different compositions exhibit several very interesting quantum-electronic phenomena, such as Colossal magnetoresistance [14], superconductivity, etc. However, for mixed conducting electrodes, the ionic and electronic defect structure and conductivity, as well as the catalytic activity for surface oxygen exchange are of preferential interest.

## 2.3 Point defects

Point defects can be of intrinsic (thermodynamically activated in a perfectly stoichiometric crystal) and extrinsic (introduced by doping) nature. In mixed conductors, the high doping level leads to predominantly extrinsic defects [15]. The defects are written in Kröger-Vink notation [16]. The reactions written below do not describe a reaction mechanism, but are used to calculate the defect concentrations in local thermodynamic equilibrium. Due to the high dopant concentration, defect-defect interactions can not be neglected, which makes an exact thermodynamic description of a typical mixed conducting electrode difficult. The thermodynamically exact calculation of the chemical potential of defects is taking into account the (concentration depending) free formation enthalpy, and configurational entropy. For small concentrations, this equation can be simplified. [15]:

$$\mu = \mu_0(c) + RT \ln\left(\frac{c}{c_0}\right) \approx \mu_0(c=0) + RT\ln(\frac{c}{c_0}) \quad c \ll c_0 \tag{2.17}$$

Here, $\mu_0$ is the free formation enthalpy without configurational entropy and $c_0$ is the density of possible lattice sites for defects (or effective density of states for delocalised defects [17]). In the case of gases and liquids, $c_0$ refers to the standard conditions. For high defect concentrations, interactions can not be neglected, and $\mu_0$ becomes a function of the defect concentration. In some cases, the $\mu(c)$ dependence for higher concentrations can be expressed by introduction of a concentration-dependent activity $a(c)$

$$\mu = \mu_0(c) + k_bT \ln\left(\frac{c}{c_0}\right) := \mu_0(c=0) + k_bT\ln(a(c)) \tag{2.18}$$

$$\lim_{c\to 0} a(c) = \frac{c}{c_0} \tag{2.19}$$

In the case of solid state electrochemistry, the function $a(c)$ is difficult to determine, because it is not possible to change one single defect concentration. They are linked over defect equilibria, and can not be changed individually. [13].

### 2.3.1 Intrinsic defects

Intrinsic defects occur even in perfectly stoichiometric crystals due to thermal activation. Some common intrinsic defects are:

- Electron-hole generation: $null \rightleftharpoons e^{'} + h^{\bullet} \quad K_{e-h} = [e^{'}][h^{\bullet}]$
- Frenkel disorder: $O_O^{\times} \rightleftharpoons V_O^{\bullet\bullet} + O_i^{''} \quad K_{frenkel} = \dfrac{[V_O^{\bullet\bullet}][O_i^{''}]}{[O_O^{\times}]}$
- Schottky disorder: $null \rightleftharpoons V_O^{\bullet\bullet} + V_{Me}^{''} \quad K_{schottky} = [V_O^{\bullet\bullet}][V_{Me}^{''}]$
- Electron trapping in oxygen vacancies: $V_O^{\bullet\bullet} + e^{'} \rightleftharpoons V_O^{\bullet} \quad K_{trap} = \dfrac{[V_O^{\bullet}]}{[V_O^{\bullet\bullet}][e^{'}]}$

Several other intrinsic defect types may also occur, such as interstitial cations, antisite defects,... However, in SOFC applications, intrinsic defects usually play a minor role, because the majority of defects is extrinsic due to the high doping amount. Only the electron-hole generation may play an important role in the oxygen reduction reaction (in oxygen atmosphere), according to [10, 11].

### 2.3.2 Extrinsic defects

Extrinsic defects are quantitatively dominant in mixed conducting ceramics, introduced by the high dopant amount. Due to the large amount of doping possibilities and corresponding defect reactions, only the relevant defects in acceptor doped ceramics (e.g. STFO) will be discussed.

- Oxygen reduction reaction : $\frac{1}{2}O_2 + V_O^{\bullet\bullet} \rightleftharpoons 2h^{\bullet} + O_O^{\times} \quad K_{red} = \dfrac{[h^{\bullet}]^2[O_O^{\times}]}{[O_2]^{\frac{1}{2}}[V_O^{\bullet\bullet}]}$
- Dopant ionisation 1: $Fe_{Ti}^{\times} \rightleftharpoons Fe_{Ti}^{'} + h^{\bullet} \quad K_{ion,1} = \dfrac{[Fe_{Ti}^{'}][h^{\bullet}]}{Fe_{Ti}^{\times}}$
- Dopant ionisation 2: $Fe_{Ti}^{'} \rightleftharpoons Fe_{Ti}^{''} + h^{\bullet} \quad K_{ion,2} = \dfrac{[Fe_{Ti}^{''}][h^{\bullet}]}{Fe_{Ti}^{'}}$

The oxygen reduction reaction can not be exactly described as intrinsic or extrinsic, because it is leading to a non-stoichiometric crystal, but also occurs in undoped systems.

### 2.3.3 Conservation laws

The three extrinsic defect reactions and electron-hole generation involve six defect species $V_O^{\bullet\bullet}, Fe_{Ti}^{\times}, Fe_{Ti}^{'}, Fe_{Ti}^{''}, h^{\bullet}, e^{'}$, and four equilibrium constants. To calculate the thermodynamic defect equilibrium (when the equilibrium constants are known), additional boundary conditions are necessary.

- Charge neutrality condition: $2[V_O^{\bullet\bullet}] + [h^{\bullet}] - [Fe_{Ti}^{'}] - 2[Fe_{Ti}^{''}] - [e^{'}] = 0$
- Mass conservation: $[Fe_{Ti}^{\times}] + [Fe_{Ti}^{'}] + [Fe_{Ti}^{''}] = [Fe_{Ti}]_{tot}$

In many mixed conductors, such as LSF [18], the dopant ions are almost fully *"ionised"* (carrying one less positive charge, compared to the host lattice). This leads to excess negative charge, which has to be compensated with positively charged defects (charge neutrality condition). Pure ionic conductors, such as YSZ or Gadolinium Doped Ceria (GDC) [19], are charge-compensated by the formation of oxygen vacancies. In pure electronic conductors, the dopant ionisation is mainly compensated by formation of holes in the valence band, whereas the number of oxygen vacancies is small, compared to the number of dopant ions. Such a material can exhibit near metal-like electronic conductivity. When both compensation mechanisms occur in similar amount, the material is a mixed ionic and electronic conductor. If the according mass-action constants are known, the defect concentration can be calculated for weakly doped systems. However, in highly doped ceramics, defect-interactions can not be neglected, and the $\mu_0(c)$ function has to be determined for an exact calculation of the defect concentrations. This is hardly possible in solid state electrochemistry. For example, the large number of additional electrons in the Fe$^{3+}$ state is proposed to form an own energy band [20]. For strontium titanate, one approximation is possible: the very low electronic conductivity implies a low concentration of holes and electrons, leading to nearly fully ionic charge compensation. Also, the amount of Fe$^{2+}$ ($Fe_{Ti}^{''}$) is comparatively small, when no bias voltage is applied.

$$[h^{\bullet}] \ll [V_O^{\bullet\bullet}] \quad \rightarrow \quad [V_O^{\bullet\bullet}] \approx \frac{1}{2}[Fe_{Ti}^{'}] \tag{2.20}$$

With this assumed approximation, the dopant ionisation and reduction reaction can be simplified to:

- Reduction reaction 2: $\frac{1}{2}O_2 + V_O^{\bullet\bullet} + 2Fe_{Ti}^{'} \rightleftharpoons 2Fe_{Ti}^{\times} + O_O^{\times}$

### 2.3.4 Chemical capacitance

The chemical capacitance of a mixed conductor is a materials property, that is proportional to the change in oxygen vacancy concentration by application of an electrical overpotential. According to [21], the partial chemical capacitance per unit volume of one charge carrier species can be described as:

$$C_{chem,j} = (ez)^2 \left( \frac{\partial \mu_j}{\partial c_j} \right)^{-1} \tag{2.21}$$

When the defect concentration $\mathrm{c_j}$ is small, the chemical capacitance is directly proportional to the concentration:

$$\mu_j = \mu_j^0 \, k_b T \ln \left( \frac{c_j}{c_{0,j}} \right) \tag{2.22}$$

$$C_{chem,j} = c_j \left( \frac{(ez)^2}{RT} \right) \tag{2.23}$$

A concentration change only of one charge carrier type is not possible due to the electro-neutrality condition, which can be written in differential form:

$$2d[V_O^{\bullet\bullet}] + d[h^{\bullet}] - d[Fe_{Ti}^{'}] - 2d[Fe_{Ti}^{''}] - d[e^{'}] = 0 \tag{2.24}$$

Since oxygen vacancy generation and electronic charge compensation have to occur in exactly the same amount, the total chemical capacitance can be calculated as:

$$C_{chem,total} = \left( \frac{1}{C_{chem,ion}} + \frac{1}{C_{chem,electron}} \right)^{-1} \tag{2.25}$$

The electronic chemical capacitance is, with considering the mass conservation for localised defects, the sum of all partial chemical capacitances of electronic defects. In many mixed conductors, such as LSF, it is assumed, that the dopant is fully ionised, and the electronic chemical capacitance is attributed to annihilation and generation of electron holes [18]. For STFO, the approximation of full dopant ionisation is not necessarily valid, and localised electronic defects, such as *"ionised"* iron, may play an important role in the electronic chemical capacitance. In STFO, the number and charge of electronic defects is smaller than for oxygen vacancies, according to equation 2.20, resulting in a comparatively large ionic chemical capacitance. So the approximation $C_{chem,total} \approx C_{chem,electron}$ is valid for a qualitative picture (with respect to equation 2.25). The charge compensation of an additional oxygen vacancy can occur over generation or consumption of any localised (dopant ionisation) or delocalised (electrons, holes) electronic defect. Typically, one charge compensation mechanism is the most dominant in a given oxygen partial pressure range. In case of STFO, the very low electronic conductivity in the pressure range between air and hydrogen atmosphere concludes a low concentration of mobile electrons and holes, which is by orders of magnitude lower than the oxygen vacancy concentration. If the charge compensation mechanism is predominantly over mobile electrons or holes, very low chemical capacitance (and electronic conductivity) is expected near the intrinsic point, where $[e^{'}] = [h^{\bullet}]$, and the thermal activation of the chemical capacitance should be similar to that of the electronic conductivity. When the main mechanism of charge compensation is attributed to localised electronic defects (e.g. $Fe_{Ti}^{\times}, Fe_{Ti}^{'}, Fe_{Ti}^{''}$), there will be no direct correlation between electronic conductivity and chemical capacitance, even if the corresponding slopes in a Brouwer diagram are equal. If the concentration of the charge compensating carrier (estimated by equation 2.23) is much higher than the number of conduction electrons or holes (calculated out of electronic conductivity and charge carrier mobility) the charge compensation mechanism is mainly attributed to localised electronic defects.

The chemical capacitance mechanism is very similar to the oxygen reduction reaction, the involved electrode defects are equal. The difference is the site of the oxygen exchange. Oxygen in and excorporation from the electrode takes place at the electrode–electrolyte interface (which is typically faster than the oxygen reduction reaction at the surface). Electrons in the electrical contact for the working electrode are referred as $e_{metal}^{'}$. When one electronic defect is dominant, the reaction can be described with one (thermodynamic) equilibrium reaction, which involves the defects with the largest concentration change. Depending on the most dominant electronic defect (which might change with oxygen partial pressure), possible reactions are:

- Full dopant ionisation ($Fe_{Ti}^{'} = Fe_{tot}$), electron holes are the most numerous electronic defect. This is not assumed to be the case for STFO.

$$V_{O,_{YSZ}}^{\bullet\bullet} + O_{O,STFO}^{\times} + 2e_{metal}^{'} + 2h_{STFO}^{\bullet} \rightleftharpoons V_{O,_{STFO}}^{\bullet\bullet} + O_{O,YSZ}^{\times} \tag{2.26}$$

- The redox pair $Fe^{4+} + e^{-} \rightleftharpoons Fe^{3+}$ is most dominant (probably the case for STFO in oxygen or weakly reducing atmosphere).

$$V_{O_{YSZ}}^{\bullet\bullet} + O_{O_{STFO}}^{\times} + 2e_{metal}^{'} + 2Fe_{Ti}^{\times} \rightleftharpoons 2Fe_{Ti}^{'} + V_{O_{STFO}}^{\bullet\bullet} + O_{O_{YSZ}}^{\times} \tag{2.27}$$

- In strongly reducing atmosphere, or with a cathodic DC-bias, the Fe dopant charge might change from Fe$^{3+}$($Fe^{'}$) to Fe$^{2+}$($Fe^{''}$).

$$V_{O_{YSZ}}^{\bullet\bullet} + O_{O_{STFO}}^{\times} + 2e_{metal}^{'} + 2Fe_{Ti}^{'} \rightleftharpoons 2Fe_{Ti}^{''} + V_{O_{STFO}}^{\bullet\bullet} + O_{OYSZ}^{\times} \tag{2.28}$$

  Also, electron trapping in oxygen vacancies might occur in strongly reducing atmosphere.

$$V_{O_{YSZ}}^{\bullet\bullet} + O_{O_{STFO}}^{\times} + 2e_{metal}^{'} + V_{O_{STFO}}^{\bullet\bullet} \rightleftharpoons 2V_{O_{STFO}}^{\bullet} + O_{O_{YSZ}}^{\times} \tag{2.29}$$

# 3 Experimental

## 3.1 Thin film deposition and characterisation

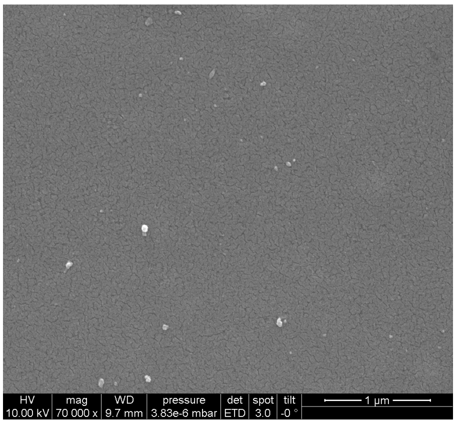

Figure 3.1: SEM image of the STFO film with 0.02 mbar $O_2$ deposition pressure with no visible grains.

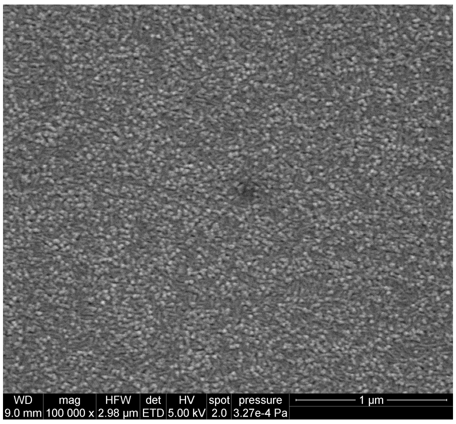

Figure 3.2: SEM image of the STFO film with 0.08 mbar $O_2$ deposition pressure, grains are clearly visible.

Pulsed laser deposition (PLD) was used to produce dense thin films of STFO on YSZ with a thickness ranging from 100-300 nm. The substrate material was single crsystalline YSZ with 8 mol% $Y_2O_3$, supplied by *CrysTec*, Germany. The substrate size was 10x10x0.5 mm with [100] surface orientation. Thin films were deposited at a substrate temperature of about 610 ℃ in a pure oxygen atmosphere with 0.02-0.08 mbar. The laser pulse energy was 400mJ (at the laser) with a repetition rate of 5 Hz. The deposition time was varied between 20 and 60 minutes. On films deposited at 0.08 mbar, grains or columns with an average diameter of ~40 nm are clearly visible in SEM images (fig. 3.2). At a deposition pressure of 0.02 mbar, the surface looks very flat without visible grains in SEM images (fig. 3.1). This stays in agreement with X-ray diffraction measurements on a bruker D8 GADDS (Generalised Area Detection Diffraction System) with Cu $K_\alpha$ radiation. Exclusively [110] orientation was found. Other orientations could not be identified (see fig. 3.4(a)). The powder diffraction pattern is in good agreement with the literature data for $SrTi_{0.5}Fe_{0.5}O_{2.75}$ [22], given that a different iron content was used. In direct comparison with the thin film

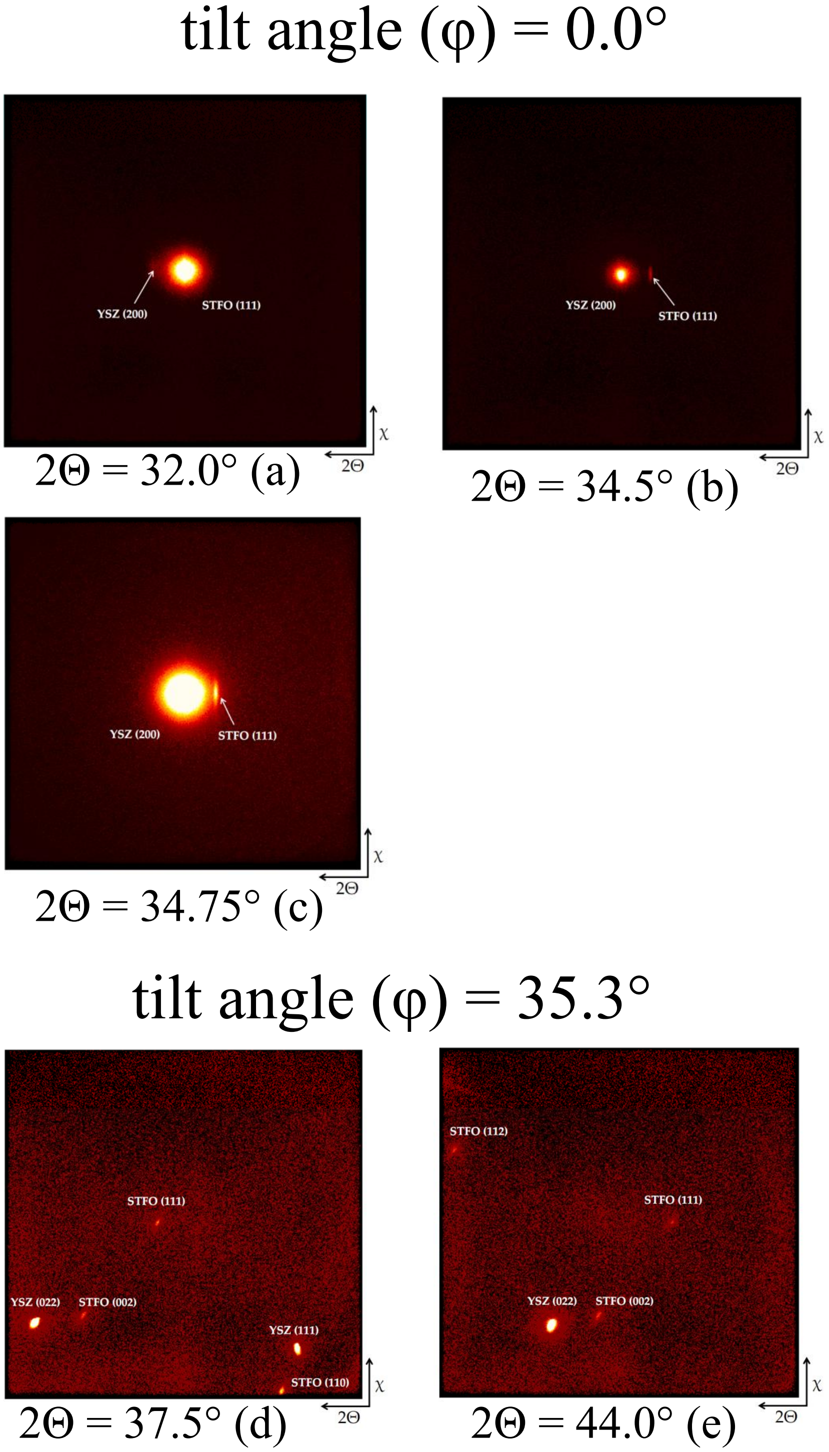

Figure 3.3: Area detection diffraction pattern of an STFO thin film deposited at 0.02 mbar, with beam plane perpendicular to the surface(a,b,c) and tilted by 35.3°(d,e), indicating epitaxial growth.

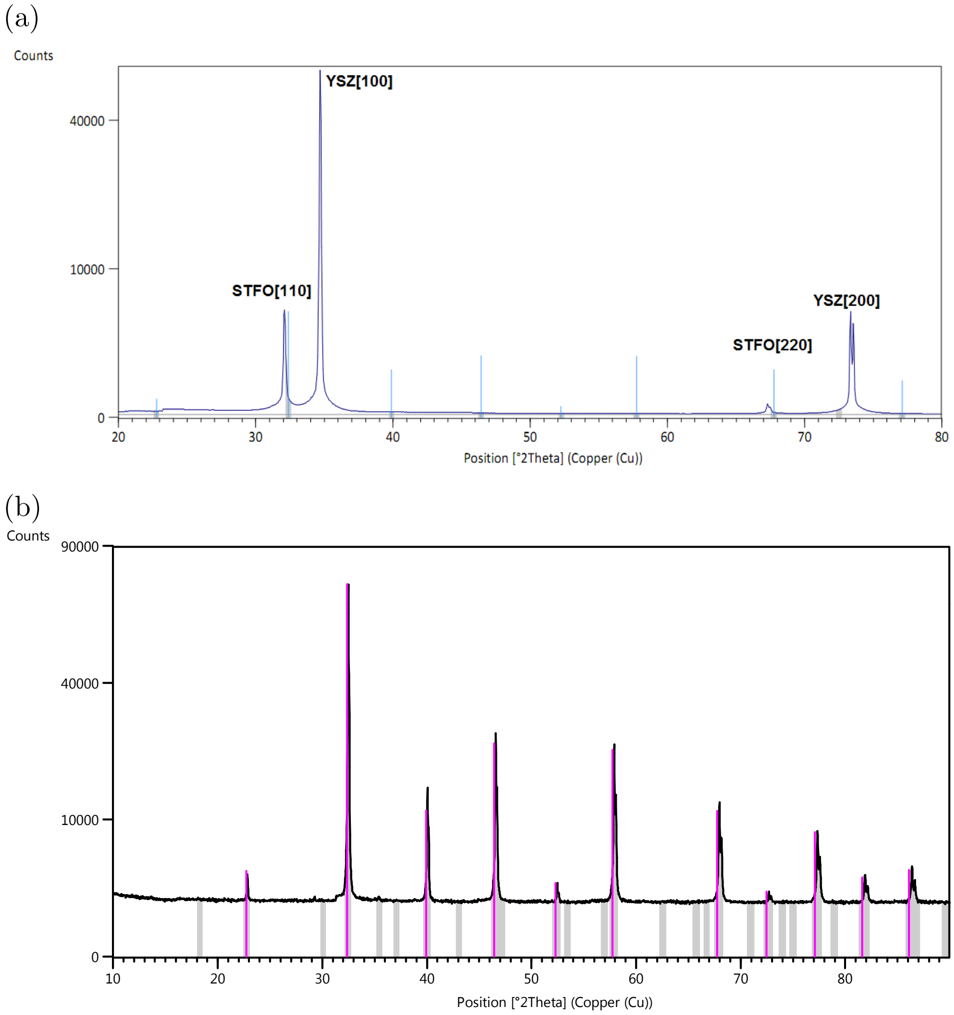

Figure 3.4: $\theta - 2\theta$ diffraction pattern of STFO. (a): grown on [100] YSZ, (b): powder target. Coloured lines are literature data for 50% Fe-doped STFO, the slight lattice mismatch may be attributed to the different iron content or oxygen nonstoichiometry of the literature data.

diffraction pattern, the lattice constant is larger in the thin film, and exclusively [110] orientation can be found. The mismatch in the lattice constant between powder and thin film may be explained with a larger concentration of oxygen vacancies in the thin film because of the low oxygen partial pressure during deposition, or with strain in the thin film. The most dominant peaks in the thin film pattern come from the YSZ substrate, which is typical for XRD patterns of thin films. SEM and X-ray diffraction measurements both conclude epitaxial film growth.

## 3.2 Lithographic techniques

The prepared thin films were spin-coated with negative photoresist, and structured via contact photolithographic masks and exposured in a mercury UV-light source [23]. With this technique, STFO-microelectrodes as well as the platinum thin film grid were prepared. A manual mask aligner with an optical microscope was used to align the microelectrodes and thin film metal grid, which is possible with an error of only few $\mu m$. Circular and rectangular microelectrodes of 50-300 $\mu m$ diameter, resp. 160×395 µm were etched via ion beam etching, using a magnetron argon ion source with 1-3mA beam current and 2-3 kV beam voltage. Due to the low electronic conductivity of STFO, the above mentioned sputtered thin film (80 nm thickness) platinum grid was applied on top or beneath the electrodes. For the platinum grid placed beneath the electrode, ion beam etching was used to achieve smooth corners, whereas for the platinum grid on top, lift-off photolithography was used, where over-etching into the electrode material can not occur, and the surface is not exposed to aggressive solvents (only ethanol). Macroscopic (15 $\mathrm{mm}^2$ area) counter electrodes of STFO with metal grid were placed at the edge of the substrates, revealing a working - to counter electrode area ratio of at least 1:300, therefore the resistance of the counter electrode can be neglected with small error.

### 3.2.1 Ion beam etching

In fig. 3.5, the process of lift-off photolithography is sketched schematically. A thin film of electrode or sputtered metal was deposited before the lithography process. Negative photo-resist was spin-coated at 50 rpm for 30 sec.

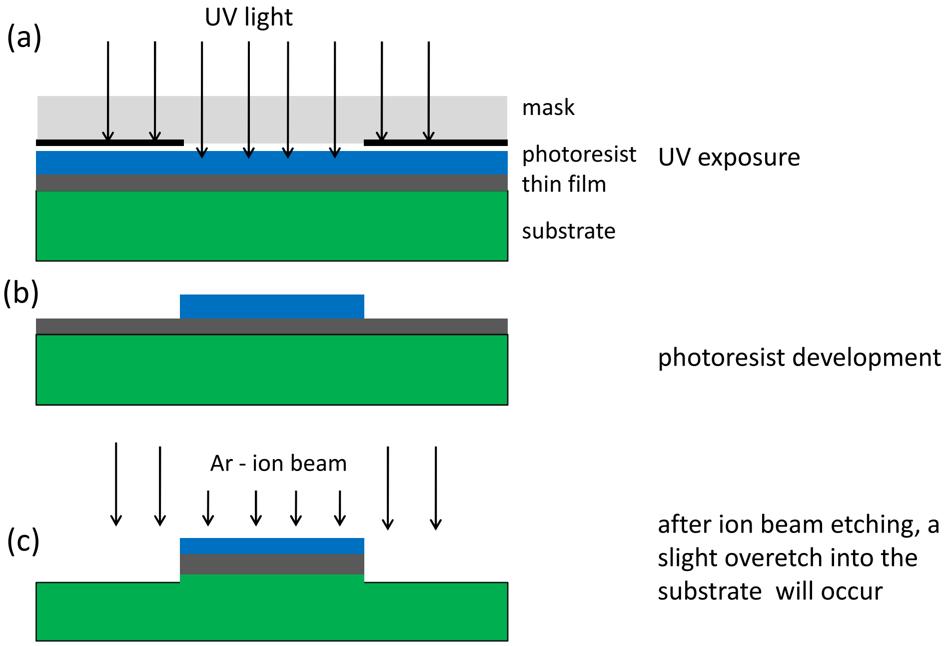

Figure 3.5: Schematic sketch of ion beam etching lithography.

and dried at 100 ℃ for 120 sec. At the substrate edges, the photoresist film is thicker due to surface tension. These *"hills"* have to be removed, so that the distance between photomask and photoresist is minimised. Afterwards, the photoresist was exgposed with UV light and a contact photomask and developed with a liquid developer. The thin film with patterned photoresist on top was etched in a weakly collimated ($\sim$ 1.5 cm spot diameter) argon ion beam. The remaining photoresist was removed with ethanol (per analysis) and an ultrasonic cleaner. The large advantage of ion beam etching is, that every material can be sputtered with argon ions, and etch rates are within the same order of magnitude for a wide range of ceramic and metallic materials. Also, there is no limitation to the deposition process of the thin film. Since the etching process does not stop when the substrate is reached, it causes over-etching into the substrate (fig. 3.5,(c)). Therefore ion beam etching can not be applied for structuring a metal grid on top of an STFO electrode, because the over-etching would occur in the electrode material, and affect the thickness as well as the surface structure.

### 3.2.2 Lift-off photolithography

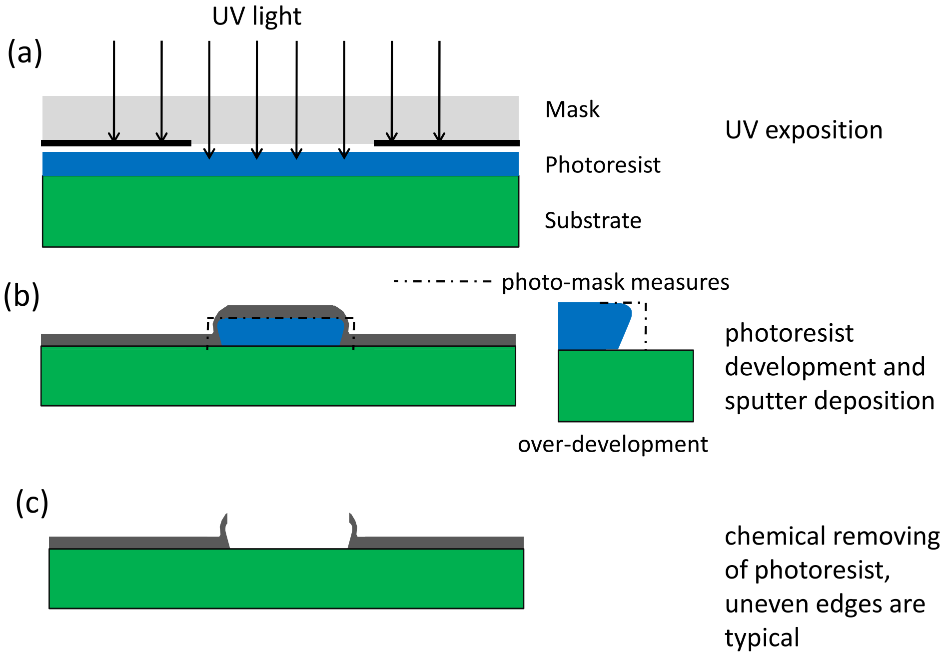

Figure 3.6: Schematic sketch of lift-off photolithography.

The lift-off process is sketched in fig. 3.6. The photoresist is spin-coated on the substrate and structured in the same way as with ion beam etching. Over-development of the photoresist causes slightly overhanging corners, which reduces the mechanical force needed to remove parts of the film during the lift-off process. The substrate with structured photoresist is afterwards coated with a sputtered thin film. The remaining photoresist is dissolved in ethanol and the sputtered film on top of the photoresist is removed. Sputtered thin films can cover even complicated surface topologies, such as overhanging edges (fig. 3.6 (b)). When this is the case, the sample has to be sonicated, which causes mechanical stress to the film. In the case of platinum on STFO, a thin interlayer of titanium was used to ensure sufficient adhesion between metal and electrode. With lift-off photolithography, only cold deposited films can be structured, because the photoresist is not stable at high temperature. Also, the edges of the film are slightly deformed (as seen in fig. 3.6 (c)), which is clearly visible in SEM imaging. The advantage, compared to ion beam etching, is that over-etching into the substrate can not occur, so it is suitable to deposit a metal grid on top of an electrode with only little effect on the surface structure.

### 3.2.3 Design of the photolithographic mask

A photolithographic mask with a new electrode and metal grid design was designed, with the aim to minimise the complexity of electronic and ionic transport paths. The new structures allow a more reliable and quantitative interpretation of the impedance features caused by transport losses, which is discussed in detail in section 5. The mask was designed in *AutoCad* and produced by *Rose Fotomasken*, Germany. It consists of a 4×4 inch$^2$ quartz

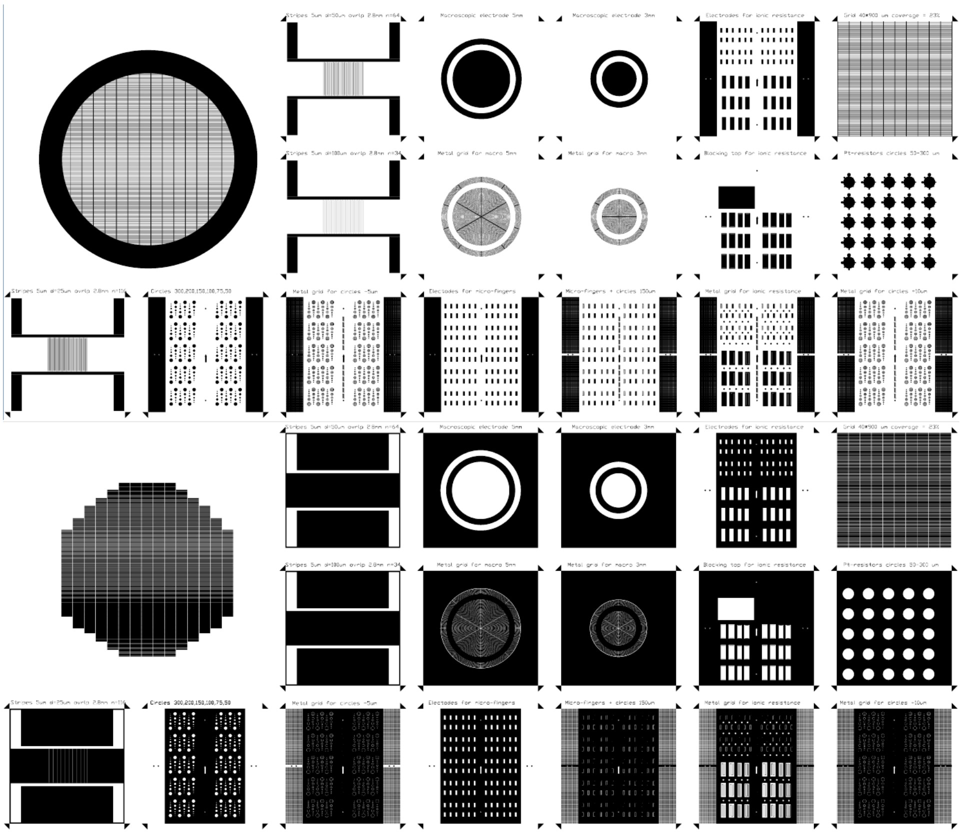

Figure 3.7: Sketch of the photo lithographic mask, which was used for the measurements in section 5 and for other research projects, which are not within this work. A magnification of the designs which were used in this work is shown in fig. 5.4.

substrate, with structured low-reflective chromium as UV-blocking layer. 17 different designs for the structuring of thin films on 10×10 mm$^2$ substrates are available in positive and negative chromium structure. The designs range from circular microelectrodes to macroscopic electrodes of different sizes, with included thin film metal grid, and also finger structures that allow the observation of dendrite growth in liquid electrochemistry. The set of designs called *microfingers* was used in section 5.

## 3.3 Impedance spectroscopy setup

This work focusses on electrode characterisation by means of Electrochemical Impedance Spectroscopy (EIS) with a *Novocontrol Alpha-A High Performance Frequency Analyser*, equipped with a *Novocontrol POT/GAL 30V/2A* interface, allowing impedance, DC, and DC-polarized impedance measurements. The electrical measurements were carried out in a temperature range of 350-800 ℃ in an atmosphere of 2.5% $H_2$ and about 2.5% $H_2O$ vapour in argon as carrier gas.

### 3.3.1 Micro-contact measurement station

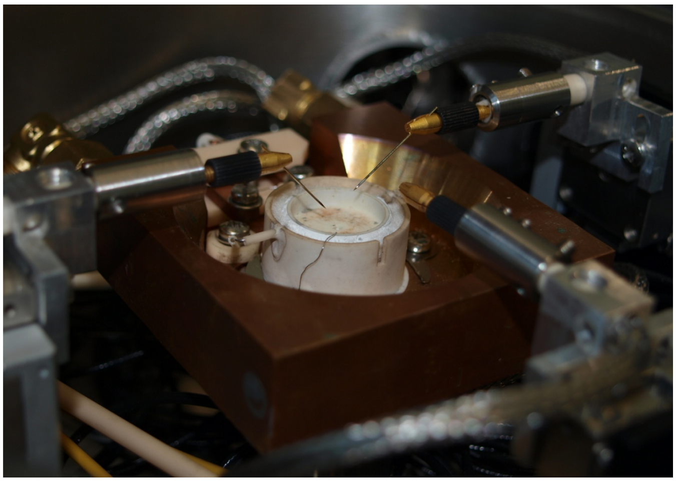

Figure 3.8: Heater and contacting needles of the micro contact measurement station.

Measurements were carried out in a sealed stainless steel chamber (I-Pot) designed by Tobias Huber, with interchangeable gas atmospheres. Slight

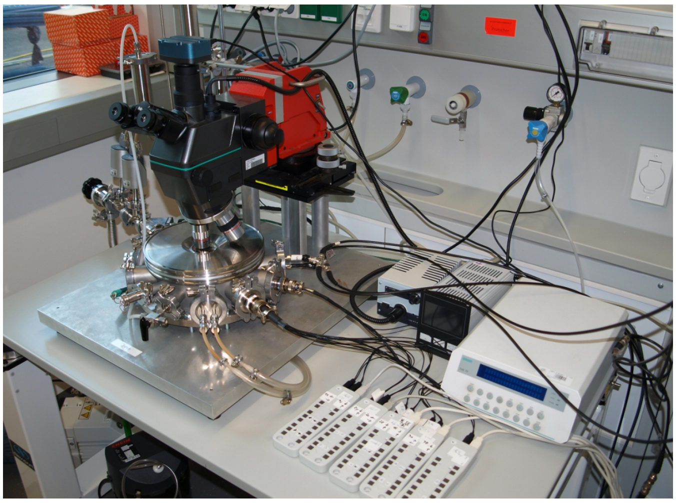

Figure 3.9: Impedance measurement station, including I-Pot with electrical wiring, optical microscope, heater controller and remote controls for the piezoelectric linear stages. The image was taken from [24, Photograph of the Impedance measurement station.]

excess pressure was used (~50 mbar) to avoid leaking in of oxygen (purely diffusive oxygen transport can not be avoided). The sample was heated with a *Linkam TS1000 EV 17/3* heater, which allows heating up to 1000℃ (set) and fast temperature changes. Counter and working electrodes were contacted with platinum or gold plated steel needles, moved by high-precision linear piezoelectric stages (*Newport Agilis*$^{TM}$). The stages were controlled by a computer interface, or remote controllers. The question, whether platinum, or gold plated steel needles produce a more reliable electric contact is depending on the measurement time and electrode type. Platinum needles are chemically stable, and an established electrode contact is rather reliable for long term measurements. On the other hand, they are much softer than iron, which is a disadvantage, if a metal grid beneath an STFO electrode has to be contacted through the thin film. Gold plated steel needles have the advantage of being much cheaper, and rather pointed, but they are not well suitable for long term measurements, because the gold plating is not stable at high temperature, and oxidation of the needle may produce a growing contact resistance.

### 3.3.2 Electrical measurement principle

For the electrical measurements, a small working electrode was measured against an extended counter electrode (see fig. 3.10). The area ratio between working and counter electrode is at least 1:300. Therefore the resistance of the counter electrode can be neglected with small error, and a reference electrode is not needed. Additionally, platinum paste was applied to the back side of the substrate. This is very helpful to avoid *"inductive loops"* in the high frequency part of the spectrum [25]. The electrical shielding reduces the electrical noise, which may be introduced by the heater. Also, the closed steel pot, which acts as a Faraday cage and a barrier for atmospheric convection, is very helpful for the reduction of measurement artifacts caused by electrical noise and temperature changes.

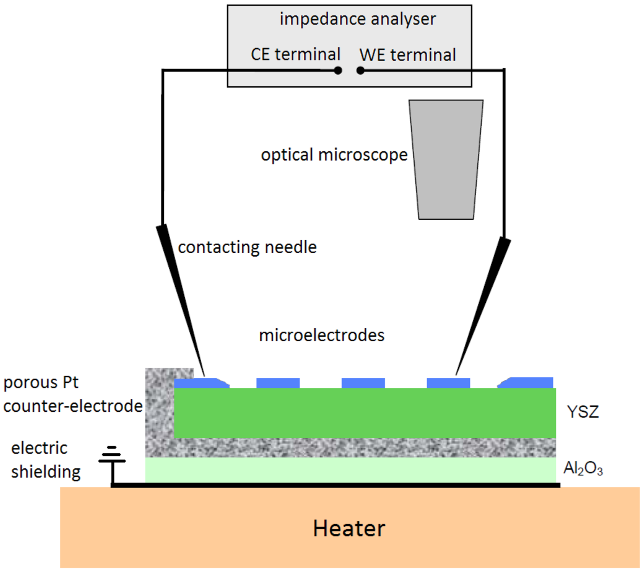

Figure 3.10: Principal sketch of the impedance measurement of microelectrodes against an extended counter electrode.

## 3.4 Impedance spectroscopy on thin film model electrodes

Impedance spectroscopy is an in-situ investigation method to determine the properties of an electrochemical system. Electrical measurements can be carried out with high very high precision, even when voltage and current are in the range of millivolts and nanoamperes, as long as sources of noise are sufficiently shielded. Nevertheless, the interpretation of the spectra is often a non-trivial task, even for experienced scientists. Not every elementary process can be identified. For example, only the sum of series of resistors, or parallel capacitors, etc. can be measured. Also the influence of some processes on an impedance spectrum is too small to be measured, which is the case for measurement of the adsorbate surface coverage and the corresponding potential step. Different methods of interpreting impedance spectra can be applied. Quantitative information can be gained, when the measurements are fitted with an equivalent circuit. This circuit can be derived out of a proposed electrochemical reaction model of an electrode, which includes all relevant resistive and capacitive processes, so that the fitting parameters are linked to electrode properties. In this case, not only the quality of the fit is important, but also the scaling of the fitting parameters to changes in electrode geometry, gas atmosphere and temperature has to be consistent with the proposed reaction model. When the relevant resistive and capacitive processes are not known, the features in the impedance spectra can be parametrized with an equivalent circuit with no underlying physical interpretation, which is often achieved by a simple series of R||CPE elements. In this case, the scaling of the circuit parameters to variations in geometry and temperature may lead to an electrochemical interpretation of the spectra and might help to derive an equivalent circuit which is motivated by an electrochemical reaction model. Even a perfect fit to the measured spectrum does not necessarily mean, that the underlying equivalent circuit and electrochemical interpretation is correct, if the circuit elements do not correspond to physically motivated parameters, or their numerical values are out of the region expected by theoretical calculations. Also, variations in the sample geometry, temperature, DC-bias, and other parameters have to be consistent with the proposed reaction model. Even though these concerns have to be taken seriously, impedance spectroscopy can reveal reliable quantitative information on the behaviour of an electrochemical system, once a (qualitative) reaction model is validated with the methods explained above, or additional measurement methods (for example $^{18}$O tracer experiments with SIMS [26]). In order to reduce the amount of unknown parameters and system complexity, geometrically well defined thin film electrodes were used in the present study [27]. These have a defined thickness, surface area and in special cases even crystallographic orientation, and their geometry is easily designable by photolithography. In [27] the advantages and field of application of thin film microelectrodes is explained in detail.

### 3.4.1 Simplified equivalent circuits for thin film electrodes

Many acceptor-doped electroceramics, which are investigated as electrode materials exhibit very high electronic conductivity ($\geq$ 100 Scm$^{-1}$). In this case, electronic transport is very fast, and causes negligible resistance in thin film microelectrodes. Also, since microelectrodes are very thin (typ.100-400 nm), the vertical oxygen transport path is short and causes no relevant resistance, when the ionic conductivity is sufficiently high. The interface between electrode and YSZ substrate is often responsible for an ionic transport resistance and a corresponding double layer capacitance. Out of these assumptions, J.Jamnik and J.Maier [21] derived a simplified equivalent circuit (fig. 3.11,(b)).

### 3.4.2 Temperature calculation - YSZ spreading resistance

The heater used for impedance measurements can be set to a temperature up to 1000°C, but the set point of the heater is typically 50-150℃ higher than the actual microelectrode temperature. This mismatch is not reproducible, since it is strongly depending on the gap size between heater and shielding plate, and the position of the sample on the heater, so a different method for the temperature determination has to be found.

**YSZ spreading resistance** The YSZ spreading resistance can be measured in the high frequency region of the impedance spectrum and is caused

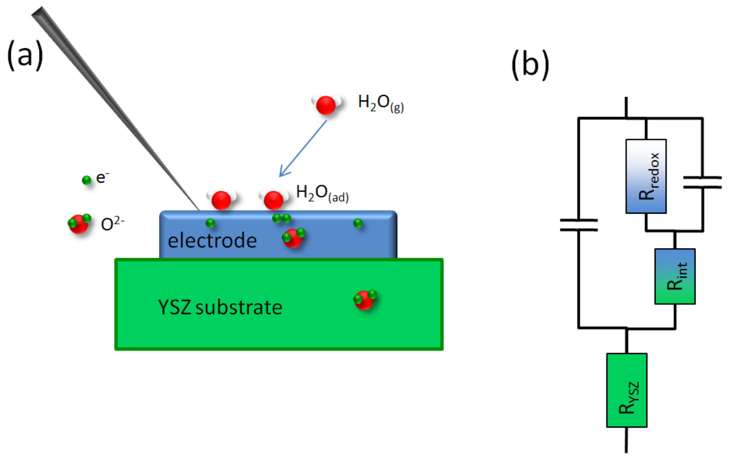

Figure 3.11: Reaction scheme of a mixed conducting fuel cell anode (a) and corresponding equivalent circuit (b) for an electrode with negligible electronic and ionic resistance.

by the ohmic resistance of the electrolyte. When the electrode is circular, it can be used to calculate the specific conductivity with the spreading resistance formula: [27]

$$\rho_{ion} = 2d_{electrode}R_{YSZ} \tag{3.1}$$

This formula is based on the assumption of an infinite substrate, which is a sufficiently good approximation if the electrode diameter is less than half of the substrate thickness. When the temperature dependence of the YSZ conductivity is known, the temperature can be calculated. The exact conductivity - temperature relationship was measured in a closed furnace with homogeneous temperature for the CrysTec substrates, that were used in [24]. If not otherwise stated, all temperature values for impedance measurements have been calculated with this method.

### 3.4.3 Electrochemical equivalent circuit elements

In electrochemistry, several processes, i.e. double-layer capacitance, transport and diffusion phenomena can not always be described with the standard (ideal) passive elements, such as resistor and capacitor. Commonly used elements in electrochemisty are:

- The **constant phase element** (CPE) can be interpreted as a non-ideal capacitor
  $$Z(\omega) = \frac{1}{Q(i\omega)^n} \tag{3.2}$$
  When n=1, the element is an ideal capacitor with C=Q. In a typical fit, n is slightly below 1. A value of 0 would describe a perfect resistor with R=$Q^{-1}$. The value Q is a parameter in the impedance function, and can not be interpreted as a true capacitance value. In many cases, a CPE is placed in parallel to a resistor, for which a capacitance can be estimated, according to [28]:
  $$C = (R^{1-n}Q)^{\frac{1}{n}} \tag{3.3}$$
  The R||CPE element is a very common equivalent circuit for fitting. It can describe the impedance of grain boundaries in the brick layer model [28]. But also features that are ideal capacitances in theory, such as chemical capacitance, are much more precisely (in terms of fitting error) fitted with a CPE with a n-value slightly below 1. The nature of this phenomenon is not always well understood.

- The **Warburg element** is describing a diffusive transport process. The equivalent circuit is a finite transmission line of R-C elements, and is either terminated with an open end (open Warburg) or a short circuit (short Warburg). R is the sum of (differential) resistances, and C is the sum of (differential) capacitances. The impedance function of such an equivalent circuit can be calculated, as explained in chapter 5.2
  $$Z_{short} = \sqrt{\frac{R}{i\omega C}}\tanh(Ri\omega C) \tag{3.4}$$
  $$Z_{open} = \sqrt{\frac{R}{i\omega C}}\coth(Ri\omega C) \tag{3.5}$$

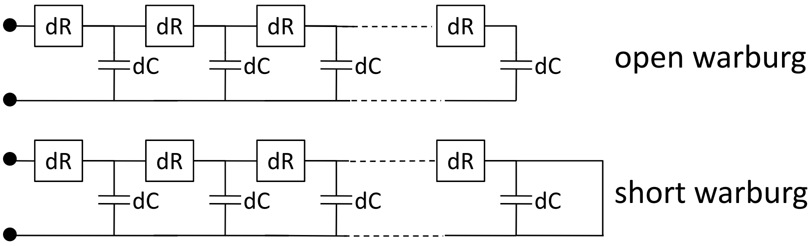

Figure 3.12: Equivalent circuit for a open and short Warburg element.

The nyquist plot of the Warburg impedance functions is shown in fig. 3.14

- The **Gerischer element** is describing an admixture of diffusion and reaction, which can be treated as the infinite transmission line shown in fig. 3.13. The resulting impedance function is surprisingly simple (eqn. 3.6). The impedance function only consists of two independent parameters, whereas three parameters are needed to construct the equivalent circuit.

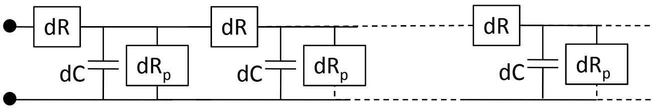

Figure 3.13: Equivalent circuit for a Gerischer element.

$$Z = \frac{1}{Y_0\sqrt{k + i\omega}} \tag{3.6}$$

The nyquist plot of the Gerischer impedance function is shown in fig. 3.14

The extended elements (Warburg and Gerischer) are idealised models, where perfectly blocking or conductive terminals, or an infinite length are assumed. For an exact model of the electrochemical processes in a STFO model electrode, a generalised transmission line circuit, discussed in chapter 5.2, has to be introduced and used for the fitting of the measurements.

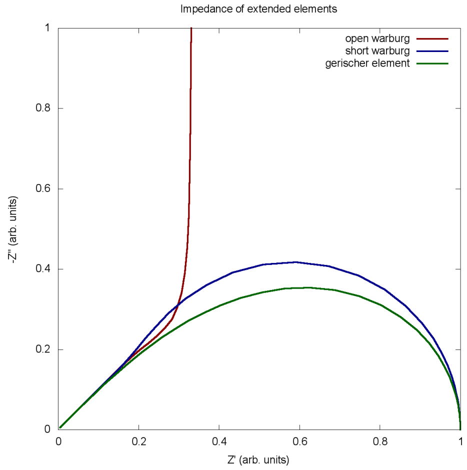

Figure 3.14: Nyquist plot of the impedance function of extended elements, all parameters are set to 1.

# 4 Impedance measurements on circular microelectrodes

## 4.1 Circular microelectrodes without metal grid

Circular microelectrodes of varying diameter are the most commonly used design in thin film microelectrode research. They are easy to produce with standard photolithographic techniques and the YSZ spreading resistance allows a calculation of the YSZ conductivity (and therefore temperature) via the spreading resistance formula (equation 3.1 [27]). Also, variations in diameter allow identification of the location of the rate limiting step (typically electrode surface or electrode-electrolyte interface) Owing to the thin film geometry, electronic conductivity has to be sufficient to produce only negligible electronic transport losses, which, as a rule of thumb, is the case when the electronic sheet resistance is much smaller than the YSZ offset resistance (which is not the case for STFO).

The first measurements were carried out on circular microelectrodes with diameter (d) ranging from 20 to 100 $\mu$m. A typically measured spectrum for a 60 $\mu$m electrode is shown in fig. 4.1. Due to the large electronic resistance, a physically motivated equivalent circuit can not be derived.The YSZ resistance ($R_{\mathrm{YSZ}}$) was directly read from the spectra and the very low frequency part of the spectra was fitted with a simple R1-(R2||CPE) circuit (see fig. 4.1 (a)). The resistance R1 is assumed to be mainly caused by lateral electronic transport and YSZ spreading resistance, R2 is assumed to be mainly caused by the electrochemical surface reactions. The capacitance of the (R2||CPE) element can be calculated with equation 3.3, and is assumed to be caused by the chemical capacitance of the electrode. Since no exact equivalent circuit can be derived, an equivalent circuit which is capable of fitting the entire electrode impedance will not increase the amount of information, since an electrochemical interpretation is still missing. In this case, the temperature can not be measured with the YSZ spreading resistance, but was estimated to be $T_{electrode} \approx T_{set} - 100\,°C$. For electrodes with high

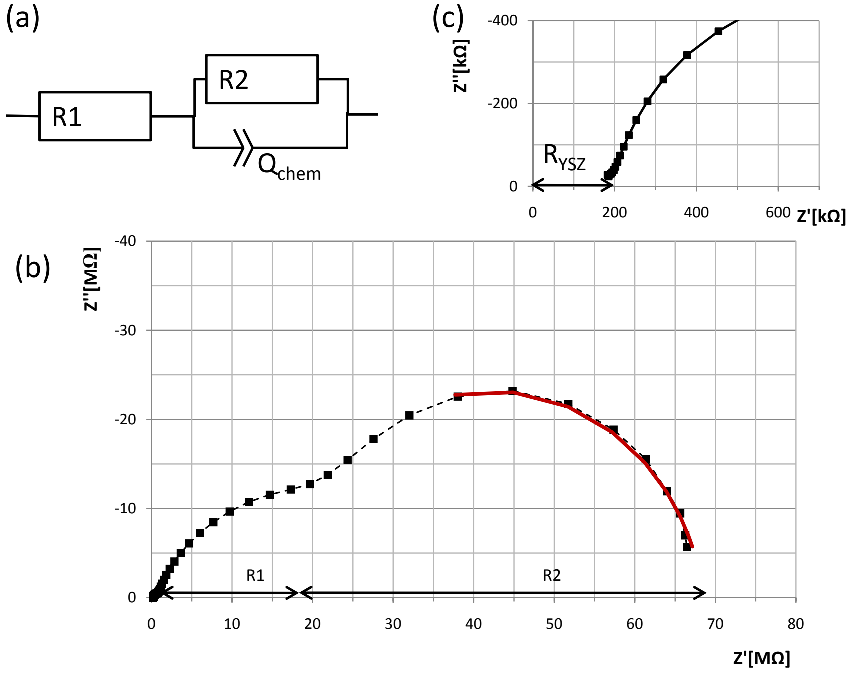

Figure 4.1: Equivalent circuit (a) and typical impedance spectrum (black) at $\sim$ 650 ℃ with fit of the low-frequency feature (red) (b, c).

electronic conductivity, some diameter-dependences can be estimated, and compared with the measured spectra.

As can obviously be seen in fig. 4.2 and table 4.1, not even one parameter does scale as expected for an electrode with high electronic conductivity. The YSZ offset resistance is scaling with $d^{-0,24}$ with very large scatter,

| fitting parameter | measured d-dependence | expected d-dependence |
|---|---|---|
| R1-$R_{YSZ}$ | $\sim d^{0.25}$ | (should be 0) |
| R2 | $\sim d^{-1.56}$ | $\sim d^{-2}$ (RDS on surface)<br>$\sim d^{-1}$ (RDS at TPB) |
| $C_{chem}$ | $\sim d^{1,66}$ | $\sim d^{2}$ |
| $R_{YSZ}$ | $\sim d^{-0.21}$ | $\sim d^{-1}$ |

Table 4.1: Measured and calculated dependence of fitting parameters on the microelectrode diameter (d)

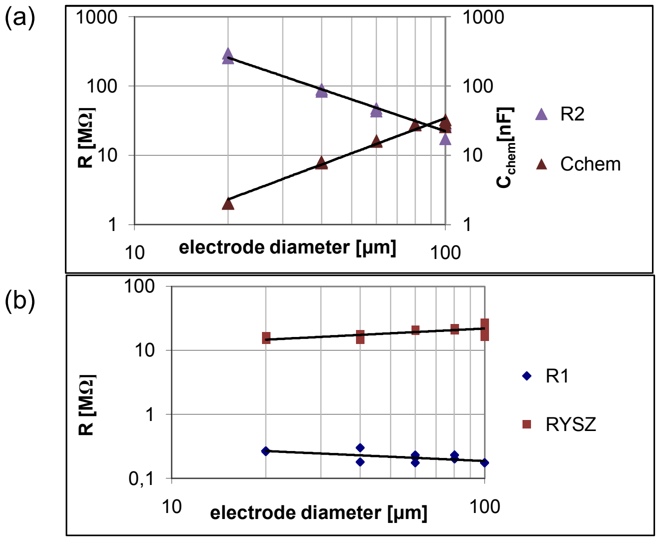

Figure 4.2: Scaling of the fitting parameters for electrodes without metal grid (fig. 4.1) with electrode diameter d, T ≈ 650°C. (a): Chemical capacitance and R2 show similarly strong dependence on diameter, (b): R1 and $R_{YSZ}$ show only minor dependence on diameter

and might be even independent of diameter. Also, the absolute value is by a factor of 20-50 higher than expected for the given temperature. These observations lead to the assumption, that in the high frequency region, the current path is restricted to a very small area around the contacting needle, and starts to cover a larger part of the electrode at lower frequency, resulting in a stronger diameter-dependence of the parameters R2 and $C_{\mathrm{chem}}$. It can be assumed, that the performance of these electrodes is limited by lateral electronic transport. A qualitative interpretation of the impedance spectra might be possible, but quantitative information can not be gained due to lack of a electrochemically motivated equivalent circuit, and exact reaction model.

## 4.2 Measurements on circular microelectrodes with thin film metal grid

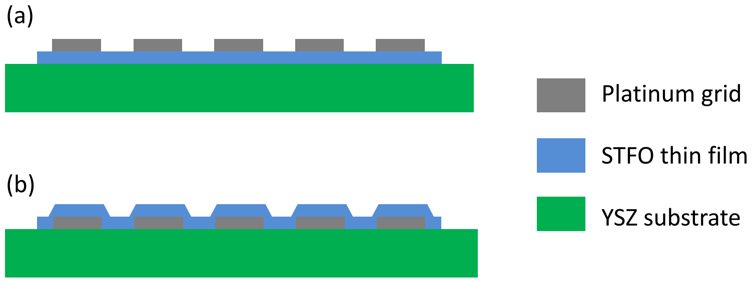

Figure 4.3: Schematic cross section of an electrode with thin film metal grid placed either on top (a) or below the electrode (b)

In order to compensate the lack of electronic conductivity, a photolithographically patterned ∼80 nm thick platinum mesh was placed either on top of the electrode, or between the YSZ substrate and the electrode, which leads to different reaction pathways with individual advantages and disadvantages. It should be noted that the assumptions on the relevant resistive processes made here will be confirmed and quantified in section 5 on an improved electrode design.

In table 4.2, the deposition parameters for STFO and platinum thin films are summarized. It is noteworthy, that the gas pressure during the PLD deposition was different for electrodes with metal mesh above and beneath the electrode. After the measurements on circular microelectrodes with metal grid on top were completed, it was observed that at a deposition pressure of 0.02 mbar, grain boundaries are not visible in SEM measurements (see fig. 3.1,3.2), which lead to choosing a lower deposition pressure for the measurements with metal grid below the electrode.

**Variations of electrode geometry** When a platinum thin film grid is applied, the electrode is a periodic structure of metal stripes and *"holes"*, shown in fig. 4.4. Therefore, a variation in electrode diameter does not change the principal geometry of reaction and transport paths. Consequently, only electrodes with 200 µm diameter were measured.

When the size of the mesh is varied, the lateral electronic transport length

| Deposition parameters | | | |
|---|---|---|---|
| Thin film type | Substrate temperature | Deposition rate | Other deposition parameters |
| STFO thin film, metal mesh on top | 610-630 °C | $\sim$ 5nm/min | 0.08 mbar $O_2$ pressure,<br>5 Hz laser repetition,<br>400 mJ/pulse,<br>40 min. deposition |
| STFO thin film, metal mesh below | 610-630 °C | $\sim$ 5 nm/min | 0.02 mbar $O_2$ pressure,<br>5 Hz laser repetition,<br>400 mJ/pulse,<br>20-60 min deposition |
| Pt, sputtered thin film | $\sim$ 30 °C | 0.8 nm/sec | 0.02 mbar Ar pressure,<br>current: 100 mA<br>100 sec. deposition ($\sim$80 nm) |

Table 4.2: Deposition parameters for STFO and platinum thin films for circular microelectrodes

is changed, while vertical transport processes remain unchanged. Variations in the metal mesh geometry allow the identification of impedance features that are caused by lateral transport phenomena. Two different mesh sizes were used, see fig. 4.4:

- Quadratic mesh with 10 $\mu$m stripes, and 10×10 $\mu m^2$ *”holes”*
- Quadratic mesh with 15 $\mu$m stripes, and 35×35 $\mu m^2$ *”holes”*

## 4.3 Metal grid on top of the electrode

With a metal grid on top of the electrode, the whole electrode is grown on YSZ, ensuring high film quality and homogeneity. Also, cracks are unlikely to appear in the region of the metal grid edges. There are several requirements on the metal mesh material. It has to be stable against oxidation, and should not diffuse into the electrode material. Also high thermal stability and dense film growth are required. The requirement of chemical stability only allows the use of noble metals. Platinum has a high melting point (1768°C)[12] and the film structure, as well as thermal stability for sputtered thin films is well known [29]. The relatively high catalytic activity

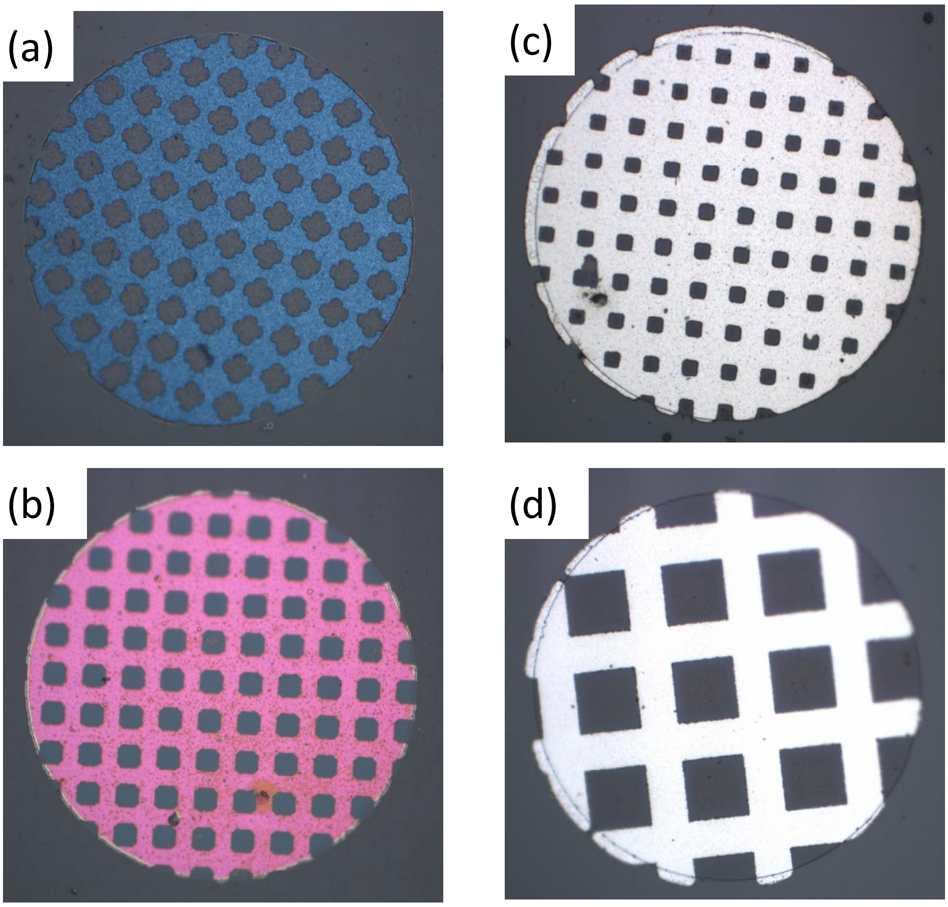

Figure 4.4: Optical microscope images of microelectrodes with 200 µm diameter
(a): metal mesh (10 µm holes) below the electrode, 20 minutes PLD deposition time
(b): metal mesh below the electrode, 40 minutes PLD deposition time. The different colours are caused by interference phenomena on thin films.
(c): metal mesh above the electrode 10 µm holes
(d): metal mesh above the electrodes, 35 µm mesh.

of platinum might lead to an additional triple phase boundary effect, although this is not assumed to play an important role, since the TPB length is small, compared to TPB optimised electrodes. Also on (mixed conducting) samaria doped ceria anodes wit platinum current collectors, no TPB activity could be found [8]. Lift-off photolithography (fig. 3.6) was used for the patterning of the thin films. During the lift-off process, only ethanol (per analysis) is used to remove the unwanted parts of the metal film to keep the STFO surface as clean as possible. A 10 nm titanium interlayer between electrode and platinum film was used to ensure sufficient adhesion of the platinum grid and avoid damage during the lift-off process. Figures 4.5 and 4.6 indicate, that the platinum thin film is dense, but due to the lift-off photolithography, deformations occur at the film edges, which is explained in fig. 3.6. This is not a problem in this case, but it indicates, that lift-off photolithography is not suited to produce a metal grid beneath the electrode, because no dense film can be grown over the complex edge structure of the lift-off mesh. Also, over-development of the photoresist can be seen. The platinum film has 7.5×7.5 µm holes with 12.5 µm stripes, which clearly differs from the nominal mask with 10/10 µm. Over-development is a typical artifact in lift-off photolithography. This effect has to be considered, when the resistance is normalised to the free surface area. The platinum and STFO thin film both appear dense with clearly visible grains, with an average grain diameter of 100-200 nm for platinum and ∼40 nm for the STFO

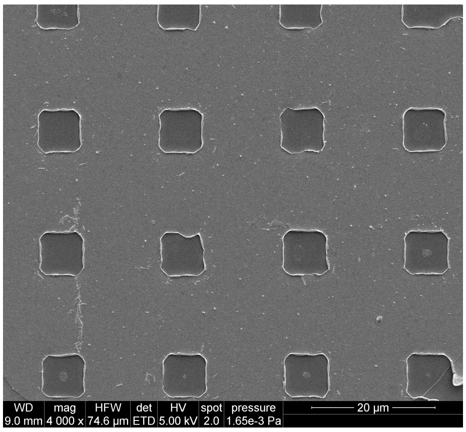

Figure 4.5: SEM of an electrode part with microstructured Pt grid.

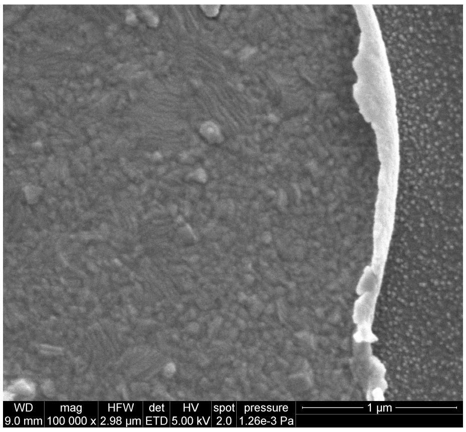

Figure 4.6: SEM of the platinum mesh edge on STFO.

film (this is better visible in fig. 3.2) A reaction scheme for the surface and transport reactions is given in fig. 4.7. In the free surface area, lateral electronic transport and oxygen incorporation are assumed to be the dominant resistive features. In the area below the metal grid, the surface reaction is assumed to be blocked, but oxygen exchange into the YSZ is still possible over the chemical capacitance mechanism.

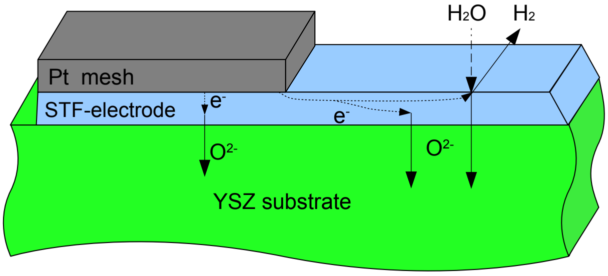

Figure 4.7: Reaction scheme for the electrode reactions with Pt grid on top of the electrode.

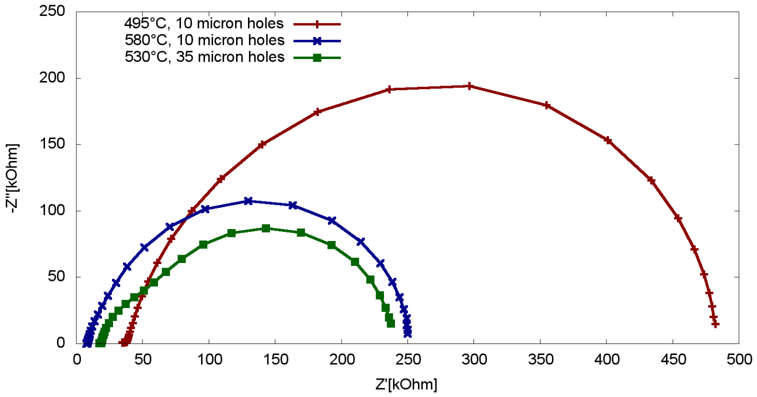

Figure 4.8: Comparison of impedance spectra of circular (d = 200 nm) STFO microelectrodes with platinum mesh on top, variation of mesh size between 10 µm and 35 µm.

**Comparison between two metal grid sizes** In fig. 4.8, the dependence of the shape of the spectra on the metal mesh size is shown. With 35 µm holes, a high-frequency feature can be clearly seen, which is not (or only very slightly) visible with 10 µm holes. This is probably attributed to the larger electronic transport length with 35 µm holes. The larger DC-resistance of electrodes with 10 µm holes (even at slightly higher temperature) is probably attributed to the smaller fraction of free surface area (see fig. 4.4).

### 4.3.1 Temperature dependence of the spectra

Most of the relevant resistive reactions that occur in mixed conducting electrodes are thermally activated. A measurement of the corresponding activation energies can help to identify and understand the underlying processes. When the sample is heated, a fast initial degradation takes place over some hours. Only after this process, a reliable measurement of activation energies can be made. In fig. 4.9 and 4.10, the temperature dependence of the impedance spectra for electrodes with 10 and 35 µm *"holes"* is shown. The clear dependence of the shape of the spectra (especially the high frequency

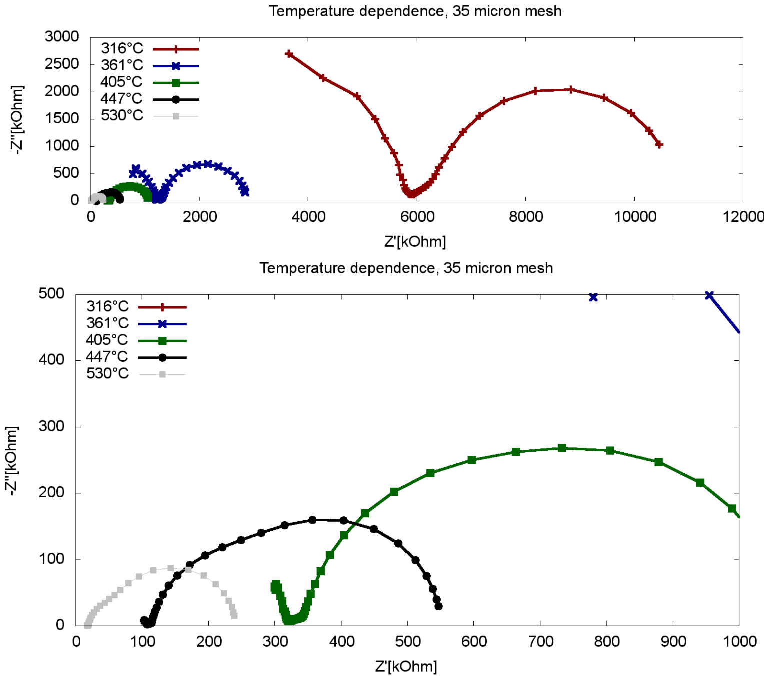

Figure 4.9: Impedance spectra of circular (d = 200 nm) STFO microelectrodes with platinum mesh on top, mesh size is 35×35 µm holes with 15 µm stripes, (a): for five different temperatures, (b): magnification of the three spectra at the highest temperatures.

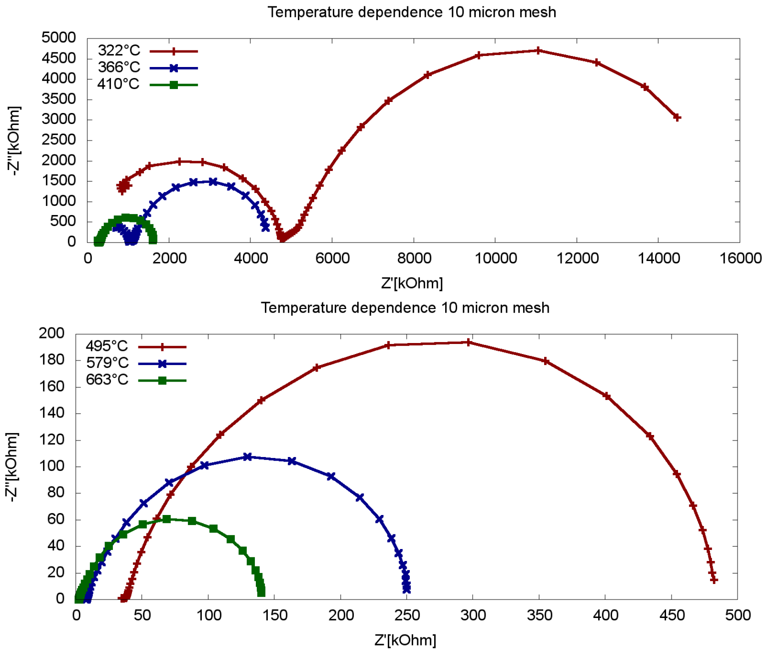

Figure 4.10: Impedance spectra of circular (d = 200 nm) STFO microelectrodes with platinum mesh on top, mesh size is 10×10 µm holes with 10 µm stripes, (a): for 322-410 ℃ (b): 495-663 ℃.

feature at higher temperature) on the metal mesh size indicates, that the lateral electronic transport depicted in fig. 4.7 is causing a relevant resistance and might even be a limiting factor for the 35 µm mesh electrodes at low temperature. Typically, a diffusive process, such as lateral electronic conduction, is causing a 45° feature in the high to medium frequency part of an impedance spectrum, as simulated for Warburg and Gerischer elements in fig. 3.14. A large part of the electrode is covered by the metal mesh (55% and 85% for 35 and 10 µm holes, respectively, when over-development of the photoresist is considered). This causes a large chemical capacitance, which is measured in parallel to the lateral electronic diffusion, and a characteristic 45° line can not be observed in the measurements. Therefore, a reliable quantitative measurement of the transport losses is not possible. However, a qualitative interpretation can be made. With a 35 µm mesh at 530℃, a high frequency shoulder can clearly be distinguished from the low frequency semicircle, which can not be observed for the 10 µm mesh. This indicates, that this shoulder is due to lateral electronic diffusion. When the temperature is reduced, the high frequency feature becomes relatively bigger, compared to the low-frequency semicircle. At 405 ℃ and below, high and low frequency feature can not be distinguished, but form one highly distorted semicircle. This is also the temperature, where the activation energy of the total electrode resistance is shifting from 0.53 to 0.75 eV , which is possibly attributed to a change in the rate limiting step from the surface reaction to the higher activated electronic transport (visible in fig. 4.11).

For the arrhenius plot in fig. 4.11, the low-frequency semicircle was fitted with an R1-(R2‖CPE) element, as shown in fig. 4.1. The value of R2 (which is believed to be the surface reaction resistance), multiplied with the free surface area gives the area specific resistance (ASR) of the oxygen exchange reaction.

## 4.4 Metal grid beneath the electrode

When the metal grid is placed between the electrode and the YSZ substrate, catalytic effects can not occur, since there is no triple phase boundary at the platinum grid edges. The film growth of STFO does differ whether it is growing on YSZ or platinum. The contributions from the electrode part grown on YSZ and on platinum are measured in parallel. Also, cracks in the

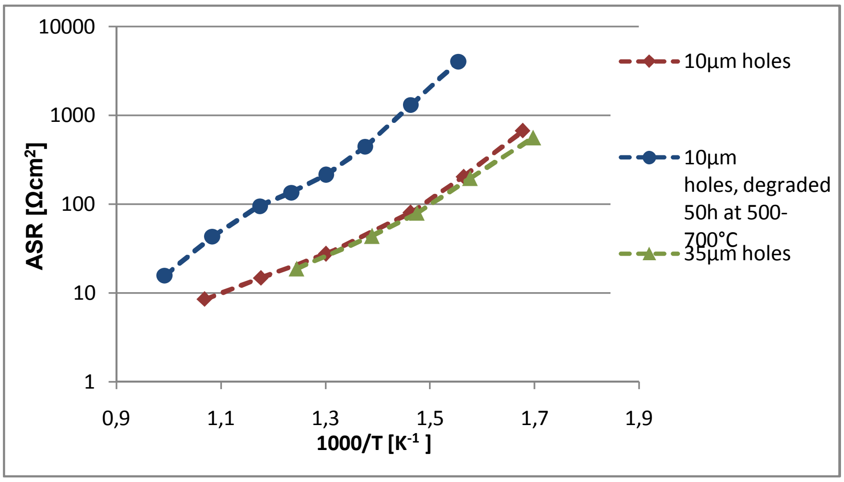

Figure 4.11: Arrhenius plot of the area specific low-frequency semicircle resistance for circular microelectrodes with metal grid on top.

electrode might occur at the metal grid edges due to thermal and chemical expansion of the electrode, although SEM and impedance measurements do not indicate this (see fig. 4.12 and 4.13). Depending on the ionic conductivity, the reaction path for oxygen exchange over the platinum grid may be activated, which is difficult to determine only by EIS, since electronic and ionic transport are both expected to create Warburg-like features in the impedance spectra. The deposition pressure for these electrodes was 0.02 mbar, instead of 0.08 mbar for the electrodes with metal grid on top, which leads to a much flatter surface, and XRD measurements even conclude epitaxial film growth on YSZ (see section 3.1).

**Optical properties of the electrodes** The STFO thin films have a slight brownish color, but light absorption, which is visible in transillumination microscopy, appears to be rather low for thin films in the visible spectral range. The refractive index of STFO is similar to that of YSZ. This causes hardly any reflections on the STFO-YSZ interface. However when the films are placed on top of a flat-surfaced platinum grid, most of the light is reflected, causing interference patterns. According to the theory, the interference color is blueish (short wavelength) for short deposition time

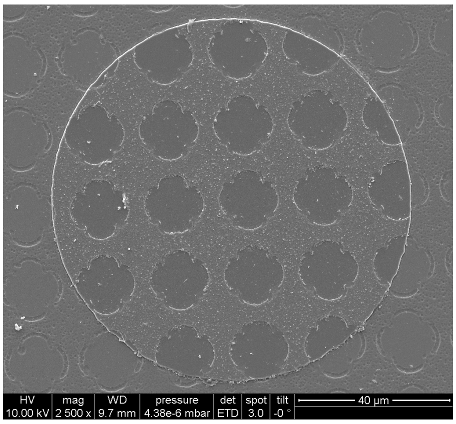

Figure 4.12: SEM image of an electrode with platinum mesh (∼80 nm) below the STFO film (∼ 200 nm).

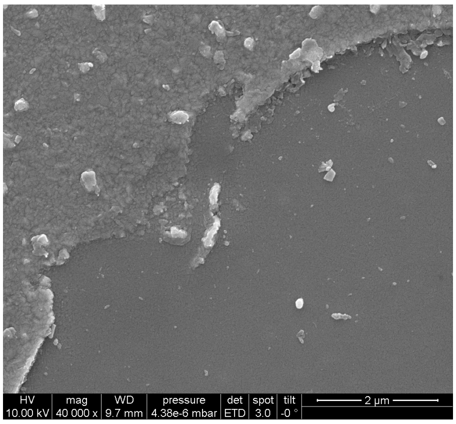

Figure 4.13: SEM image of the platinum mesh edge, covered with a ∼ 200 nm STFO film, no cracks are visible.

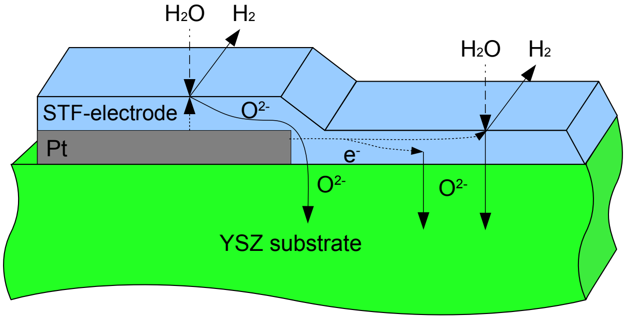

Figure 4.14: Reaction scheme for the electrode reactions with Pt thin film grid beneath the electrode.

(thin films), and shifts towards a reddish colour with increasing film thicknesss ($d_{\text{film}}$), visible in fig. 4.4. This coloration is in good agreement with the film thickness estimated by SEM images. Peak reflectivity is given at $\lambda_{max} = 2nd_{film}$ [30], where n is the refractive index. This concludes a film thickness ranging from around 100 nm (blue) for 20 min PLD deposition time to 200 nm (red) for 40-60 minutes deposition. Also changes in the surrounding atmosphere cause significant colouration changes to the electrode area above the metal grid. The cause of this is not yet fully understood, but might be due to changes in the refractive index, or different absorption properties due to oxygen nonstoichiometry and the contributing electronic defect concentrations.

### 4.4.1 Lateral ionic and electronic transport

Although it can be assumed, that with the metal grid beneath the electrodes, electronic transport is not the limiting factor in the low-frequency range at temperatures above 400 °C, some artifacts caused by electronic conduction are visible in the high to medium frequency range of the impedance. To investigate the influence of the metal grid size, both mesh types with 10 µm and 35 µm holes have been applied on one YSZ substrate to avoid a systematic error caused by degradation and different thin film samples. The impedance of both mesh types was measured at 450 °C. The two metal grid geometries in fig. 4.15 show a clear dependence of the HF-feature on the metal grid design. The resistive offset ($R_{\text{offset}}$) of this feature can be estimated by fitting the low and medium frequency part of the spectrum with an R1-(R2||CPE) element, and estimation via $R_{offset} \approx R1 - R_{YSZ}$. The ratio of the offset resistances for 10 µm and 35 µm mesh is in the region of 1:2.5-1:3.5, depending on the selected electrodes for comparison. If this feature is attributed to lateral electronic transport, the ratio is expected to be 1:3.5, according to the metal mesh size, which is in reasonable agreement with the experiment. The size of the low-frequency semicircle is showing relatively large scatter for different electrodes (The standard deviation is around 20%), with no distinct trend towards higher or lower resistance, depending on the mesh size. For better comparability, two measurements with similar surface reaction resistance were taken.

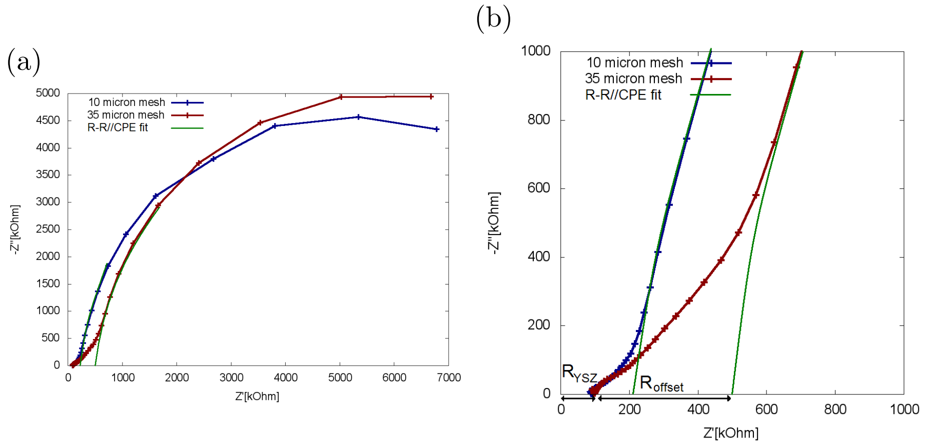

Figure 4.15: Effect of variations of the platinum mesh size on the high frequency impedance features at 450 ℃ and fit for estimation of the resistive offset, caused the high-frequency feature, mesh below the electrodes. (a): full spectra (b): magnification of the high-frequency part.

**Ionic transport** The dominating part of the impedance spectra at temperatures above 400 ℃ is the low-frequency semicircle. It is generated by chemical capacitance plus interfacial capacitance, and surface reaction resistance, according to the simplified equivalent circuit for mixed conducting electrodes [21], (fig. 3.11(b)). When the metal grid is placed on the bottom of the electrodes, the fraction of electrochemically active area is not easily determinable only by EIS. Lateral Electronic and ionic transport are causing similar features in the impedance spectra. Therefore it is not easy to conclude, whether the ionic conductivity is high enough to allow a reaction path on STFO above the metal grid, as depicted in fig. 4.14. While an interpretation over impedance measurements is difficult, an optical in-situ observation can be made: When a large positive or negative DC-bias (about ±400mV) is applied to the electrode, the colour of the electrode part above the platinum grid changes rapidly and homogeneously (fig. 4.16). The same colouration changes can be observed, when the oxygen partial pressure in the gas atmosphere is changed. This concludes, that the polarisation is spreading over the entire electrode area and ionic transport is fast enough, so that the entire electrode area is electrochemically active in the low frequency region.

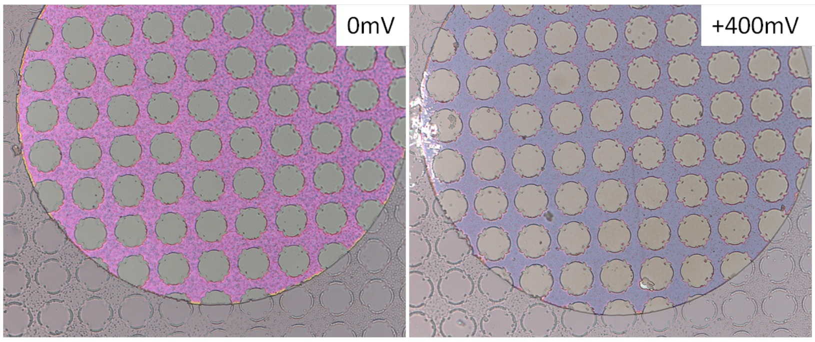

Figure 4.16: Reversible optical effects on the electrode colour with metal grid beneath the electrode when a DC-bias is applied. The photographs of the electrodes were taken at room temperature, with *"frozen in"* polarisation/defect chemistry.

Consequently, the chemical capacitance and surface resistance have to be normalised over the whole electrode.

### 4.4.2 Temperature dependence of surface and bulk properties

Fig. 4.17 shows the temperature dependence of the impedance spectra for an electrode with 20 minutes deposition time (~ 100 nm thickness) and 10 µm mesh after approximately 70 hours of degradation. Both, transport reactions and oxygen incorporation are thermally activated with different activation energies. Lateral electronic and ionic transport can not be separated, only the resistive offset consisting of both contributions can be estimated, as depicted in fig. 4.15, and explained in chapter 4.4.1. The resistance of the low-frequency semicircle was fitted with an R1-(R2||CPE) element, and the resistive offset caused by electronic and ionic transport was estimated as explained in fig. 4.15 and plotted in fig. 4.18. R2 is believed to be mainly caused by the surface reaction. It can clearly be seen, that the surface reaction, as well as the transport reactions are thermally activated. The activation energies for different elementary processes in the electrodes are shown in table 4.3.

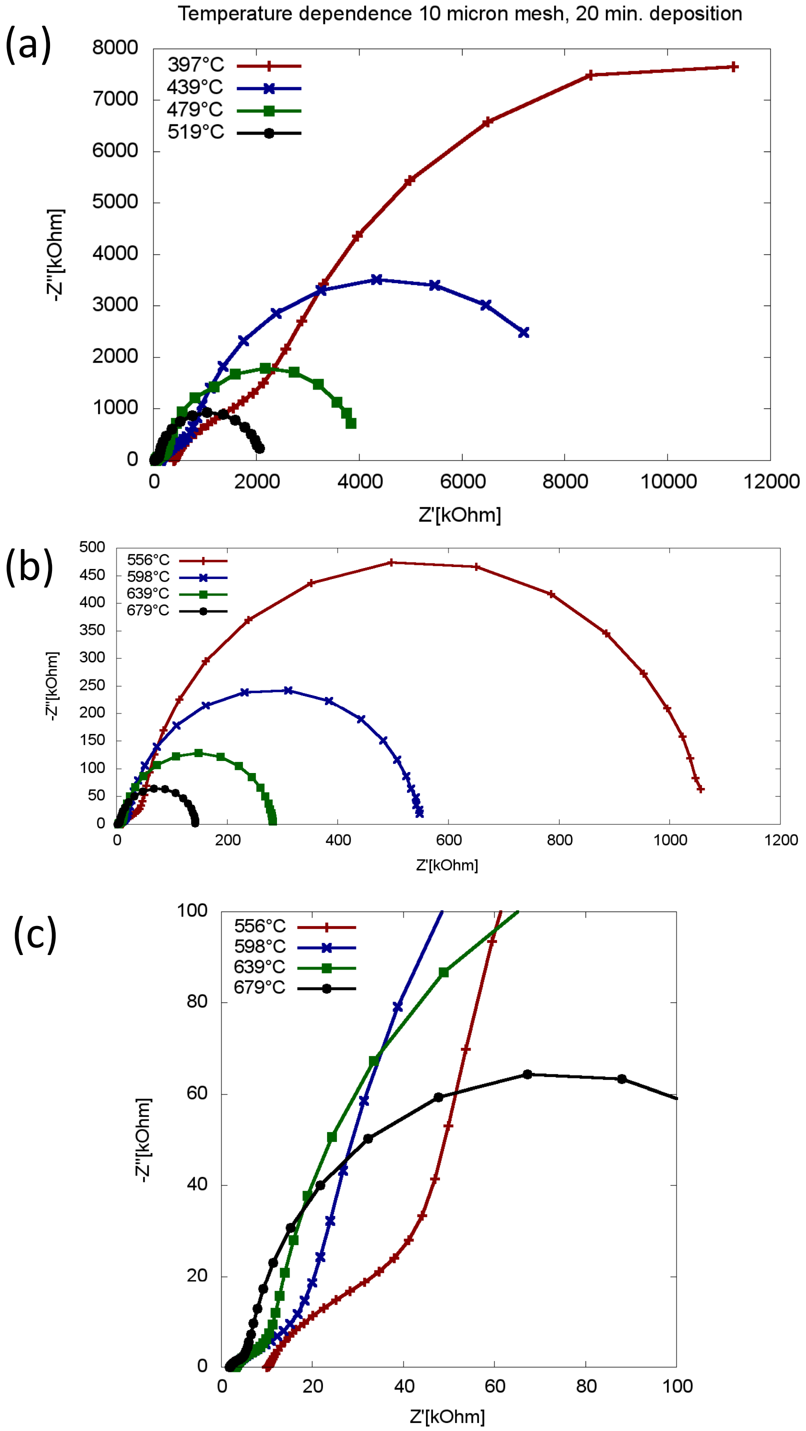

Figure 4.17: Impedance spectra measured at different temperatures on a 200 µm electrode with 10 µm Pt grid beneath the electrode, deposition time: 20 min (∼100 nm) (a): 397-519 °C, (b): 556-679 °C, (c): detail of the HF-features in (b).

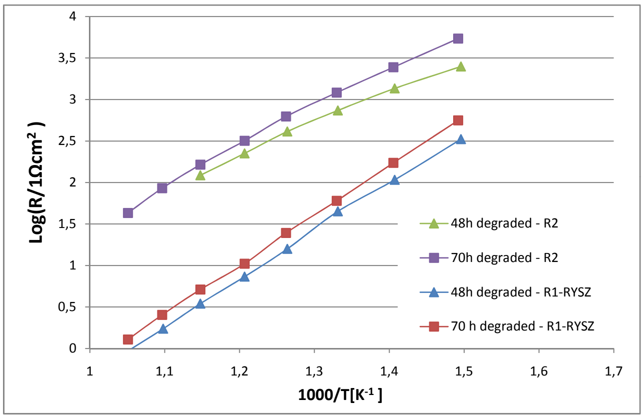

Figure 4.18: Arrhenius plot for different electrodes on a sample with 20 minutes deposition ($\sim 100\,\text{nm}$), metal grid ($10\,\mu\text{m}$ holes) below the electrode. The resistance values were normalised to the electrode area.

| process | activation energy (eV) |
|---|---|
| Low frequency process (R2) | |
| metal mesh beneath the electrode | 0.7-0.8 |
| metal mesh on top, T < 420 ℃ | 0.7-0.8 |
| metal mesh on top, T > 420 ℃ | 0.48-0.55 |
| metal mesh on top, degraded | 0.8 |
| High frequency process (R1-$R_{YSZ}$) | |
| metal mesh on top | 1-1.05 |

Table 4.3: Activation energies for oxygen incorporation and transport reactions.

### 4.4.3 Current-voltage characteristics

Typically, an electrochemical device has a strongly non-linear current-voltage characteristic. In liquid electrochemistry (at least at moderate overpotential), the reaction kinetics often follow the Butler-Volmer equation, which is based on the assumption, that a charge transfer is the rate limiting step, and that the overpotential drop is at the same location as the charge transfer. The second of these conditions can not hold true for MIEC electrodes. The rate limiting step is at the electrode surface, but an overpotential step can not occur relative to the insulating atmosphere The actual location of the overpotential step is discussed in section 5.1. A potential step between electrode and adsorbates may occur, which is discussed in detail in [31] for the oxygen exchange reaction in oxygen atmosphere. The rate determining step in this reference is assumed to be a charge transfer to an adsorbed oxygen species. A charge transfer reaction is also a possible RDS in hydrogen atmosphere. The measurement of reproducible DC-curves is an experimentally challenging task. When the voltage range is too low, non-linear effects, especially in the negative bias range, are hardly visible. When the voltage is

| T[°]C | $j^0[\mu A/cm^2]$ | $\beta_A$ | $\beta_B$ |
|---|---|---|---|
| 560 | 554 | 0.5 | 0.25 |
| 480 | 191 | 0.46 | 0.23 |

Table 4.4: Values for the generalised Butler-Volmer (equation 4.1).

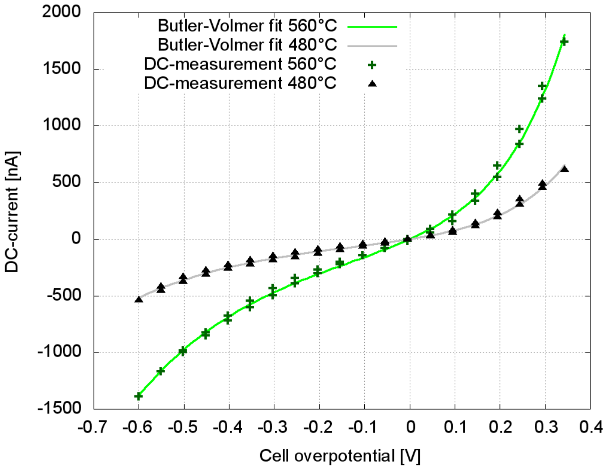

Figure 4.19: Typical DC-measurement within a reversible bias range, fitted with a generalised Butler-Volmer equation.

too high, the DC-curves show considerable hysteresis, with significantly improved kinetics after negative DC-bias. In the voltage range between $-0.6V$ and $+0.35V$, the DC-measurements are well reproducible, and show only minor hysteresis when several cycles are measured (only degradation can be observed). The measured DC-characteristics in this voltage range can be fitted with a generalised Butler-Volmer equation:

$$j = j^0 \left( exp\left(\frac{\beta_A F \eta}{RT}\right) - exp\left(\frac{-\beta_B F \eta}{RT}\right)\right) \tag{4.1}$$

The sum $\beta_A + \beta_B$ lies between 0.69 and 0.75, which is far away from the value of 2, proposed in [31], and also significantly smaller than 1, which would match the original Butler-Volmer equation. However, given the large amount of electrode bulk and surface parameters (such as: surface space charge potential, surface adsorbate coverage, Fermi level, ionic and electronic defect concentrations, . . . ) that are changed with DC-bias, it is not surprising, that the current-voltage characteristics do not follow one simple reaction model.

### 4.4.4 Electrode bulk and transport properties as function of DC-bias

When a DC-bias is applied to the electrode, the bulk oxygen partial pressure changes according to equation 2.16. This has a large influence on defect concentrations. According to the correlation between charge carrier concentration and conductivity $\sigma = |z|ec\mu^*_{e'}$, the electronic and ionic conductivity changes when a DC-bias is applied, under certain conditions and large bias/$p_{O_2}$ changes even by orders of magnitude. The ionic conductivity is assumed to increase proportionally to the amount of generated oxygen vacancies. In STFO, the oxygen vacancy concentration is predominantly controlled by the dopant amount, according to section 2.3.4. the relative change in oxygen vacancy concentration (within a moderate range of ±400 mV DC-bias) is small, and therefore large effects are not expected.

The concentration of conduction electrons increases, while holes decrease with negative bias, allowing an assumption on the type of electronic conduction. In a n-conductive oxide, electronic conductivity is assumed to grow with negative bias, and vice versa for a p-conductive oxide. In fig. 4.20, the DC-bias dependence of the impedance is shown. The resistive offset is caused by electronic as well as ionic transport processes, which makes a quantitative evaluation impossible, but qualitative interpretations can be made. As clearly visible in fig. 4.20, the resistive offset (R1-$R_{YSZ}$) significantly decreases with negative DC-bias, whereas for positive bias, it roughly stays the same size, or might grow (which can not be clearly interpreted). This, combined with the rather low electronic conductivity, leads to the assumption, that for reducing atmosphere, the electrode is in the n-conductive region, near to the intrinsic point of minimum electronic conductivity. This interpretation is in good agreement with the defect chemical model and conductivity isotherms proposed in [20] and [13] for bulk STFO.

### 4.4.5 Chemical capacitance as a function of temperature and DC bias

The theory of chemical capacitance was already explained in section 2.3.4. The $C_{chem}$ values were obtained by fitting an R1-(R2||CPE) element to the

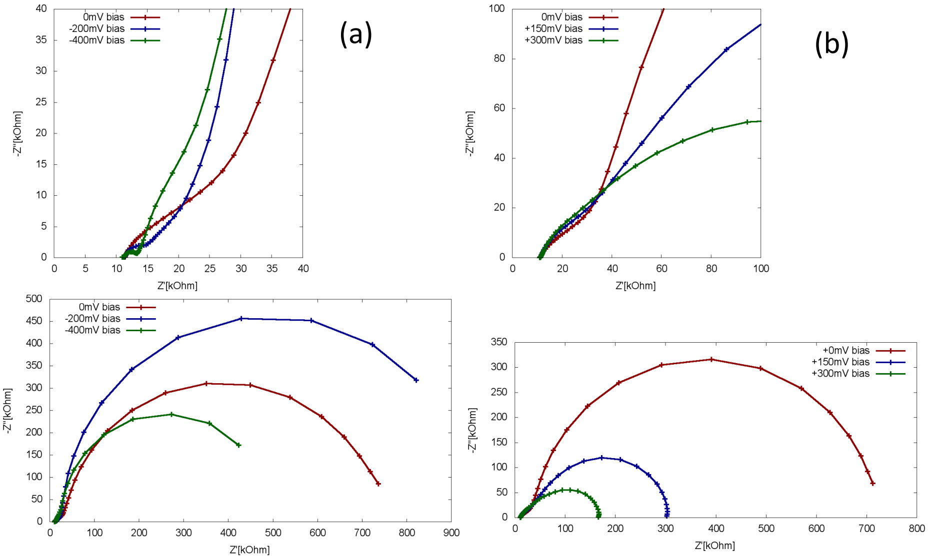

Figure 4.20: Impedance spectra at 555 ℃ with (a) negative and (b) positive DC bias, including a magnification of the high-frequency features, which are attributed to lateral transport losses. Deposition time: 20 minutes, (∼ 100 nm) meal grid (10 µm holes) beneath the electrode.

low-frequency part of the spectra, and calculation of the chemical capacitance via equation 3.3 and normalisation to the electrode volume. With this very simple fit, the sum of ionic double layer and chemical capacitance are fitted. Since the chemical capacitance is at least two orders of magnitude larger than a typical interfacial double layer capacitance, this effect can be neglected for STFO electrodes [32] [21]. The chemical capacitance was measured as a function of temperature and DC bias (see fig. 4.21). For each temperature point, three cycles were measured to prove good reproducibility. The overpotential is shown on a linear scale, whereas the chemical capacitance is plotted logarithmically. According to equation 2.13 the oxygen partial pressure in the electrode changes exponentially with the overpotential at the electrode.

$$p^{el}_{O_2} = p^{g}_{O_2} e^{\frac{4F\eta}{RT}} \frac{4F\eta}{RT} = \ln(\frac{p^{el}_{O_2}}{p^{g}_{O_2}})$$

Therefore, the x-axis can also be interpreted as a logarithmic scale for the oxygen partial pressure, as in a Brouwer diagram. If one electronic defect

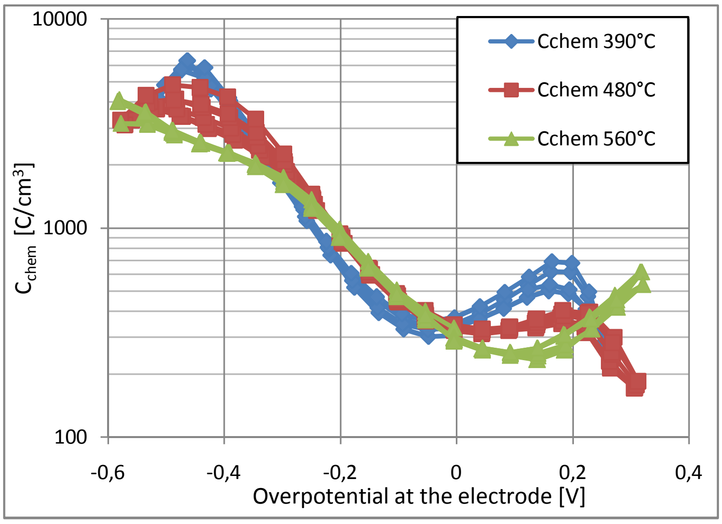

Figure 4.21: Temperature and DC-bias dependence of the chemical capacitance at 390-560 °C.

type is limiting the chemical capacitance in a certain partial pressure range, straight lines are expected. However, the measured chemical capacitance shows a strong dependence on the DC-bias with a minimum around $\eta = 0$. An increase in temperature only leads to a shift of the minimum towards more anodic overpotential, and a slightly shallower profile, but has only little effect on the magnitude of the minimum. This leads to the conclusion, that the chemical capacitance is not thermally activated, but is depending on the chemical potential of oxygen and electrons. High temperature typically leads to more reducing conditions even at zero potential. This may explain the horizontal shift of the curves for different temperatures. The steep drop of the chemical capacitance for anodic overpotential over +0.3 V may be attributed to a transport limitation, which reduces the polarised area, or to complications in the fitting routine, since new features appear in the spectra, which can not be explained so far.

**Electronic charge compensating mechanism** The positive charge of the oxygen vacancies generated in the chemical capacitance mechanism has to be compensated by formation and annihilation of electronic defects. The negative slope in the cathodic region suggests, that negatively charged defects are the dominant charge compensation mechanism in this regime, where the positive slope for anodic bias suggests positively charged defects in this regime. This observation, combined with the previously made assumption, that the STFO-film is near the intrinsic point of minimum electronic conductivity, might indicate, that conduction electrons and holes are the charge compensating mechanism. However, there are two reasons, why this can not hold true.

- **Carrier concentration**
  Even though the approximation for dilute situations is not fulfilled, equation 2.23 can be used to estimate the order of magnitude of the compensating carrier concentration. According to this equation, the ionic chemical capacitance can be estimated with the assumption $[V_O^{\bullet\bullet}] \approx [Fe_{Ti}^{'}] \approx [Fe_{tot}]/2$, revealing $C_{chem,O^{2-}} \approx 18000\, Fcm^{-3}$, which is far larger than the total chemical capacitance, allowing the approximation $C_{chem.tot} \approx C_{chem,electron}$. Then the carrier concentration can be estimated as $c \approx C_{chem}\frac{k_bT}{(ze)^2}$ (equation 2.23), revealing a minimum value of $c_{min} \approx 10^{20}\, cm^{-3}$ for z = 1. Such a high value of conductive electrons/holes would imply high electronic conductivity, which is barely measureable with EIS. In [20], the mobility of conduction electrons in bulk STFO (35 mol% Fe) was measured as $\mu_e^* \approx 2.5\, cm^2V^{-1}s^{-1}$ at 560 °C, which would lead to $\sigma_{el} = e\mu_e^*[e^{'}] \approx 40\, Scm^{-1}$. With this conductivity value, only minor (if any) sheet resistance would be observable even without an applied platinum grid.

- **Thermal activation**
  The concentration of conduction electrons and holes is thermally activated, which also leads to the thermal activation of electronic conduction. Therefore, a chemical capacitance generated by conduction electrons would have to be thermally activated. The measured chemical capacitance, on the other hand, is not at all thermally activated.

**Localised electronic defects** The low electronic conductivity of STFO thin films indicates a very low concentration of conduction electrons or holes.

Therefore these defects can not be the dominant electronic charge compensation mechanism for the rather large chemical capacitance. The only mechanism that can explain all observations so far is a concentration change in localised electronic defects, which is probably either attributed to a change in the iron oxidation state, or electron trapping in oxygen vacancies, which could both explain the measurements. Thermodynamically, there is no difference between localised and delocalised defects, only the electronic conductivity is not influenced by them. The measurements therefore confirm the assumptions from chapter 2.3.4.

### 4.4.6 Irreversible effects: large DC bias

When a large anodic bias, up to +1V, is applied, only little changes in the electrode performance appear. A large cathodic DC-bias, on the other hand, causes very strong increase in catalytic activity. Such a large cathodic bias was applied to a heavily degraded electrode with a very slow ramp of several hours. Afterwards, a small bias within the reversible range was applied. Compared to the initial value, a decrease of the dc resistance by more than two orders of magnitude could be observed, leading to a resistance even lower than for undegraded electrodes. Also, the shape of the spectra

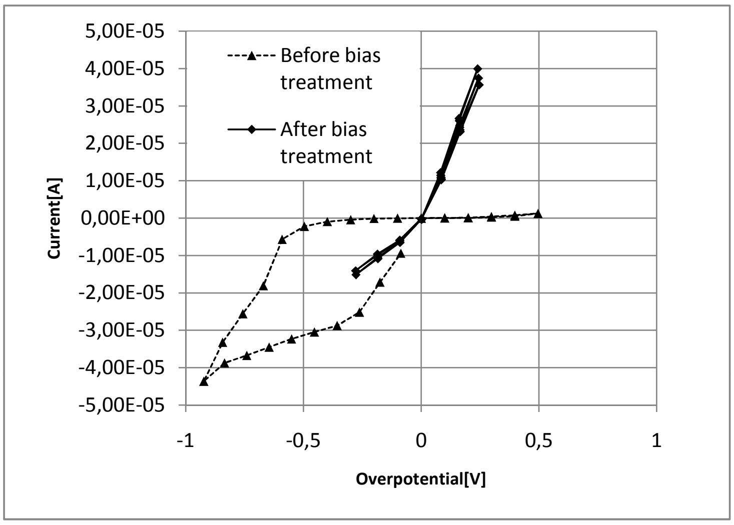

Figure 4.22: Current-voltage characteristics before and after an irreversible cathodic DC-bias treatment.

changes, and a drastic increase in the chemical capacitance and a strong change in the DC-behaviour could be observed. The large bias may even lead to a decomposition of the material and segregation of different phases. No mechanistic interpretation of this phenomenon can be found so far. For $La_{0.6}Sr_{0.4}Co_{0.8}Fe_{0.2}O_{3-\delta}$ microelectrodes (used as cathodes in oxygen atmosphere), a similar effect could be observed and correlated to a change in the chemical composition at the surface [33].

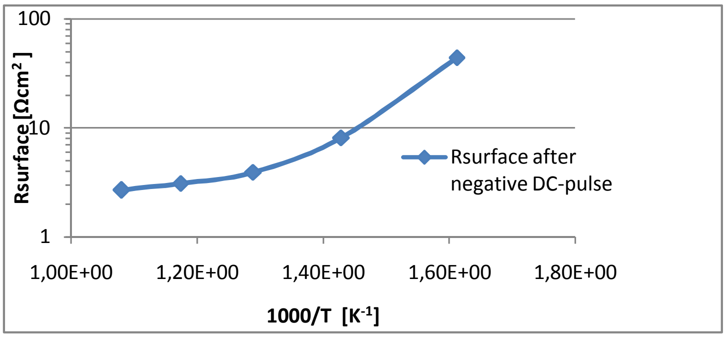

Figure 4.23: Arrhenius plot of the ASR of an electrode after a large negative DC-bias (-1.3 V for 30 minutes).

**Unconventional temperature dependence** The measurement in fig. 4.23 was carried out on an electrode after applying a large negative DC bias of -1.3 V (at the electrode) for 30 minutes at 670°C. Virtually no thermal activation of the oxygen exchange reaction is observed in the temperature range of 500 to 650°C. ($\sim 0.14\,eV$), whereas in the low-temperature range, an activation energy of $\sim 0.6 - 0.7\,eV$ can be estimated. This value is comparable to the activation energy of the surface process for degraded electrodes.

# 5 New electrode and metal grid design for quantitative evaluation

In order to quantify and separate the different contributions to the polarisation resistance more accurately, a novel electrode design and measurement mode were developed. Before results can be discussed in section 5.5, a thorough discussion of the polarisation and transport phenomena in mixed conducting electrodes has to be made. For thin film microelectrodes with a specifically designed metal grid as a current collector, an electrochemically motivated equivalent circuit can be derived and used for fitting of the measured spectra.

## 5.1 Electrical and chemical driving forces for transport, polarisation and chemical reactions

In mixed conducting electrodes, stoichiometric polarisation leads to simultaneous change in electronic and ionic defect concentrations. An identification of the exact driving force for polarisation and transport phenomena occurring in a mixed conducting electrode is crucial for the development of equivalent circuits and may lead to unexpected results.

**Stoichiometric polarisation of a blocked electrode** As already explained in section 2.1.1, application of an overpotential ($\eta$) to a working electrode with blocked surface path changes the electrochemical potential of electrons by $-F\eta$.

$$\begin{aligned}
&\Delta\tilde{\mu}_{O^{2-}} = 0\\
&\Delta\tilde{\mu}_{e^-} = -F\eta\\
&\Delta\tilde{\mu}_{O^{2-}} - 2\Delta\tilde{\mu}_{e^-} = \Delta\mu_{O^{2-}} - 2\Delta\mu_{e^-} = 2F\eta
\end{aligned}$$

When the charge neutrality condition and the assumption from section 2.3.4 of comparatively large ionic chemical capacitance is applied, an interesting conclusion can be made:

$$\Delta[O^{2-}] = -\frac{1}{2}\Delta[e^-] \tag{5.1}$$

$$\frac{\partial \mu_{O^{2-}}}{\partial c} \ll \frac{\partial \mu_{e^-}}{\partial c}$$

$$\Delta\mu_{e^-} \approx -F\eta \tag{5.2}$$

$$\Delta\mu_{O^{2-}} \ll F\eta \tag{5.3}$$

$$F\Delta\varphi = \Delta\mu_{e^-} - \Delta\tilde{\mu}e^- \ll F\eta \tag{5.4}$$

The electrostatic potential of an electrode remains almost unchanged, when a bias is applied. The overpotential is (mainly) located to the interface between electrode and metallic contact. The chemical potential of electrons (which is synonymon for the Fermi level) is changed by application of an overpotential. Consequently, the contact potential to the metal contact changes.

In section 5.2, it will be shown, that for a STFO thin film electrode only lateral electronic and ionic transport processes cause relevant losses, and vertical transport processes can be considered lossless. The electrochemical potential of electrons and oxygen ions is therefore a function of only the lateral position ($x$) at the electrode. In mixed conductors with low ionic conductivity, this is not always the case.

### 5.1.1 Driving forces for electrochemically driven transport reactions

When a real STFO microelectrode with metal grid on bottom (figure 4.14) is considered, lateral transport losses - and hence their driving forces - can not be neglected. Electrochemically driven transport reactions may be driven by an electric field or a concentration gradient. In the linear regime, the current density of a species x equals a pre-factor ($\beta$) times the gradient in the electrochemical potential: [15]

$$j_x = \beta_x \nabla\tilde{\mu}_x = \beta_x(\nabla\mu_x + z_e F \nabla\varphi) \tag{5.5}$$

When j shall have the dimension of an electric current density, $\beta$ can easily be calculated by the ohmic law.

$$j_x = \frac{-\nabla \mu_x}{z_e F R_{sheet}} - \frac{\nabla \varphi}{R_{sheet}} \qquad \beta = \frac{-1}{z_e F R_{sheet}} \tag{5.6}$$

In the case of thin film electrodes, it is more useful to integrate the current density over the film thickness, which reveals dimension of $[j] = \frac{A}{cm}$ for the current density and $[R_{sheet}] = \Omega$ for the sheet resistance.

**Driving force for electronic transport** In the YSZ below the electrode, the electrochemical potential of oxygen ions is homogeneous. Consequently, no gradient in the electrochemical potential of oxygen ions ($\nabla O^{2-}$) can occur in the electrode region grown on YSZ. Electronic current is driven by a gradient in the electrochemical potential of electrons ($\nabla \tilde{\mu}_{e^-}$). Since the electrostatic potential is almost unchanged in this region, the driving force is a gradient in the pure chemical potential of electrons. With an electric current density $j$ and an electronic sheet resistance $R_{sheet,el}$, equation 5.6 can be used to calculate the current density and driving force ($z_e = -1$ for electrons).

$$2F\Delta\varphi = \Delta\mu_{O^{2-}} - \overbrace{\Delta\tilde{\mu}_{O^{2-}}}^{=0} \ll F\eta \tag{5.7}$$

$$2F\nabla\varphi = \nabla\mu_{O^{2-}} \approx 0 \tag{5.8}$$

$$F j_{el} R_{sheet,el} = \nabla\tilde{\mu}_{e^-} \approx \nabla\, \mu_{e^-} \tag{5.9}$$

In this region, no electrostatic overpotential is present, and the electronic current is driven by a gradient in the electron concentration (which is leading to a gradient in the chemical potential). A similar situation can be found in experiments using Wagner-Hebb-polarisation, where the ionic charge carrier is blocked on one electrode, leading to $\nabla\tilde{\mu}_{O^{2-}} = 0$ (as the steady state condition).

**Driving force for ionic transport** In the electrode region above the metal grid, the electrochemical potential of electrons is laterally homogeneous, and a gradient in the electrochemical potential of oxygen ions is causing the transport.

$$\nabla \tilde{\mu}_{e^-} = \nabla \mu_{e^-} - F \nabla \varphi = 0 \tag{5.10}$$

$$F \nabla \varphi = \nabla \mu_{e^-} \gg \nabla \mu_{O^{2-}} \tag{5.11}$$

$$2F j_{ion} R_{sheet,ion} = \nabla \mu_{O^{2-}} - 2F \nabla \varphi \approx -2F \nabla \varphi \tag{5.12}$$

Therefore, in this region of the electrode, even though a metallic conductor is present, the ionic current is field-driven. Electronic transport has no driving force in this region, because the electric field is equal to the gradient in the chemical potential of electrons. A similar situation is found in a *p-n* junction in semiconductors where diffusive and field driven current compensate each other, though the electrical field can be in the order of $10^7 \frac{V}{m}$ in equilibrium conditions [17].

### 5.1.2 Effective cell polarisation and transport losses

In the location of the metal grid border ($x = 0$), electronic and ionic transport paths in the electrode are short and cause negligible losses. In this region, full stoichiometric polarisation occurs, according to equation 5.1. In order to take account of transport losses, a polarisation potential ($\eta^*$) has to be introduced, which is the driving force of stoichiometric polarisation (and hence surface reaction and chemical capacitance mechanism).

$$Fj_{el}R_{sheet,el} = \nabla\tilde{\mu}_{e^-} \tag{5.13}$$

$$\Delta\tilde{\mu}_{e^-}(x) = \int\limits_0^x Fj_{el}R_{sheet,el} - F\eta \tag{5.14}$$

$$2Fj_{ion}R_{sheet,ion} = \nabla\tilde{\mu}_{O^{2-}} \tag{5.15}$$

$$\Delta\tilde{\mu}_{O^{2-}}(x) = \int\limits_0^x 2Fj_{ion}R_{sheet,ion} \tag{5.16}$$

$$\Delta\tilde{\mu}_{O^{2-}} - 2\Delta\tilde{\mu}_{e^-} := 2F\eta^* = 2F\eta - \int\limits_0^x 2Fj_{ion}R_{sheet,ion} - 2\int\limits_0^x Fj_{el}R_{sheet,el} \tag{5.17}$$

$$\eta^* = \eta - \int\limits_0^x j_{ion}R_{sheet,ion}dx - \int\limits_0^x j_{el}R_{sheet,el}dx \tag{5.18}$$

The effective polarisation potential is therefore the applied voltage minus transport losses attributed to electronic and ionic transport. The dimension of $\eta^*$ is volts, but it can not be mapped to an electrostatic potential. In an STFO electrode with metal grid on bottom, transport losses are either purely ionic (in the region above the metal grid) or purely electronic (in the region above YSZ).

**Conclusions for construction of a physically derived equivalent circuit** Electrical and chemical driving forces for electronic and ionic transport are phenomenologically indistinguishable, and can be treated with Ohm's law. Also, the driving forces for surface oxygen exchange and chemical capacitance ($\eta^*$) is simply the applied voltage minus electronic and ionic transport losses.

## 5.2 Equivalent circuits modelling electronic and ionic transport in thin films

As shown above, the interpretation of impedance measurements of electrodes with low electronic conductivity is rather complicated, which is mainly caused by lack of knowledge of the actual current path. Nevertheless, it is possible to describe and calculate the current and potential distribution, when a specific electrode and metal grid design is used. For a planar thin film that is electrically contacted via long and thin metal fingers placed on top or beneath the electrode, electronic and ionic transport only takes place in one lateral and vertical direction, reducing the reaction model to two dimensions. The according reaction scheme can be seen in fig. 4.7 and 4.14 in sections 4.3 and 4.4. Considering the electronic transport resistance of such a thin film electrode with a lateral transport path of length l, and film thickness d, one can estimate, that $R_{electron,lateral} \propto \rho\frac{l}{d}$, where $\rho$ is the specific electronic resistance. Vertical electronic transport losses are proportional to $R_{electron,vertical} \propto \rho\frac{d}{l}$. When the smallest lateral feature is more than ten times larger than the electrode thickness, electronic transport losses in vertical direction can be neglected with an error smaller than 1%. For thin film microelectrodes this approximation is valid, since the smallest lateral feature size is around 5 µm, limited by standard photolithographic techniques, and the typical thickness of a thin film model electrode is 50-400 nm. This leads to a quasi-one dimensional equivalent circuit, where only lateral electronic transport losses are measurable. When terminal parts are neglected, the circuit is a transmission line, consisting of an ohmic series resistance $R_s$ that represents the electronic sheet resistance, and a parallel admittance. The parallel admittance is a more complicated element, including the electrochemical surface reaction, the chemical capacitance, and eventually other features such as an electrode/electrolyte interface, or even vertical ionic transport within the film. However, for the following calculations, it will remain on a symbolic level as $Y_p$. This circuit is based on the mixed conductor theory proposed by [21]. The lateral dimension of the circuit can be interpreted as the lateral dimension of a thin film electrode, whereas the vertical dimension does refer to different charge carriers and their reactions, and can not be directly mapped to a spatial coordinate. The electronic rail stands for the electronic current and transport losses in the sheet. The ionic YSZ potential is symbolising the electrochemical potential of oxygen ions in the YSZ substrate near the electrode. An electrical short circuit in this part implies the simplification, that the electrochemical potential of oxygen is assumed to be homogeneous directly beneath the electrode, therefore an

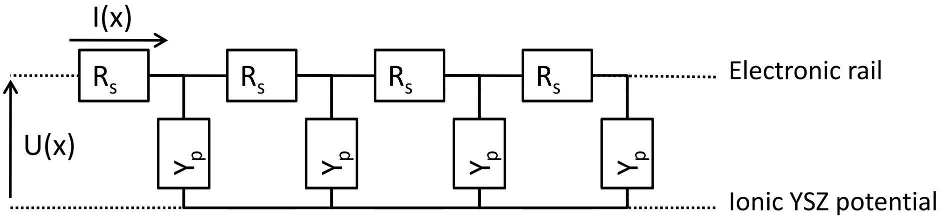

Figure 5.1: Generalised transmission line circuit without terminal parts, the names 'electronic rail', and 'ionic YSZ potential' symbolize the meaning of the corresponding elements for STFO electrodes.

ohmic spreading resistance against the counter electrode has to be treated separately from the electrode circuit. The voltage $U(x)$ is the polarisation overpotential, according to equation 5.18. When no boundary conditions are set, current and voltage distribution can be calculated as follows:

$$I'(x) = -Y_p U(x) \qquad U'(x) = -R_s I(x) \tag{5.19}$$

These equations can easily be solved by differentiating the right equation and inserting $I'(x)$.

$$U''(x) = Y_p R_s U(x) \tag{5.20}$$

$$\tag{5.21}$$

Every linear, ordinary differential equation with constant coefficients can by solved with an exponential ansatz: $U(x) = Ce^{\gamma x}$.

$$\gamma^2 C e^{\gamma x} = Y_p R_s C e^{\gamma x} \tag{5.22}$$

$$\gamma_{1,2} = \pm\sqrt{Y_p R_s} \tag{5.23}$$

$$U(x) = Ae^{\sqrt{Y_p R_s} x} + Be^{-\sqrt{Y_p R_s} x} \tag{5.24}$$

The parameters A and B are depending on the electrode geometry and the variant of the electrical contact.

## 5.3 Electrode geometry and resulting equivalent circuits

The goal of the electrode and metal grid design is to achieve a current distribution that can be modelled with the quasi one-dimensional equivalent circuit in fig. 5.1. This model would be exactly valid for an STFO electrode contacted by infinitely long metal stripes. In order to achieve a good approximation to this idealised model, a rectangular electrode with intermeshing comb-shaped metal contacts was used, as shown in fig. 5.2

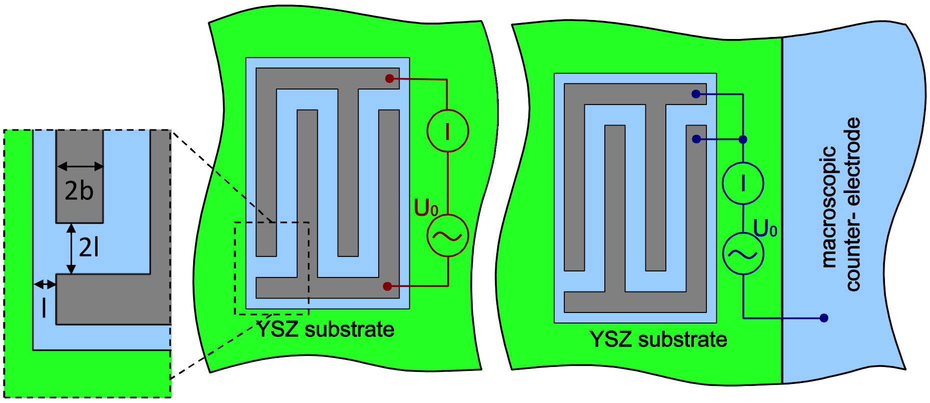

Figure 5.2: Schematic electrode design with (left) asymmetric and (right) symmetric applied voltage.

The fact that two separated metal combs are placed on one electrode allows a new measurement method for thin film electrodes. The combs can either be contacted in parallel, where (for low frequencies) mainly the oxygen exchange resistance is measured, like in conventional impedance spectroscopy (fig. 5.2, right). The voltage can also be applied between the combs, where (for low frequencies) predominantly the electronic resistance is measured. The proposed transmission-line shaped equivalent circuit (fig. 5.1) is valid for both measurement methods, only the boundary conditions are different. Therefore the elements of the equivalent circuit and their numerical values remain the same. Both measurements can be carried out on the same electrode.

### 5.3.1 Boundary conditions of the transmission line circuit

With a metal finger distance of $2l$ and symmetric applied voltage, the parameters A and B from equation 5.24 can be calculated. The point $x = 0$ is defined as the middle between the metal fingers. For symmetric applied voltage, the following boundary conditions are set:

$$U_{sym}(-l) = U_{sym}(l) = U_0 \tag{5.25}$$

Since l is not further specified, this is the definition of a symmetric function, which leads to $A = B$, or a hyperbolic cosine function.

$$A = B \tag{5.26}$$

$$U_{sym}(l) = U_0 \tag{5.27}$$

$$U_{sym}(x) = U_0 \frac{\cosh \gamma x}{\cosh \gamma l} \tag{5.28}$$

$$I_{sym}(x) = \frac{-dU}{R_s dx} = U_0 \frac{-\gamma \sinh \gamma x}{R_s \cosh \gamma l} \tag{5.29}$$

For asymmetric applied voltage, the boundary conditions slightly change:

$$U_a(-l) = -U_a(l) = U_0 \tag{5.30}$$

This is the definition of an asymmetric function, leading to $A = -B$, or a hyperbolic sine function.

$$A = -B \tag{5.31}$$

$$U_{asym}(l) = U_0 \tag{5.32}$$

$$U_{asym}(x) = -U_0 \frac{\sinh \gamma x}{\sinh \gamma l} \tag{5.33}$$

$$I_{asym}(x) = \frac{-dU}{R_s dx} = U_0 \frac{\gamma \cosh \gamma x}{R_s \sinh \gamma l} \tag{5.34}$$

Experimentally, the impedance for symmetric and asymmetric driving voltage can be measured by Electrochemical impedance spectroscopy.

$$Z_{asym} = \frac{U_0}{I_{asym}(-l)} = \frac{R_s}{\gamma} \tanh(\gamma l) \tag{5.35}$$

$$Z_{sym} = \frac{U_0}{I_{sym}(-l)} = \frac{R_s}{\gamma} \coth(\gamma l) \tag{5.36}$$

$$\frac{Z_{asym}}{Z_{sym}} = (\tanh \gamma l)^2 \tag{5.37}$$

If the electrochemical reactions can be described with one single transmission line, these quantities are sufficient to calculate $\mathrm{Y_p}$ and $\mathrm{R_s}$.

$$\gamma = \frac{\operatorname{artanh}\left(\sqrt{\frac{Z_{asym}}{Z_{sym}}}\right)}{l} \tag{5.38}$$

$$R_s = Z_{asym} \gamma \coth \gamma l \tag{5.39}$$

$$Y_p = \frac{\gamma^2}{R_s} \tag{5.40}$$

These equations allow an ab initio calculation of the parallel admittance and sheet resistance, without the need of a specific equivalent circuit for $Y_p$. Mathematically, these equations are valid for any measured spectrum, and are independently applicable for every measured frequency. However, the only physically meaningful interpretation of the $\mathrm{R_s}$ element is a perfect, frequency-independent resistor. If application of the equations above does not deliver a simple resistor's impedance, a single transmission line does not describe the actual electrode reactions. The value of $real(\gamma l)$, which can be interpreted as the ratio between half of the finger distance ($l$) and electronic diffusion length ($real(\frac{1}{\gamma})$), is a measure for the difference of symmetric and asymmetric measurement. For $real(\gamma l) \lessapprox 1$, the measurements are clearly distinguishable, but for $real(\gamma l) \gg 1$, the approximation $\coth(\gamma l) \approx \tanh(\gamma l) \approx 1$ becomes valid, resulting in $Z_{sym} \approx Z_{asym}$.

### 5.3.2 Simulated Spectra

For a simple picture, the equivalent circuit for $Y_p$ was chosen to be a simple $\mathrm{R_p}\|\mathrm{C_p}$ element. In this case, the transmission line is a finite length Gerischer element (see fig. 3.13). According to dimensional analysis, only one characteristic dimensionless number influences the shape of the spectra:

$$\gamma(\omega = 0)l \;=\; \sqrt{\frac{R_s}{R_p}}\, l \tag{5.41}$$

The symbols $\mathrm{R_s}$ (sheet resistance) and $\mathrm{R_p}$ (area specific parallel resistance) are according to fig. 3.13. $\gamma(\omega = 0)l$ is the ratio between half of the finger distance (l) and the electronic diffusion length in the DC-case ($\gamma$). In fig. 5.3,

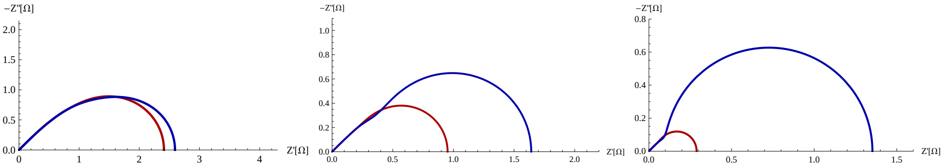

$\gamma l = 2$ $\gamma l = 1$ $\gamma l = 0.5$

Figure 5.3: Simulated spectra of a generalised transmission line with an $\mathrm{R_p}\|\mathrm{C_p}$ element for $\mathrm{Y_p}$ (finite length Gerischer) for symmetric (blue) and asymmetric (red) applied voltage, with varying ratio in $\mathrm{R_s}/\mathrm{R_p}$.

the influence of the parameter $\gamma l$ on the shape of the impedance spectra is clearly visible. When the electronic diffusion length becomes much smaller than the metal finger distance, $\mathrm{Z_{sym}}$ and $\mathrm{Z_{asym}}$ converge against the solution for an infinite finger distance, which would be a Gerischer element in this case. For high frequencies, the additional capacitive current path reduces the electronic diffusion length, and leads to overlapping spectra. In this frequency region, only the electrode region near the metal finger edges is electrochemically active. Overlapping spectra in the high frequency region occur for any equivalent circuit and parameter set, as long as a direct capacitive path is part of the $Y_p$ element. On circular microelectrodes without metal grid, the YSZ resistance is independent of the electrode diameter (see section 4.1), which can be explained by a localisation of the electrochemical current path near the electrical contact in the high frequency region.

### 5.3.3 Modelling of equivalent circuits for real microelectrodes

When dealing with a real microelectrode, more effects have to be considered. Electrochemical reactions also take place in the region of the platinum grid, which is placed on top or beneath the electrode.

**Investigation of electrodes with small statistical deviations** When the statistical deviation of different microelectrodes is very small (which is not the case for STFO electrodes), the unknown additional current at the platinum fingers can be eliminated by varying the finger distance. The electrochemical reactions and transport processes in the region of the metal grid is independent of the finger distance. Therefore also the impedance contributions from this electrode part remain equal when the finger distance is changed. Therefore the difference in admittance for two metal finger distances eliminates the current contributions from the electrode parts covered with platinum. When two different metal grid geometries are used, with the metal finger distance of l and 2l, $\gamma$ (and therefore $\mathrm{R_{sheet}}$ and $\mathrm{Y_p}$ with equation 5.39 and 5.40) can be calculated numerically over:

$$\frac{Y_{asym}(l) - Y_{asym}(2l)}{Y_{sym}(2l) - Y_{sym}(l)} = \frac{\coth(\gamma l) - \coth(2\gamma l)}{\tanh(2\gamma l) - \tanh(\gamma l)} \tag{5.42}$$

So far, the equations above are independent for every measured frequency point and do not propose a specific circuit for the parallel admittance and the electrochemical reactions over the metal grid, which makes this model a very beautiful one.

**Investigation of microelectrodes with significant statistical deviation** Typical STFO microelectrodes have a rather large statistical deviation. In this case, subtraction of two admittance values also contains the statistical deviations of the two electrodes, making the above mentioned model not applicable. Instead, an explicit circuit for the $Y_p$ element, and for the electrode part over the metal grid has to be derived. With an explicit equivalent circuit, one electrode is sufficient for fitting, and variations in geometry are helpful to prove (or disprove) a proposed reaction model. This is the best applicable method in the case of STFO electrodes.

**YSZ resistance** When the DC-case is considered, ohmic losses in the YSZ substrate occur when symmetric voltage is applied. Therefore, the YSZ resistance can be modelled as a resistive offset. For asymmetric voltage, on the other hand, the current path is predominantly electronic in the DC-case, and the YSZ resistance does not play a role. This consequently means, that the YSZ resistance has to be modelled differently, whether symmetric or asymmetric voltage is applied.

### 5.3.4 Photo mask used for structuring of the electrodes

As a part of this work, a photomask was designed to produce microelectrodes and metal grid in a design as sketched in fig. 5.2. The drawings of the microelectrodes and metal grid are shown in fig. 5.4. Electrode and metal grid have to be aligned with high precision (ideally with an error below 2 µm). The cross-hair styled structures at the electrode edges are position markers on which even very small deviations from a perfect alignment can be detected under an optical light microscope. The macroscopic counter-electrodes are visible at the sides of the substrates.

### 5.3.5 Full equivalent circuit for metal fingers beneath the electrode

With metal combs beneath the electrode, the whole electrode area is in exchange with the gas atmosphere, but it depends on the electronic and

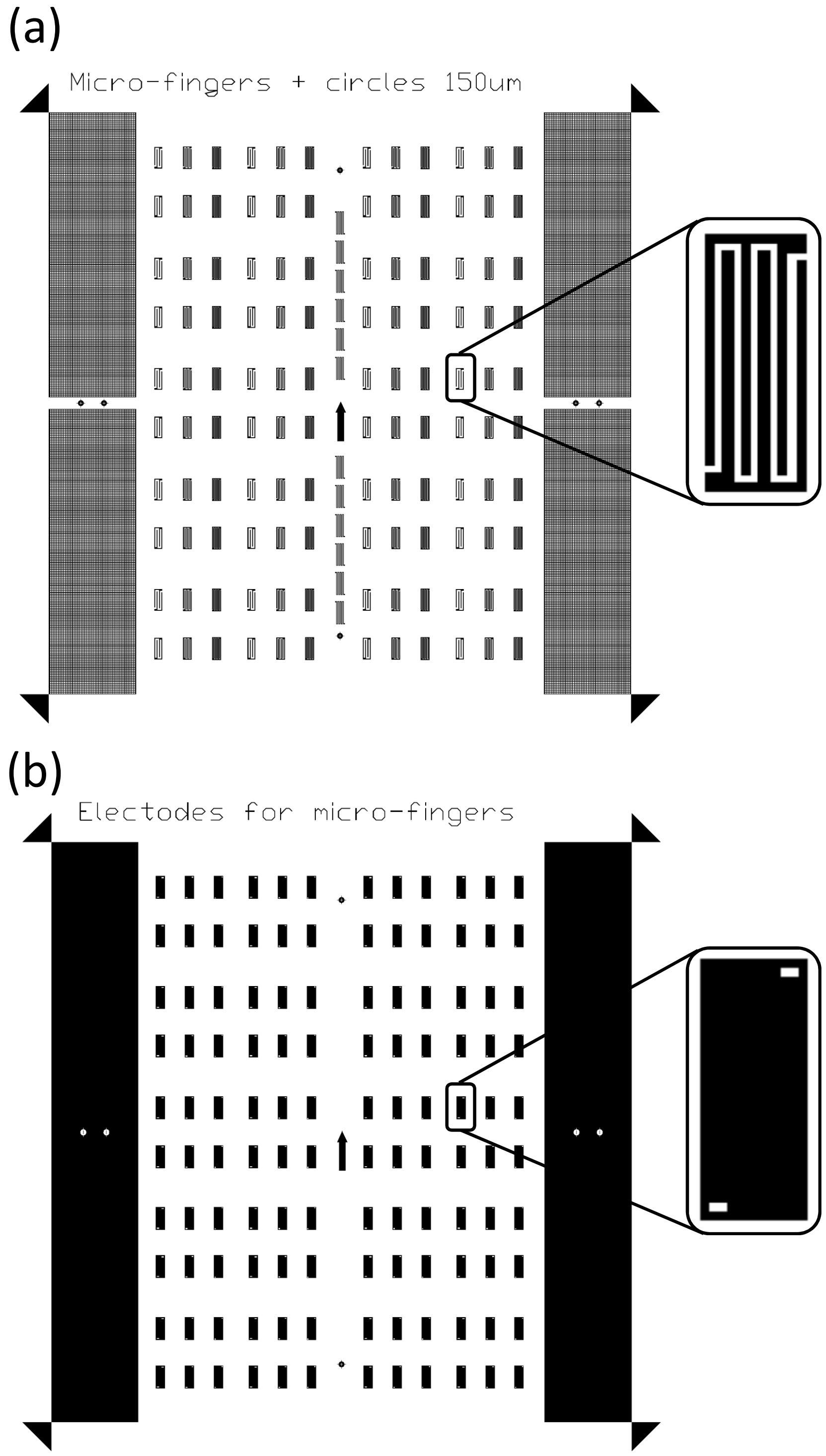

Figure 5.4: Drawing of the photolithographic mask, containing the design for electrodes and metal fingers (a): Metal grid structure (b): STFO-electrode structure.

ionic conductivity, how much of the surface area is electrochemically active. For quantitative evaluation of the electrode properties, a specific equivalent circuit for $Y_p$ and also for the region over the platinum grid has to be derived.

**Region above the YSZ substrate** In this region, lateral electronic transport ($R_{electron}$) and electrochemical reactions can be modelled with a generalised transmission line equivalent circuit. The $Y_p$ element is modelled with the simplified equivalent circuit for electrodes with high ionic conductivity by J.Jamnik and J.Maier[21] (fig. 3.11).

**Region above the metal grid** In the region over the metal grid, lateral electronic transport can occur in the metal and can therefore be considered lossless (vertical transport losses can be neglected). Oxygen ions have a lateral transport path in the electrode, causing ionic transport losses in this region. This can be modelled with an additional transmission line with lossless electronic and resistive ionic transport. The $\mathrm{Y_p}$ element in this case can be modelled as a simple $\mathrm{R}\|\mathrm{C}$ element, consisting of $\mathrm{R_{redox}}$ and $\mathrm{C_{chem}}$, because an ionic interface is physically not existent. Also, a double-layer capacitance, caused by the YSZ-Pt interface ($C_{dl}$) has to be considered. Oxygen ions, which are incorporated above the metal grid also have to pass the ionic YSZ-STFO interface. An exact solution of this phenomenon can not be found analytically, but an approximation can be applied. When this interfacial transport process is modelled as a transmission line with $R_{ion}$ as serial resistance and $R_{int}$ as the (area specific) parallel resistance, the interfacial transport can be modelled by $R_{int2} = \sqrt{R_{ion}R_{int}}$, according to [21].

**YSZ resistance** As mentioned earlier, the YSZ resistance is the only element, which can not be treated equally for symmetric and asymmetric voltage. Therefore, the absolute value and also location of this element have to differ, depending on the type of measurement. The numeric value of the YSZ resistance was not obtained by a real fitting method, but by taking the impedance value with minimal imaginary part in the high-frequency region. This is more accurate than including it into the fitting routine, because the YSZ offset resistance can be measured independently of the electrode impedance, and a fitting routine with less parameters is more accurate.

- $R_{YSZ}^{sym}$: For symmetric applied voltage, the YSZ resistance is a serial resistor to the entire electrode impedance function and represents the spreading resistance against the counter electrode.
- $R_{YSZ}^{asym}$: For asymmetric applied voltage, the YSZ resistance is only relevant in the high-frequency range, and must not play a role in the low-frequency range, where the electronic current is dominating. It can therefore be placed in series to the double-layer capacitance at the YSZ-Pt interface. This representation is still an approximation, but the YSZ resistance is comparatively small, so that a large error is not expected.

Full stoichiometric polarisation of the electrode only occurs at the edges of the metal grid, where electronic and ionic transport paths are very short. In the electrode area over YSZ, the dominant transport losses are electronic, and ionic transport losses dominate in the area over the Pt grid. The voltage source on the right side of the equivalent circuit refers to the next metal finger, which can be driven with equal polarity (symmetric voltage) or opposite polarity (asymmetric voltage). In order to keep the amount of parameters small, and an analytic expression for the impedance function possible, some simplifications have to be made. The YSZ resistance for asymmetric applied voltage can only be modelled approximatively. Also, the ionic current over the metal grid has to pass the ionic YSZ-STFO interface, for which only an approximative analytic solution can be found. Chemical capacitance and oxygen exchange rate of the electrode part grown on platinum and on YSZ are assumed to be equal (the surface topology for the electrode part above platinum and YSZ appears very similar in SEM images). These simplifications may influence the high-frequency part of the spectra, but in the low-frequency range, they are not assumed to play an important role (in the case that the surface reaction is the rate limiting step). Consequently, $\mathrm{R}_{\mathrm{redox}}$, and $\mathrm{C}_{\mathrm{chem}}$, as well as $\mathrm{R}_{\mathrm{electron}}$ are expected to be determinable with satisfying accuracy (The fitting error is expected to be below the standard deviation for different electrodes), the ionic interface parameters might be

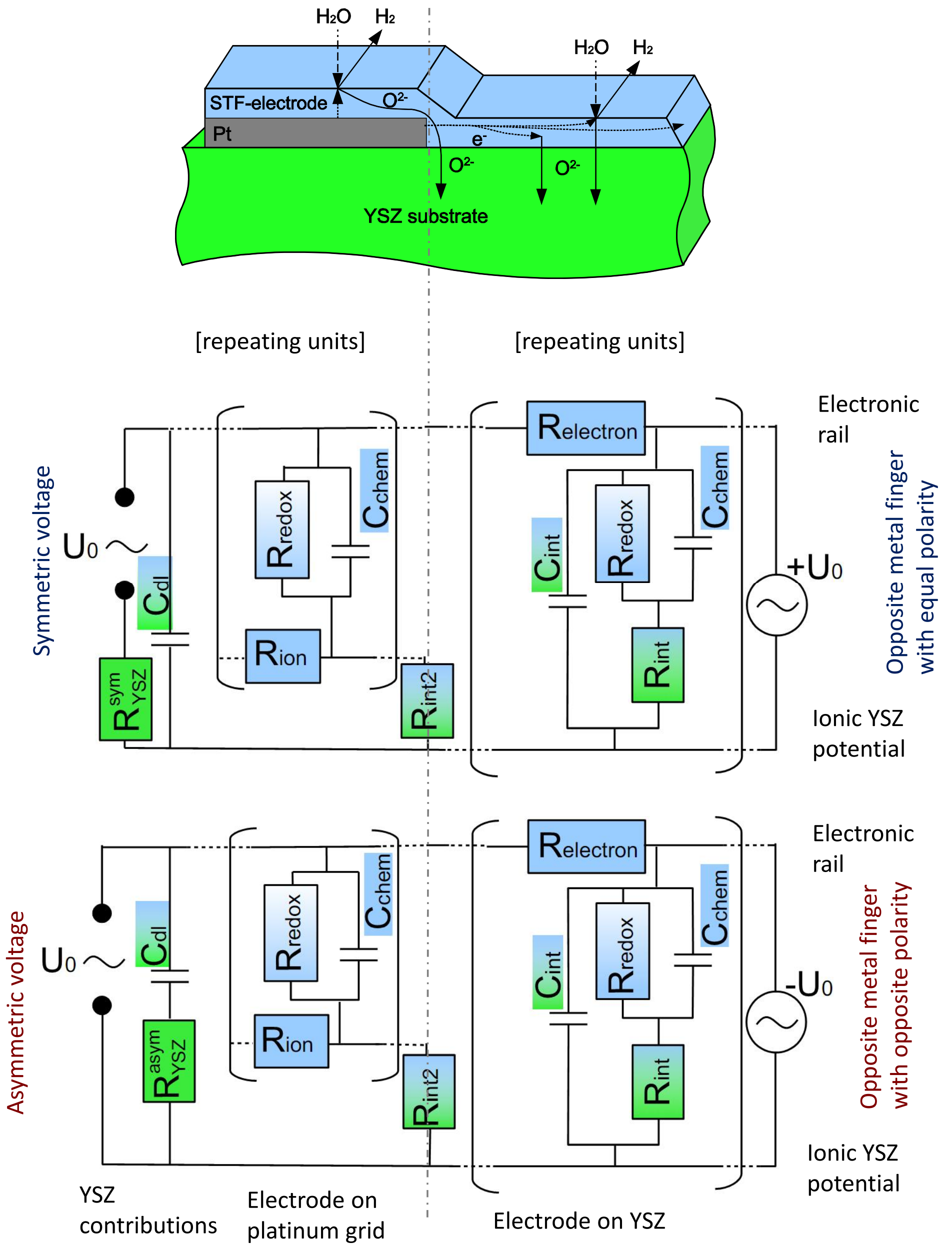

Figure 5.5: Reaction scheme and equivalent circuit for a STFO electrode above the metal grid. The equivalent circuits for symmetric and asymmetric voltage are almost equal, only the representation of the $R_{YSZ}$ element and the boundary conditions on the right hand side change.

prone to higher fitting errors. For STFO-electrodes, the ionic interface capacitance ($C_{int}$) can not be fitted with satisfying accuracy, because the parallel Pt-YSZ double layer capacitance is much larger. In the fitting routine, $C_{int}$ was manually set zero.

### 5.3.6 Full equivalent circuit for metal fingers on top of the electrode

The electrochemical reactions (and the equivalent circuit) for the electrode part without platinum are independent of the placement of the metal fingers (above or beneath the electrode). In the region below the metal grid, however, a new reaction model has to be derived.

**Electrode region below the platinum grid** In this region, lateral electronic transport is fast, and no lateral ionic transport is necessary, so a homogeneous cell polarisation can be assumed. Also, the bulk and ionic interface properties of the electrode are equal to the free surface area, but oxygen exchange at the surface is blocked. Therefore, this electrode region can be modelled with the simplified equivalent circuit by J.Jamnik and J.Maier [21], with blocked surface reaction path.

**YSZ resistance** Also in this case, the YSZ resistance has to be modelled differently for symmetric and asymmetric meaurement.

- $R_{YSZ}^{sym}$ is placed in series to the entire electrode impedance.
- $R_{YSZ}^{asym}$ is placed in series to the reactions below the metal grid.

When the metal grid is placed on top of the electrode, the STFO film is homogeneously grown on YSZ, and less simplifications have to be made to preserve an analytical expression for the impedance. Ionic conductivity, on the other hand can not be measured in this case.

## 5.4 Normalisation and fitting of the measured spectra

The impedance functions derived by the equivalent circuits in fig. 5.5 and 5.6 are normalized to one centimetre of metal finger edge length, and do

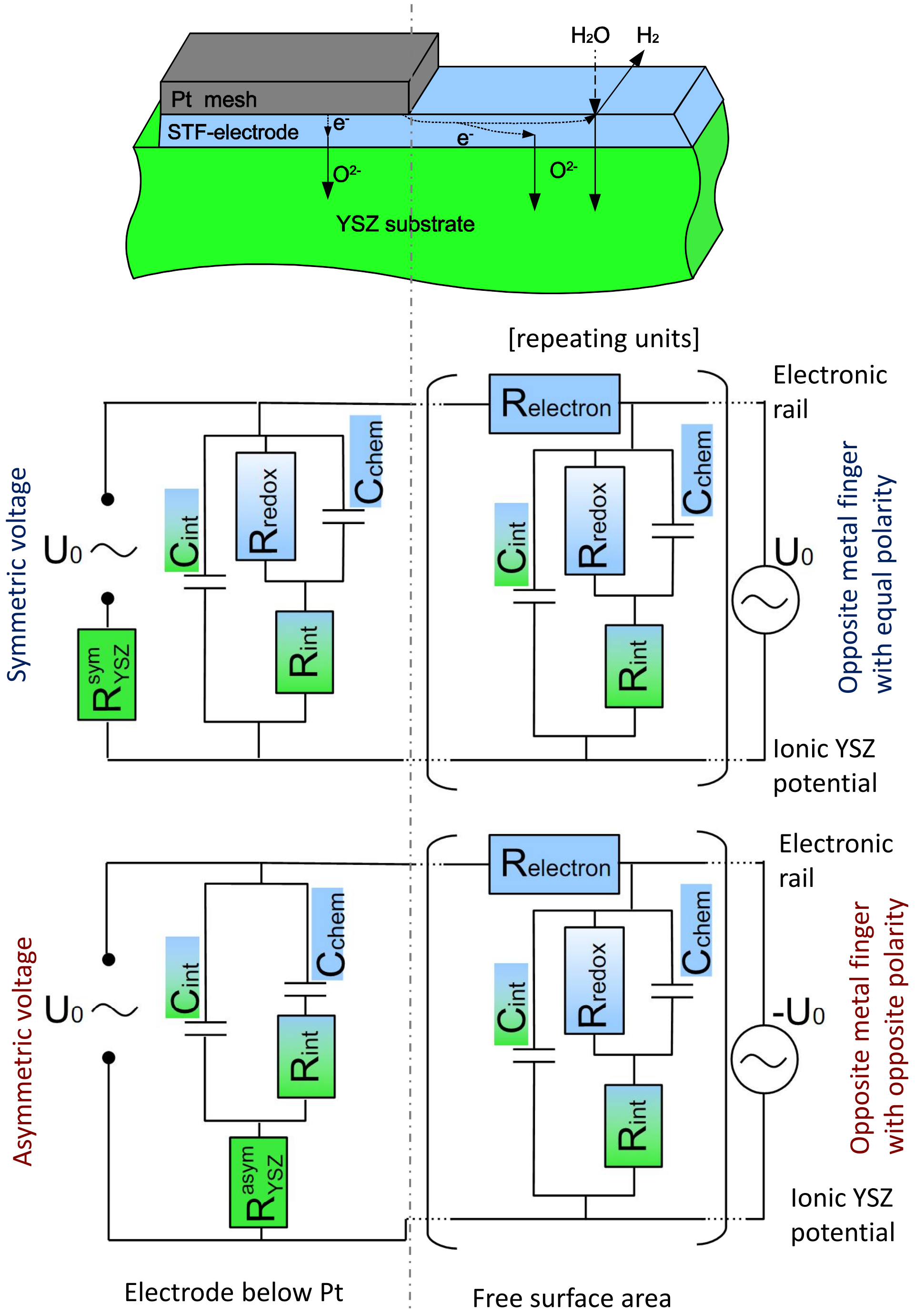

Figure 5.6: Reaction scheme and equivalent circuit for a STFO electrode with metal grid on top. The equivalent circuits for symmetric and asymmetric voltage are almost equal, only the representation of the $R_{YSZ}$ element and the boundary conditions on the right hand side change.

not contain contributions from the electrode borders. With simple linear transformations, the measured impedance spectra can be normalized like the calculated functions. These transformations are necessary before fitting of the measurements to the previously derived functions. This also allows fitting of symmetric and asymmetric measurement in one run / parameter set.

### 5.4.1 Normalisation

**YSZ resistance and temperature calculation** The YSZ resistance is already modelled in the equivalent circuits for the electrodes. For the plot in the manual fitting routine (in section 5.4.2), the YSZ resistance is simply subtracted from the measurements, which reveals perfectly overlapping spectra in the high-frequency region (fig. 5.9), as expected from theoretical calculations (fig. 5.3). Since the spreading resistance formula 3.1 is only valid for circular microelectrodes, it is not directly applicable for rectangular electrodes. This problem can easily be solved when additional circular electrodes are placed on the same substrate as the rectangular electrodes. In this case, the ratio in the spreading resistance for circular and rectangular electrodes can be measured, which leads to a virtual electrode diameter. Circular electrodes with a diameter of 150 µm were used for comparison for the three different metal grid sizes.

| metal finger distance | $R_{YSZ}$ ratio | virtual electrode diameter |
|---|---|---|
| 5 µm | 2.1 ± 0.1 | 310±15 µm |
| 11.6 µm | 2 ± 0.1 | 300±15 µm |
| 25 µm | 1.8 ± 0.1 | 270±15 µm |

Table 5.1: Virtual diameter of microfinger-electrodes, estimated by comparison of the $R_{YSZ}$ values to 150 µm circular electrodes.

**Electrode borders** Since the electrode is not infinite, also the electrode borders have to be taken into account. The electrodes overlap the metal grid by l, with a finger distance of 2l (see fig. 5.8). At the electrode borders, the lateral electronic current has to be zero, which means that $\partial U(x)/\partial x =$

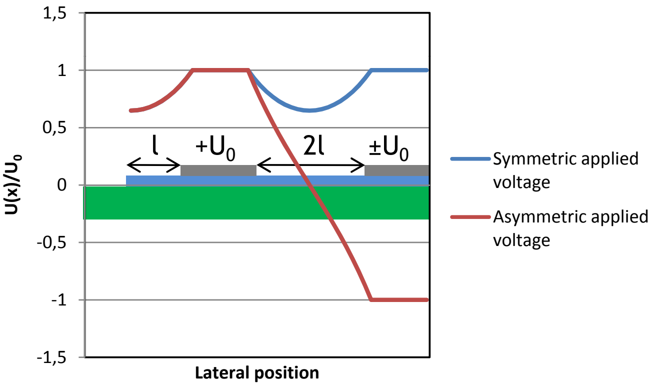

Figure 5.7: Calculated distribution of the overpotential at the electrode borders and inner part for symmetric and asymmetric applied voltage. Calculations contribute to the DC case with $\sqrt{\gamma l} = 1$.

$-R_s I(x) = 0 \quad at \quad x = l$. This boundary condition causes the same current and voltage distribution function as for symmetric applied voltage, as depicted in fig. 5.7. Therefore, the electrode borders do not influence the impedance measurement for symmetric applied voltage. When asymmetric voltage is applied, the electrode borders deliver contributions from the symmetric measurement. These contributions can easily be subtracted, because the electrode border length is well known.

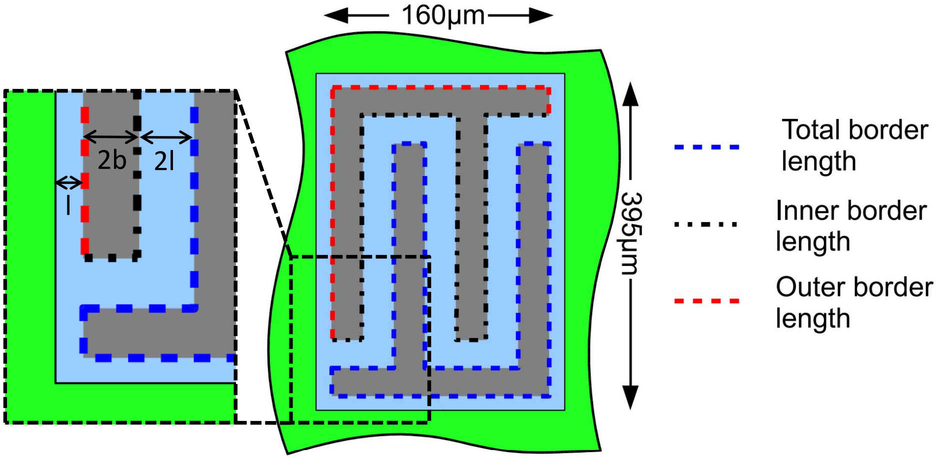

Figure 5.8: Measures of the platinum grid on the electrodes.

**Normalization to platinum finger border length** Finally, the measured impedance values have to be normalised to the length of the platinum finger borders. The dimensions of the electrodes are $395 \times 160\,\mu\text{m}^2$, with three different metal comb designs. The measures are summarized in table 5.2. In the calculations for the asymmetric driving voltage, the voltage of the metal fingers is $\pm U_0$. In an impedance measurement, only the difference in the potential is $U_0$. Therefore the fingers are polarised with $\pm 0.5U_0$, with the YSZ substrate at zero potential. This causes only half the current, compared to the theoretical calculations, and therefore double measured impedance, so the impedance value has to be divided by two. In fig. 5.9, the impedance spectra as measured (a) and after normalisation (b) are shown. The shape of the spectra remains, and in the high frequency region, they are perfectly overlapping, which is in agreement with theoretical calculations (fig. 5.3). Also, the unit changes from $\Omega$ to $\Omega\, cm$, since the measurements become normalised to 1 cm of metal grid border length. For the plot, the YSZ spreading resistance was subtracted to visualise the overlapping electrode impedance in the high frequency region.

| number of fingers | finger width (2b)[$\mu$m] | finger distance (2l)[$\mu$m] | total border length [$\mu$m] | inner border length [$\mu$m] | outer border length [$\mu$m] |
|---|---|---|---|---|---|
| 4 | 15 | 25 | 3060 | 1065 | 465 |
| 6 | 15 | 11.66 | 4693 | 1841 | 505 |
| 8 | 15 | 5 | 6300 | 2625 | 525 |

Table 5.2: Exact electrode measures for different metal comb designs.

### 5.4.2 Fitting

**manual *"fitting"*** The previously derived impedance functions are fairly unconventional for fitting, since two complex measurements with two different functions are fitted to one parameter set. A manual fitting routine was implemented, before automatised algorithms with satisfying results using *Wolfram Mathematica* could be developed. With the process of manual fitting, the derived values may slightly be shifted in the direction desired by

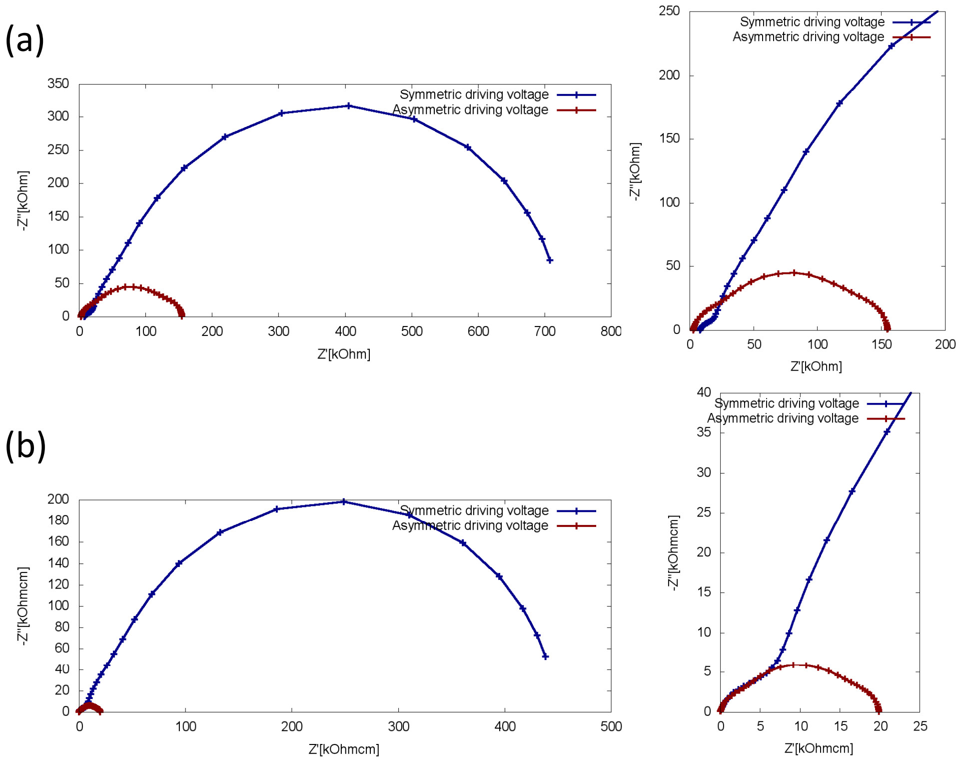

Figure 5.9: Measured spectra at 540℃, 5$\mu$m finger distance (a) before and (b) after the normalisation.

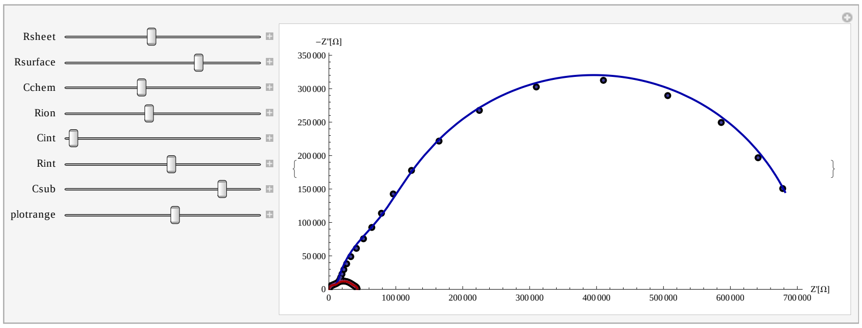

Figure 5.10: Screenshot of the manual *"fitting"* method showing fit parameter manipulators (left) and nyquist plot (right). Numerical values of the fitting parameters are shown after a satisfying approximation was found.

the experimentalist, and the effort is much greater. To reduce this influencing factor, a ”blind” fitting method was used, where the numerical values of the parameters are only shown after a satisfyingly good approximation was found (see fig. 5.10). Also some advantages can be found with the manual fitting routine. When the approximations regarding the equivalent circuit are known, it is more clear, in which frequency range deviations from the experimental data are expected. Also, a manual fitting routine is a very instructive and funny way to get a feeling on the influence of parameter changes on the impedance spectra.

**Automatised numeric fitting** Also an automatic fitting routine could be developped, which is not a direct fit, but a routine, that minimises the sum of squared relative errors between measurement and fitting function (which is a single real valued function). This method the same goal as in a least squares fit, but with a different algorithm is used, which is numerically more stable. In this case, only one real-valued function has to be minimised. Starting parameters for the fit are automatically calculated from the spectra, which is greatly reducing the effort of fitting, and eliminates the influence of the operator on the fit. However, when compared to manual *”fitting”*, the difference of the gained parameters (except for the interface parameters) is below ±10%.

## 5.5 Verification of the reaction model over geometry variations

The photolithographic masks contain three different metal grid shapes with metal finger distances from 5 to 25 µm, which are placed on the same YSZ substrate. The values in the previously derived equivalent circuits are, apart from well known geometry factors, material parameters, and should stay equal, when the metal finger distance is varied. To prove this assumption, different metal finger geometries on a sample with metal fingers beneath the electrodes and 40 minutes deposition time (∼200 nm thickness) was measured at 450 ℃. In fig. 5.11, the measured spectra and corresponding fit is shown for the three different metal finger distances. The proposed equivalent circuit (fig. 5.5) is suited for fitting the entire electrode impedance

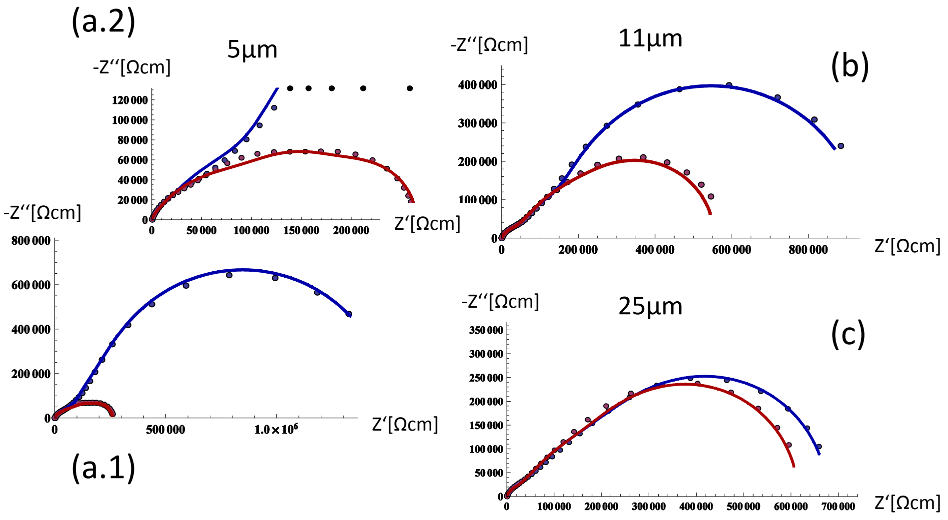

Figure 5.11: Measured (dots) and fitted (lines) impedance spectra at 450 °C with different metal finger distances: 5 µm (a.1 - full, a.2 - magnification) 11 µm (b), 25 µm (c) for symmetric (blue) and asymmetric (red) driving voltage. Metal fingers were beneath the electrode, STFO deposition time: 40 minutes($\sim 200\,nm$).

| finger distance $[\mu m]$ | $\mathrm{R_{redox}}$ $[\Omega\mathrm{cm}^2]$ | $\rho_{\mathrm{electron}}$ $[\Omega\mathrm{cm}]$ | $\rho_{\mathrm{ion}}$ $[\Omega\mathrm{cm}]$ | $\mathrm{C_{chem}}$ $[\mathrm{mFcm^{-2}}]$ | $\gamma(\omega = 0)l$ |
|---|---|---|---|---|---|
| 5 | 1273 | 27400 | 33600 | 6.68 | 0,26 |
| 11.6 | 1023 | 37600 | 26600 | 7.74 | 0.79 |
| 25 | 1071 | 37700 | 26600 | 7.52 | 1.65 |

Table 5.3: Electrode parameters for different mesh sizes, measured at 450℃ with metal fingers beneath the electrode.

(without YSZ contributions) in the frequency range starting at 10-100 kHz, to several mHz for different metal finger distances with satisfying accuracy. At the given temperature, an interesting phenomenon can be clearly observed: For 5 µm finger distance, the (DC case) electronic diffusion length is larger than the finger distance, resulting in a large difference between the symmetric and the asymmetric measurement. With increasing finger distance, the limiting process switches from the surface reaction to lateral electronic (and ionic) transport, where the impedance becomes almost independent, whether symmetric or asymmetric voltage is applied. This transition was already explained in the simulated spectra in fig. 5.3. In the case of the 11 and 25 µm mesh, the derived values have a larger fitting-error, because both spectra become rather similar. In general, when the electronic diffusion length becomes smaller than the metal finger distance, the accuracy of the fit will drop. So, the measurement with 5 µm finger distance contains the most accurate information, and the other measurements are mainly included as a prove of the theory. Also, all spectra are indistinguishable in the high frequency region, which is attributed to the reduction of the electronic and ionic diffusion length, and a concentration of the current paths near the metal finger edges. Since the activation energies for electronic and ionic transport processes are higher than for the oxygen exchange reaction, the transition to electronic transport limitation can not be observed at significantly higher temperature for the given electrode geometries.

## 5.6 Temperature dependence and activation energies

With the new electrode design, a calculation of electronic and ionic resistance is easily possible, and the oxygen exchange resistance is automatically normalised to the electrochemically active fraction of the surface.

| Electrode property | oxygen exchange | electronic $\rho$ | ionic $\rho$ |
|---|---|---|---|
| Value | 0.62 eV | 1.01 eV | 1.15 eV |

Table 5.4: Activation energies of electrode properties with metal grid beneath the electrode.

In fig. 5.12, the temperature dependence of electronic and ionic resistivity as well as ASR for the surface reaction are shown, and the corresponding

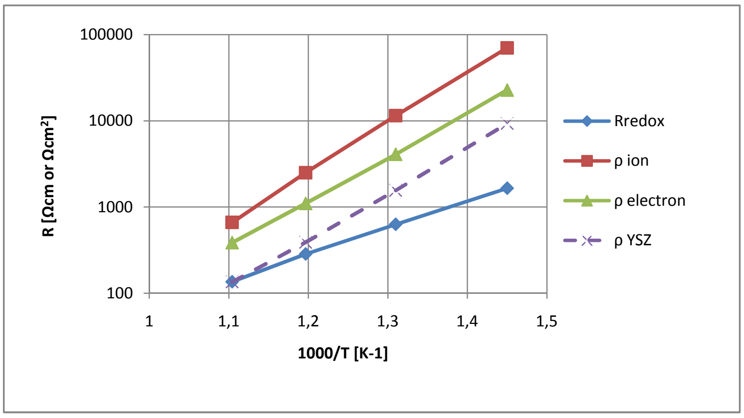

Figure 5.12: Arrhenius plot and activation energies for oxygen exchange, ionic and electronic resistivity, measured with a thin film metal grid beneath the electrode, deposition time: 40min (~200 nm). $\rho_{YSZ}$ was calculated with the spreading resistance formula. (3.1).

activation energies are summarised in table 5.4. Controversial to previous measurements (fig. 4.18, fig. 4.11), no deviations from perfectly straight lines can be observed in the Arrhenius plot, which is probably due to the quantitative reaction model, which compensates eventual changes of the active area at different temperature. It has to be stated, that the measured ionic conductivity is the lateral conductivity of STFO grown on platinum, instead of YSZ. In this region, the electrodes do not appear epitaxial, and grain boundaries probably exist. The electrical conductivity, on the other hand, is measured for STFO grown on YSZ, which looks epitactic in XRD and SEM measurements.

**Ionic resistivity** For the ionic resistivity, not only the bulk resistivity, but also the grain boundaries are measured, which can not be separated with this setup. Grain boundaries might even be the main cause of ionic resistance. Nevertheless, the measured ionic conductivity of STFO is relatively high. Compared to single crystalline YSZ, the resistivity is approximately 5 times higher. Also, the activation energy of the ion hopping process is close to the YSZ (1,06 eV for YSZ, and 1,15 eV for STFO in the given temperature range).

### 5.6.1 Temperature dependence of the electronic resistivity

Several processes contribute to the temperature dependence of the electronic resistance: electronic excitation into the conduction band, changing oxygen non-stoichiometry with temperature, resulting in a shift of the Fermi level, and the temperature dependence of conduction electrons. Therefore, the activation energy for the electronic resistance can not be mapped to an elementary process.

**Electronic conductivity and Fermi level** The density of conduction electrons can be calculated by measurement of the specific conductivity of STFO and the mobility of electrons. In the literature [20], the temperature dependence of the electron mobility is proposed to be $\mu^*_{el} = 1,97{*}10^8\,T^{-2.7\pm0.2}$.

$$\mu^*_{el} = 1,97 * 10^8\,T^{-2.7\pm0.2} \tag{5.43}$$

$$[e^{'}] = \frac{\sigma_{el}}{e}\frac{T^{2.7\pm0.2}}{1,97 * 10^8} \tag{5.44}$$

The number of conduction electrons can also be calculated from the energy difference between Fermi level and conduction band ($E_{cb} - E_f$). $N_{eff,cb}$ is the effective density of states in the conduction band (equation A.1). [17].

$$N_{eff,cb} = 2\left(\frac{2\pi m^*_e k_b T}{h^2}\right)^{\frac{3}{2}} \tag{5.45}$$

The effective mass of the electron is assumed to be equal to a free electron ($m^*_e = m_e$)

$$[e^{'}] = N_{eff,cb}\,e^{-\frac{E_{cb}-E_f}{k_b T}} \tag{5.46}$$

$$E_{cb} - E_f = \ln(\frac{[e^{'}]}{N_{eff,cb}})\,k_b T \tag{5.47}$$

$E_{cb} - E_f$ can consequently be calculated by equation 5.44 and 5.47. When these equations are applied to the measured values of electronic conductivity and the reported values of the mobility of electrons [20], the energy difference $E_{cb} - E_f$ is temperature-dependent, with a value of 0.84 eV at 412℃ and 0.76 eV at 633 ℃. The calculated shift in the Fermi level is (qualitatively) consistent with the previously made observation on the temperature dependence of chemical capacitance isotherms depicted in fig. 4.21, section 4.4.5.

In this section, it could be observed that an increase in temperature leads to more reducing conditions, which also means a rise of the Fermi level. These interpretations are, however, based on the assumption that the reported electron mobility values are correct, and that the conduction takes place in a band-like model.

When equation 5.44 is applied to the measured data, an activation energy of 1.2 eV for $[e^{'}]$ is obtained. This value clearly differs from the (calculated) difference between $E_f$ and $E_{cb}$, which is a further indication for a temperature-dependent Fermi level.

## 5.7 Mechanistic interpretation of the surface reaction

So far, electronic and ionic transport processes as well as chemical capacitance and ASR of the surface reaction could be well separated and hence quantified by electrochemical impedance spectroscopy. At sufficiently high temperature and small metal finger distance, the surface reaction can be identified as the rate limiting step. A mechanistic interpretation of the reaction and identification of the rate limiting step has not been carried out so far. In oxygen atmosphere, the exact mechanism could not be identified, but there is a strong indication, that the rate limiting step for oxygen incorporation is involving an electron transfer from the conduction band to an adsorbed oxygen species [11, 10]. In reducing atmosphere, many defect concentrations change. In equilibrium, the chemical potentials of products and educts have to be equal in the oxygen surface exchange reaction.

$$\begin{aligned} \frac{1}{2}O_2 &\rightleftharpoons O^{2-} - 2e^- \\ \frac{1}{2}\mu_{O_2} &= \mu_{O^{2-}} - 2\mu_{e^-} \end{aligned} \tag{5.48}$$

The change in the chemical potential of oxygen between $H_2$-$H_2O$ vapour and oxygen atmosphere is equal to the Gibbs free energy change of the water generation reaction ($\Delta_R G$). Also, in section 4.4.5, it could be estimated, that the chemical capacitance is limited by the electronic density of states, which is helpful in the calculation of the chemical potential changes.

$$\begin{aligned}
\frac{1}{2}\Delta\mu_{O_2} &= \Delta_R G = \Delta\mu_{O^{2-}} - 2\Delta\mu_{e^-} \\
\frac{\partial\mu_{O^{2-}}}{\partial c} &\ll \frac{\partial\mu_{e^-}}{\partial c} \\
\Delta\mu_{e^-} &\approx -\frac{1}{2}\Delta_R G \qquad (5.49)
\end{aligned}$$

Since the chemical potential of electrons is basically a synonym for the Fermi level, the change in the conduction electron concentration can easily be calculated, according to [17]. The exact value of $\Delta_R G$ for different temperatures was already calculated in section 2.1. At a temperature of 550 ℃, $\Delta_R G$ for the water generation reaction is around -200 kJ/mol.

$$\Delta E_f = \Delta\mu_{e^-} \approx -\frac{1}{2}\Delta_R G \qquad (5.50)$$

$$\Delta E_f \approx 1.04\, eV (T = 550\,{}^{\circ}C) \qquad (5.51)$$

$$[e^{'}] = N_{eff,cb} e^{\frac{E_f E_{cb}}{k_b T}} \qquad (5.52)$$

$$\frac{[e']_{H_2/H_2O}}{[e']_{O_2}} = e^{\frac{\Delta E_f}{k_b T}} \approx 2.3 \times 10^6 (T = 550\,{}^{\circ}C) \qquad (5.53)$$

In $H_2$-$H_2O$ atmosphere, the number of conduction electrons is approximately six orders of magnitude larger than for oxygen. If the rate limiting step in hydrogen atmosphere would still be an electron transfer from the conduction band, much faster kinetics, and an activation energy lowered by roughly 1 eV, and consequently a strongly reduced ASR would be expected. In [11], an ASR activation energy of 2 eV for 35 % Fe-dopted STFO was reported for oxygen atmosphere. It was also reported that below 1 mbar $p_{O_2}$, the activation energy drops down to approximately 1 eV , and the pressure dependence shifts from ASR$\propto {p_{O_2}}^{-0.25}$ to ASR$\propto {p_{O_2}}^{-1}$. This indicates, that even in oxygen atmosphere, the rate limiting step changes from an electron transfer in the high $p_{O_2}$ range to another process (maybe adsorption) in the low $p_{O_2}$ range.

In $H_2$-$H_2O$ atmosphere, the calculated difference $E_{cb} - E_f$ of about 0.8 eV is in good agreement with the literature value in [11]: $E_{cb} - E_f \approx 1.9\, eV$ is reported in oxygen atmosphere. In hydrogen atmosphere, the Fermi level shifts by about 1 eV (eqn. 5.52), revealing a theoretically calculated value of $E_{cb} - E_f \approx 0.9\, eV$.

The activation energy for the water splitting reaction, with values from 0.6-0.8 eV, is definitely lower than the calculated activation energy for $[e^{'}]$ with 1.2eV.

Contrary to the activation energy, the magnitude of the ASR for undegraded electrodes in $H_2 - H_2O$ atmosphere is similar to the values reported in [11], where an ASR of $10\,\Omega\text{cm}^2$ at 650°C in roughly 20 mbar $O_2$ was measured by EIS.

### 5.7.1 Conclusions on the rate limiting step

Since the concentration of conduction electrons is approximately six orders of magnitude larger than in oxygen atmosphere, an electron transfer from the conduction band to an adsorbed species is expected to be fast. If this were the rate limiting step, the surface reaction rate should increase dramatically. Also, the activation energy of the ASR is 0.4-0.6 eV smaller than of $[e^{'}]$ concentration. Given the very low activation energy, it is rather surprising, that the ASR is very similar in oxygen as well as in $H_2$-$H_2O$ atmosphere. Maybe the overall surface coverage of the species involved in the RDS is very small under equilibrium conditions. For a detailed mechanistic investigation of the surface reaction, more investigations on the exact surface topology, orientation and termination (SrO or $TiO_2$), the mechanism of water adsorption (molecular or dissociative) as well as the relevant processes of degradation would be helpful. With EIS measurements, only the magnitude of the ASR can be measured, the reaction mechanism remains on black box level. Attributed to the necessity of a high surrounding gas pressure and temperature during fuel/electrolysis cell operation, to the author's best knowledge, surface adsorbates can not be detected by in situ measurements. Only indirect observations such as the influence of gas atmosphere and defect concentrations on the ASR may lead to a conclusive interpretation of the surface reaction. A thorough mechanistic investigation and discussion would be beyond the scope of this work. However, the new electrode and metal grid design allows quantification of electronic and ionic conductivity as well as ASR and chemical capacitance on one single microelectrode, which reduces the experimental effort involved in the investigation of mixed conducting thin films. Also, the systematic error caused by usage of different samples for determination of different thin film properties can be eliminated.

# 6 Summary of scientific results

The magnitude and type of electronic conductivity of STFO is strongly depending on the surrounding gas atmosphere. It changes from moderate p-type conductivity in oxygen atmosphere to low n-type conductivity in hydrogen gas atmosphere. An investigation of the electrochemical properties of STFO microelectrodes in $H_2 - H_2O$ atmosphere requires application of a thin film platinum grid as a current collector.

The chemical capacitance can be used to estimate the concentration of the majority electronic defect [21]. In hydrogen atmosphere, this value does not directly correlate with the electronic conductivity, which implies that most electronic defects must be localised and therefore not contribute to the electronic conductivity.

The low electronic conductivity in $H_2 - H_2O$ atmosphere is causing noticeable artefacts in the impedance spectra, even when a metal grid is applied to the electrodes. A novel design of the metal grid for the microelectrodes was developed and employed, where two different impedance spectra can be measured for one electrode. This also means, that two impedance spectra can be used for one fitting run / parameter set, which increases the fitting accuracy and allows separation of electronic and ionic transport processes. Analytical equivalent circuits could be derived from the basic transport and reaction laws of mixed conducting thin films with metal grid on top or below the electrode. With usage of these equivalent circuits, electronic and ionic transport losses can be separated from the surface reaction, and the surface reaction can be identified as the rate limiting step at temperatures above 500 °CWhen a current collector is applied to the electrode. The simultaneous quantification of electronic and ionic conductivity further allows investigation of correlations between transport properties, chemical capacitance and ASR.

# A Appendix

## A.1 List of symbols and acronyms

- **SOFC**: Solid Oxide Fuel Cell
- **SOEC**: Solid Oxide Electrolysis Cell
- **STFO**: Iron doped strontium titanate $\mathrm{SrTi_{1\text{-}x}Fe_xO_{3\text{-}\delta}}$
- **RDS**: Rate determining step - the elementar process which is limiting the reaction rate of a multi-step reaction
- **TPB**: Triple phase boundary - The (quasi 1-dimensional) region where electrode, electrolyte and gas meet
- $z_e$: number of elementary charges
- $e$: Eulers number, or elementary charge
- $F$: Faraday constant $F = 96485.33 Cmol^{-1}$ [12]
- $\mu_x$: chemical potential of species x
- $\mu_x^*$: mobility of charge carrier x
- $\varphi$: Electrostatic potential
- $\tilde{\mu}_x$: electro-chemical potential of species x $\tilde{\mu}_x = \mu_x + F z_e \varphi$
- $m_e^*$ : Effective mass of the electron in the conduction band
- $h$: Planck constant
- $k_b$: Boltzmann constant, $1.38065 * 10^{-23} \frac{J}{K}$ [12]
- $R$: Gas constant, $8.314 \frac{J}{mol\,K}$ [12]
- $\mathrm{E_f}$: Fermi level
- $\mathrm{N_{eff,cb}}$: effective density of states in the conduction band [17]

$$N_{eff,cb} = 2\left(\frac{2\pi m_e^* k_b T}{h^2}\right)^{\frac{3}{2}} \tag{A.1}$$

- $\mathrm{E_{cb}}$: Lowest energy level in the conduction band
- $T$: Temperature
- $S$: Entropy

- $H$: Enthalpy
- $G$: Gibbs free energy $G = H - TS$
- $\Delta_R P$: Change in thermodynamic potential P caused by an isothermal, isobaric reaction
- $e^-$: An electron, no energy level specified
- $e^{'}$: An electron in the conduction band
- $[x]$: Volumetric concentration of species x
- $\nu_x$: Stoichiometric coefficient of species x in a chemical reaction
- **R-C**: Series circuit of resistor and capacitor
- **R||C**: Parallel circuit of resistor and capacitor

# List of Figures

# List of Tables

## A.2 Source codes used for fitting and evaluation of the measurements

### A.2.1 Automatised fitting routine for microfinger-electrodes

The source code of the *"Wolfram Mathematica"* routine, which was used for automatic fitting is shown. The impedance function in this case is modelling a microelectrode with metal mesh on top.

```
 (*Define filename and MeshType*)
FileSym = "5UM_S_10.TXT";
FileASym = "5UM_A_10.TXT";
MeshType = 1;
Overetch = 0;
HeaderLines = 4;
maxf = 50;
PrependTo[$Path, "D:\Eigene_Dateien\PA_BSZ\Messdaten" ];

Measures = {{0.626, 0.135, 0.0540, 0.00025, 0.00075}, {0.468, 0.0914, 0.0520,
    0.0005833, 0.00075}, {0.3, 0.0525, 0.048, 0.00125, 0.00075}};
RYSZfractions = {16, 12, 5};
(*read file as table, drop HeaderLines lines*)
Data = Drop[Import[FileSym, "Table"], HeaderLines];
(* fsym is the list of omega values, not frequencies*)
fsym = Data[[All, 1]]*2*Pi // N;
 (* Column 2 an 3 of the input file contain the information*)
impedancesym = Table[Complex[Data[[i, 2]], Data[[i, 3]]], {i, 1, Dimensions[
    Data][[1]]}];
(* Point of minimal imaginary impedance in HF region is YSZ offset *)
RYSZ = impedancesym[[Ordering[Take[Abs[Im[impedancesym]], {1, 20}], 1]
    [[1]] ]] // Re;
impedancesym = impedancesym*Measures[[MeshType, 1]]; (*Normalisation to
    border length*)
nsym = Dimensions[fsym][[1]];
RYSZsym = RYSZ*Measures[[MeshType, 1]];
```

```
Data = Drop[Import[FileASym, ”Table”], HeaderLines];
fasym = Data[[All, 1]]*2*Pi // N;
nasym = Dimensions[fasym][[1]];
impedanceasym = Table[Complex[Data[[i, 2]], Data[[i, 3]]], {i, 1, Dimensions[
      Data][[1]]}];
RYSZasym = impedanceasym[[Ordering[Take[Im[impedanceasym], {1, 20}],
      -1] [[1]] ]] // Re;
impedanceasym = impedanceasym - RYSZasym;
(*Substraction of the electrode border contributions from the asymmetric
      measurement*)
impedanceasym = 1/(1/(impedanceasym) - 1/(impedancesym[[1 ;; nasym]] -
      RYSZ*Measures[[MeshType, 1]]) * Measures[[MeshType, 3]]/2) + RYSZasym
      ;
RYSZasym2 = impedanceasym[[Ordering[Take[Im[impedanceasym], {1, 20}],
      -1] [[1]] ]] // Re;
impedanceasym = impedanceasym*Measures[[MeshType, 2]];
fmin = Log[fsym[[-1]]]; fmax = Log[fsym[[1]]];
(*generalised transmission line impedace*)
TLsym[Y_, R_, l_] = (R/Sqrt[R*Y])*Coth[Sqrt[R*Y]*l];
TLasym[Y_, R_, l_] = (R/Sqrt[R*Y])*Tanh[Sqrt[R*Y]*l];
 lfree  = Measures[[MeshType, 4]] + Overetch/10000; (*metal finger distance/2*)
lmetal = Measures[[MeshType, 5]] - Overetch/10000; (*metal finger width/2*)
(*Position of the first occurence of f < maxf*)
fdrop1  = Position[fsym, Select[fsym, # < maxf*2*Pi &, 1][[1]] ]  [[1,  1]];

 Relectron1 = impedanceasym[[-1]]/lfree//Abs;
R0Sym1 = RYSZ*Measures[[MeshType,1]]*2;
(*low-frequency semicircle R1-(R2//C1) fit to get starting values for the
       fitting  function*)
 fdroplf  = Ordering[Im[impedancesym],1][[1]]-1;
Startparameters = FindMinimum[Sum[Abs[(Roffset + 1/(Cchem*(lfree+
      lmetal)*I*fsym[[i]]+Ychem*(lfree)) - impedancesym[[i]])^2/impedancesym[[i
      ]]^2],{i,fdroplf,nsym}],{{Roffset,RYSZ*3},{Cchem,0.005},{Ychem,1/(Re[
      impedancesym[[nsym]]]*(lfree))}},Method->”PrincipalAxis”][[2]];
Ychem1 = Ychem/.Startparameters;
Cchem1 = Cchem/.Startparameters;

(*Modelling of the impedance function*)
Yfree0 =1/(1/(Ychem0 + I*Cchem0*w)+Roffset);
Rmetal0= (1/(I*Cchem0*w)+Roffset ) /lmetal;
Zsym0 = 1/(1/TLsym[Yfree0,Relectron0,lfree] +1/Rmetal0)+RYSZsym;
Zasym0 = 1/(1/TLasym[Yfree0,Relectron0,lfree] +1/(Rmetal0+RYSZsym/
      RYSZfractions[[MeshType]]));
StartParameters = {Cchem0 -> Cchem1, Relectron0 -> Relectron1, Ychem0
      -> Ychem1,R0Sym0 -> R0Sym1};
StartList  = {{Cchem0 , Cchem1}, {Relectron0 ,Relectron1},{ Ychem0 ,Ychem1
      }, {Roffset,RYSZasym2*lmetal}};
StartList//N
```

```
(∗Minimise the sum of squared errors∗)
Parameters = FindMinimum[Sum[Abs[((Zsym0/.{w−>fsym[[i]]})−
      impedancesym[[i]])ˆ2/(impedancesym[[i]])ˆ2],{i,fdrop1,nsym}]/nsym +
     Sum[Abs[((Zasym0/.{w−>fasym[[i]]})−impedanceasym[[i]])ˆ2/(
           impedanceasym[[i]])ˆ2],{i,fdrop1,nasym}]/nasym,StartList,Method−>”
           PrincipalAxis”,MaxIterations−>10000,PrecisionGoal−>9];
parameterlist  = Parameters[[2]]
Sqrt[Parameters[[1]]]
parameterlist2  = Append[parameterlist,w−> Exp[w]];

(∗Plot data + fit  with variable  plot  range∗)
Manipulate[
 {Show[{
       ParametricPlot[{{Re[Zsym0/.parameterlist2],−Im[Zsym0/.parameterlist2
             ]},{Re[Zasym0/.parameterlist2],−Im[Zasym0/.parameterlist2]}},{w,
             Log[fsym[[fdrop1]]],Log[fsym[[nsym]]]},PlotRange−>{{0,10ˆprange
             },{0,(10ˆprange)/2}}, AxesLabel−>{”Z’[Wcm]”,”−Z’’[Wcm]”} ,
             PlotStyle −>{{Black},{Black}},Mesh−>{Log[fsym[[fdrop1;;nsym
             ]]],Axes−>False},MeshStyle−>Directive[PointSize[Large],Black],
             ImageSize−>Large] ,
     ListPlot[{Transpose[{Re[impedancesym],−Im[impedancesym]}],
           Transpose[{Re[impedanceasym],−Im[impedanceasym]}]},
           AspectRatio−>0.5 , Mesh−>Full, PlotMarkers−>{””,12},PlotStyle
           −>{Darker[Blue],Darker[Red]},AxesLabel−>{”Z’[Wcm]”,”−Z’’[Wcm]
           ”},PlotRange−>{{0,10ˆprange},{0,(10ˆprange)/2}},ImageSize−>
           Large]
     }],
   Show[{Plot[{Log[−Im[Zsym0/.parameterlist2]],Log[−Im[Zasym0/.
        parameterlist2]]},{w,Log[fsym[[fdrop1]]],Log[fsym[[nsym]]]},PlotRange
        −>All,ImageSize−>Medium,AxesLabel−>{”Ln(w)”,”Ln(−Im(Z))”}],
        ListPlot[{Transpose[{Log[Take[fsym,{fdrop1,nsym}]],Log[−Im[Take[
        impedancesym,{fdrop1,nsym}]]]}],Transpose[{Log[Take[fasym,{fdrop1,
        nasym}]],Log[−Im[Take[impedanceasym,{fdrop1,nasym}]]]}]},
        PlotRange−>All,Joined−>True,Mesh−>Full] }]
   },{{prange,5},3,7}]

 (∗Print  fitting  results  in  an  ascii  file ∗)
values   =Join[(StartList/.parameterlist)  [[ All ,1]],{ RYSZ,Sqrt[Parameters
      [[1]]]}]
out = OpenAppend[StringJoin[ToString[NotebookDirectory[]] , ”
      Arrhenius.txt”]]
WriteString[out,”500␣C␣set␣\n␣Cchem␣\t␣Relectron␣\t␣Ychem0␣\t␣Rinterface␣
      \t␣RYSZ␣\t␣Sum␣of␣relative␣errors␣\n”];
Do[WriteString[out,InputForm[Log10[values[[i]]]],”\t”],{i,Length[values]}];
WriteString[out,”\n”];
Close[out]
```

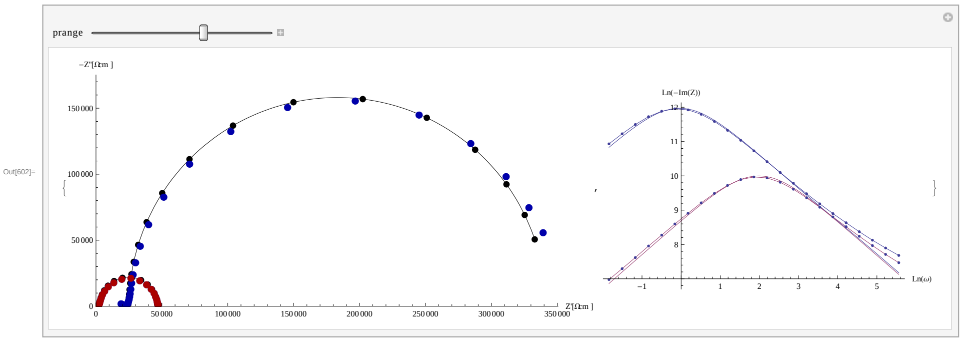

### A.2.2 Manual parameter variation routine

The source code of the *"Wolfram Mathematica"* routine for manual *"fitting"* is shown, the impedance function and start parameters list can be modelled independently of this routine.

```
 pl = StartParameters;
Manipulate[{
  parameterlist2 = {Cchem0−>Cchem,Relectron0−>Relectron,Rredox0−>
      Rredox,Rion0−>Rion,Roffset−>Rint,Cint0−>Csub,w−>w};
  (*Plot  fitting  function and measured points in nyquist plot*)
  Show[{
     ParametricPlot[{{Re[Zsym0/.parameterlist2],−Im[Zsym0/.parameterlist2
        ]},{Re[Zasym0/.parameterlist2],−Im[Zasym0/.parameterlist2]}},{w,
        Log[fsym[[fdrop1]]],Log[fsym[[nsym]]]},PlotRange−>{{0,10^Plotrange
        },{0,(10^Plotrange)/2}}, PlotStyle −>{{Black},{Black}},Mesh−>{
        Log[fsym[[fdrop1;;nsym]] ],Axes−>False},MeshStyle−>Directive[
        PointSize[Large],Black],ImageSize−>Large] ,
    ListPlot[{Transpose[{Re[impedancesym],−Im[impedancesym]}],
        Transpose[{Re[impedanceasym],−Im[impedanceasym]}]},
        AspectRatio−>0.5 , Mesh−>Full, PlotMarkers−>{””,12},PlotStyle
        −>{Darker[Blue],Darker[Red]},AxesLabel−>{”Z’[Wcm]”,”−Z’’[Wcm]
        ”},PlotRange−>{{0,10^Plotrange},{0,(10^Plotrange)/2}},ImageSize
        −>Large]
    }]
  ,
  (*Plot  fitting  function and measured points in bode plot*)
  Show[{Plot[{Log[−Im[Zsym0/.parameterlist2]],Log[−Im[Zasym0/.
      parameterlist2]]},{w,Log[fsym[[fdrop1]]],Log[fsym[[nsym]]]},PlotRange
      −>All,ImageSize−>Medium,AxesLabel−>{”Ln(w)”,”−Arg(Z)”}],
      ListPlot[{Transpose[{Log[Take[fsym,{fdrop1,nsym}]],Log[−Im[Take[
      impedancesym,{fdrop1,nsym}]]]}],Transpose[{Log[Take[fasym,{fdrop1,
      nasym}]],Log[−Im[Take[impedanceasym,{fdrop1,nasym}]]]}]},
      PlotRange−>All,Joined−>True,Mesh−>Full] }],
  Sqrt[Relectron0/Rredox0]*lfree /.parameterlist2,
  Sqrt[Rion0/Rredox0]*lmetal /.parameterlist2
  (*Manipulate the parameters of the  fitting  function*)
```

```
},{{Plotrange,5},3,7},{{Cchem,Cchem0/.pl},(Cchem0/.pl)/3,(Cchem0/.pl)
    *3},{{Relectron,Relectron0/.pl},(Relectron0/.pl)/3,(Relectron0/.pl)*3},{{
    Rredox,Rredox0/.pl},(Rredox0/.pl)/3,(Rredox0/.pl)*3},{{Rion,Rion0/.pl
    },(Rion0/.pl)/3,(Rion0/.pl)*3},{{Rint,Roffset/.pl},(Roffset/.pl)/3,(Roffset
    /.pl)*3},{{Csub,Cint0/.pl},(Cint0/.pl)/3,(Cint0/.pl)*3}]
```

### A.2.3 DC-curve evaluation from a Winchem measurement

A DC-measurement, carried out with Winchem, or similar software, using stepwise increase in voltage with a large number of samples per voltage step will produce a very large output file. This worksheet will reduce the primary measurement log to the current-voltage points at the end of each voltage step.

```
clear;

ncolumns = 3;   %number of columns in the input file
column_i = 2;
column_u = 3;
U_step = 0.05;  % step height of a voltage jump
R_offset = 0;  %offset resistance (for example electrolyte)
    to determine effective overpotential of the cell

    inputfilename = 'Reines_DC\dc_au.txt';  % Input-
       filename, relative path from source file - input
       file may contain header lines
    outputfilename = 'DC_out.txt';     % Output file
       consists of two columns, U and I
    in=fopen(inputfilename,'r');
ndata = 0;
    while(1)
        strline = fgets(in,300);
        if(strline == -1) % when EOF is reached, break
            break;
        end
        row = sscanf(strline,'%g',[1,ncolumns]);
        if(length(row)==ncolumns)     % only rows with
            ncolumns numerical values are treated as data
            points
            ndata=ndata+1;
            current(ndata)=row(column_i);
            voltage(ndata)=row(column_u);
        end
    end

    fclose(in);
```

```
voltage = medfilt1(voltage,3); % avoiding artefacts from
    single point zeroes, that sometimes occur in winchem
    measurements
current = medfilt1(current,3);
npoints = 0;
stepstart = 2;
for i = 2: length(voltage)-1
     if(abs(voltage(i+1)-voltage(i-1))>U_step/3 && (i-
         stepstart)>5)   % voltage jump at point i
          npoints=npoints+1;
          width(npoints) = i-stepstart;
          U(npoints)=mean(voltage(round(stepstart+0.7*width(
              npoints)):i-2));       % the mean of the last
              data points per voltage set is taken
          I(npoints)=mean(current(round(stepstart+0.7*width(
              npoints)):i-2));
          Uramp(npoints,1:width(npoints)-1)=voltage(stepstart
              +2:i);                   %Uramp,Iramp: time-
              evolution of the current at a specific voltage
              set point
          Iramp(npoints,1:width(npoints)-1)=current(stepstart
              +2:i);
          I_error(npoints) = (Iramp(npoints,width(npoints)-3)
              -Iramp(npoints,round(width(npoints)*0.7)))/I(
              npoints); %relative error
          stepstart = i;
     end
end

U_corr = U - R_offset*I;

cyclestart(1) = 1;
ncycles = 1;
for i = 2:npoints -1
     if(abs(U(i))<abs(U(i-1)) && abs(U(i)) < abs(U(i+1)) &&
         abs(U(i)) < U_step && U(i+1) - U(i) > 0 && i-
         cyclestart(ncycles) >3)
          ncycles = ncycles+1;
          cyclestart(ncycles) = i;
     end
end

U_I = [U_corr;I];    %Write U/I data into ascii file
out = fopen(outputfilename,'w');
fprintf(out,'%g\t%g␣\n',U_I);

plot(U,I, '--ks','MarkerSize',3,'LineWidth',2)
xlabel('Voltage[V]')
ylabel('Current[A]')
```

```
title('DC-measurement')
fclose(out);
```

### A.2.4 Extracting the DC-values from a DC-polarised impedance measurement

When DC-polarised impedance measurements are carried out, the impedance functions can be batch-fitted with ZView, but the DC-characteristics are not logged in the file. With this worksheet, the DC-characteristics of subsequently numbered impedance measurement files can be logged.

```
clear;
% Set parameters of the measurement file
basename = 'datafiles\microdc\DATA_';
ncolumns = 5;
column_i=5;
column_u=4;
column_zr=2;
column_zi=3;
column_f=1;

roffset = 30000; % the voltage drop over roffset will be
    subtracted from the cell polarisation
filestart = 0; % files have to be numbered from filestart
    to fileend
fileend = 72;
pointnumber = 1;
for filenumber = filestart:fileend %subsequently read the
    impedance files
     filename = strcat(basename,sprintf('%d',filenumber),'.
         TXT');
     in=fopen(filename,'r');

     ndata = 0;

     while(1)
          strline = fgets(in,300);
          if(strline == -1) % equiv. to EOF
               break;
          end
          row = sscanf(strline,'%g',[1,ncolumns]);
          if(length(row)==ncolumns) % rows with ncolumns
               numerical values contain measurement information
               ndata=ndata+1;
               current(ndata)=row(column_i);
               voltage(ndata)=row(column_u);
               %z_comp(ndata)=complex(row(column_zr),row(
                    column_zi));
               %frequency(ndata) = row(column_f);
```

```
            end
        end

        fclose(in);
        % only the mean DC current and voltage of each
            impedance file are relevant
        I(pointnumber) = mean(current((ndata-10):ndata));
        U(pointnumber) = mean(voltage((ndata-10):ndata))-
            roffset*I(pointnumber);
        pointnumber = pointnumber+1;
end

blabla = [U;I];

out = fopen('dcmicro.txt','w');

fprintf(out,'%g\t%g␣\n',blabla);
fclose(out);
```

## A.3 Impedance functions of the derived equivalent circuits

### Impedance function for micro-finger electrodes deposited above the metal grid

$$\text{Zsym} = \text{Rysz} + \frac{1}{i\,\text{Cdl}\,\omega + \frac{\sqrt{\text{Rion}\left(\frac{1}{\text{Rredox}}+i\,\text{Cchem}\,\omega\right)}\ \text{Tanh}\left[\text{b}\sqrt{\text{Rion}\left(\frac{1}{\text{Rredox}}+i\,\text{Cchem}\,\omega\right)}\right]}{\text{Rion}} + \frac{\sqrt{\text{Relectron}\left(i\,\text{Cint}\,\omega+\frac{1}{\text{Rint}+\frac{1}{\frac{1}{\text{Rredox}}+i\,\text{Cchem}\,\omega}}\right)}\ \text{Tanh}\left[\text{l}\sqrt{\text{Relectron}\left(i\,\text{Cint}\,\omega+\frac{1}{\text{Rint}+\frac{1}{\frac{1}{\text{Rredox}}+i\,\text{Cchem}\,\omega}}\right)}\right]}{\text{Relectron}}}$$

$$\text{Zasym} = \frac{1}{i\,\text{Cdl}\,\omega + \frac{\sqrt{\text{Relectron}\left(i\,\text{Cint}\,\omega+\frac{1}{\text{Rint}+\frac{1}{\frac{1}{\text{Rredox}}+i\,\text{Cchem}\,\omega}}\right)}\ \text{Coth}\left[\text{l}\sqrt{\text{Relectron}\left(i\,\text{Cint}\,\omega+\frac{1}{\text{Rint}+\frac{1}{\frac{1}{\text{Rredox}}+i\,\text{Cchem}\,\omega}}\right)}\right]}{\text{Relectron}} + \frac{\sqrt{\text{Rion}\left(\frac{1}{\text{Rredox}}+i\,\text{Cchem}\,\omega\right)}\ \text{Tanh}\left[\text{b}\sqrt{\text{Rion}\left(\frac{1}{\text{Rredox}}+i\,\text{Cchem}\,\omega\right)}\right]}{\text{Rion}}}$$

Figure A.1: Impedance functions for micro-finger electrodes deposited above the metal grid. Zsym and Zasym refer to symmetric and asymmetric applied voltage.

### Impedance function for micro-finger electrodes with metal grid on top

$$\text{Zsym} = \text{RYSZsym} + \frac{1}{\frac{\text{Cchem0}\,\text{lmetal}\,\omega}{-i+\text{Cchem0}\,\text{Roffset}\,\omega} + \frac{\sqrt{\frac{\text{Relectron0}}{\text{Roffset}+\frac{1}{\text{Ychem0}+i\,\text{Cchem0}\,\omega}}}\ \text{Tanh}\left[\text{lfree}\sqrt{\frac{\text{Relectron0}}{\text{Roffset}+\frac{1}{\text{Ychem0}+i\,\text{Cchem0}\,\omega}}}\right]}{\text{Relectron0}}}$$

$$\text{Zasym} = \frac{1}{\frac{\text{Cchem0}\,\text{lmetal}\,\omega}{-i+\text{Cchem0}\left(\text{Roffset}+\text{lmetal}\,\text{RYSZasym}\right)\omega} + \frac{\sqrt{\frac{\text{Relectron0}}{\text{Roffset}+\frac{1}{\text{Ychem0}+i\,\text{Cchem0}\,\omega}}}\ \text{Coth}\left[\text{lfree}\sqrt{\frac{\text{Relectron0}}{\text{Roffset}+\frac{1}{\text{Ychem0}+i\,\text{Cchem0}\,\omega}}}\right]}{\text{Relectron0}}}$$

Figure A.2: Impedance functions for micro-finger electrodes with metal grid on top. Zsym and Zasym refer to symmetric and asymmetric applied voltage.

# References

[1] W. Dürrschmidt, M. van Mark, “Hintergrundinformationen zum EEG-Erfahrungsbericht 2007,” tech. rep., Bundesministerium für Umwelt, Naturschutz und Reaktorsicherheit, 2007.

[2] T. M. Letcher, *Future energy: improved, sustainable and clean options for our planet.* Elsevier Science Limited, 2008.

[3] EG and G Technical Services, Inc. , *Fuel Cell Handbook*, vol. 7. U.S. Department of Energy, 2004.

[4] N. Q. Minh, “Solid oxide fuel cell technology - features and applications,” *Solid State Ionics*, vol. 174, no. 14, pp. 271 – 277, 2004.

[5] M. C. W. N. Q. Minha, S. C. Singhal, “Solid Oxide Fuel Cells: Development Activities, Trends and Technological Challenges,” *ECS Transactions*, vol. 17(1), pp. 211–219, 2009.

[6] X. Yue and J. T. S. Irvine, “Impedance Studies on LSCM/GDC Cathode for High Temperature $CO_2$ Electrolysis,” *Electrochemical and Solid-State Letters*, vol. 15, pp. B31–B34, 2012.

[7] S. Tao and J. T. S. Irvine, “Synthesis and Characterization of $(La_{0.75}Sr_{0.25})Cr_{0.5}Mn_{0.5}O_{3-\delta}$ , a Redox-Stable, Efcient Perovskite Anode for SOFCs,” *Journal of the Electrochemical Society*, vol. 151, pp. A252–A259, 2004.

[8] W. Chueh, Y. Hao, W. Jung, and S. Haile, “High electrochemical activity of the oxide phase in model ceria-Pt and ceria-Ni composite anodes,” *Nature Materials*, vol. 11, pp. 155–161, 2012.

[9] W. Jung and H. L.Tuller, “Investigation of Cathode Behavior of Model Thin-Film $SrTi_{1-x}Fe_xO_{3-\delta}$ (x = 0.35 and 0.5) Mixed Ionic-Electronic Conducting Electrodes,” *Journal of The Electrochemical Society*, vol. 155, pp. B1194–B1201, 2008.

[10] R. Merkle and J. Maier, “Oxygen incorporation into Fe-doped $SrTiO_3$: Mechanistic interpretation of the surface reaction,” *Phys. Chem. Chem. Phys.*, vol. 4, pp. 4140–4148, 2002.

[11] W. Jung and H. L.Tuller, “A New Model Describing Solid Oxide Fuel Cell Cathode Kinetics: Model Thin Film $SrTi_{1-x}Fe_xO_{3-\delta}$ Mixed Conducting Oxides a Case Study,” *Advanced Energy Materials*, vol. 1, no. 6, pp. 1184–1191, 2011.

[12] VDI-Wärmeatlas, *VDI-Wärmeatlas. Berechnungsunterlagen für Druckverlust, Wärme- und Stoffübergang.* Springer, Berlin, 10., bearb. u. erw. a. ed., 2006.

[13] R. Merkle and J. Maier, “How Is Oxygen Incorporated into Oxides? A Comprehensive Kinetic Study of a Simple Solid-State Reaction with $SrTiO_3$ as a Model Material,” *Angewandte Chemie International Edition*, vol. 47, no. 21, pp. 3874–3894, 2008.

[14] B. Raveau, A. Maignan, and V. Caignaert, “Spectacular Giant Magnetoresistance Effects in the Polycrystalline Perovskite $Pr_{0.7}Sr_{0.05}Ca_{0.25}MnO_{3-\delta}$,” *Journal of Solid State Chemistry*, vol. 117, no. 2, pp. 424 – 426, 1995.

[15] J. Maier, *Physical chemistry of ionic materials: ions and electrons in solids.* Wiley, 2004.

[16] F.A. Kröger, *Chemistry of Imperfect Crystals.* Svets and Zeitlinger, 1964.

[17] J. Summhammer, “Physik der Solarzelle.” Skriptum zur Vorlesung 141.126.

[18] M. S. M. Mosleh and P. Hendriksen, “Kinetics and Mechanisms of Oxygen Surface Exchange on $La_{0.6}Sr_{0.4}FeO_{3-\delta}$ Thin Films,” *Journal of the Electrochemical Society*, vol. 156, no. 4, pp. B441–B457, 2009.

[19] J. H. Park and R. N. Blumenthal, “Electronic Transport in 8 Percent $Y_2O_3 - ZrO_2$,” *Journal of the Electrochemical Society*, vol. 136, pp. 2867–2876, 1989.

[20] M. Rothschild, W. Menesklou, H. L. Tuller E. Ivers-Tiffée, “Electronic Structure, Defect Chemistry, and Transport Properties of $\mathrm{SrTi_{1-x}Fe_xO_{3-\delta}}$ Solid Solutions,” *Chemistry of Materials*, vol. 18, no. 16, pp. 3651–3659, 2006.

[21] J. Jamnik and J. Maier, “Generalised equivalent circuits for mass and charge transport: chemical capacitance and its implications,” *Phys. Chem. Chem. Phys.*, vol. 3, pp. 1668–1678, 2001.

[22] International Centre for Diffraction Data, Newtown Square, PA, USA, *ICDD (2010). PDF-4+ 2010 (Database), edited by Dr. Soorya Kabekkodu.*

[23] E. Koep, C. Compson, M. Liu, and Z. Zhou, “A photolithographic process for investigation of electrode reaction sites in solid oxide fuel cells,” *Solid State Ionics*, vol. 176, no. 12, pp. 1 – 8, 2005.

[24] T. Huber, “Konstruktion einer Vakuum-Mikrokontaktapparatur und Impedanzmessungen an mikrostrukturierten Platin- und Nickelelektroden auf Yttrium stabilisiertem Zirconiumoxid in Wasserstoff Atmosphre,” Master’s thesis, Vienna University Of Technology, 2010.

[25] J. Fleig, J. Jamnik, and J. Maier , “Inductive Loops in Impedance Spectroscopy Caused by Electrical Shielding,” *Journal of the Electrochemical Society*, vol. 143, pp. 3636–3441, 1996.

[26] J. Fleig, M. Kubicek, S. Huber, M. Ahrens, K. Langer-Hansel, M. Gerstl, H. Hutter , “Ion Transfer and Ion Transport in Thin Oxide Films Investigated by Complementary Tracer Diffusion and Impedance Spectroscopy Measurements ,” *ECS Transactions*, vol. 43, pp. 203–212, 2012.

[27] J. Fleig and F. S. Baumann and V. Brichzin and H.-R. Kim and J. Jamnik and G. Cristiani and H.-U. Habermeier and J. Maier, “Thin Film Microelectrodes in SOFC Electrode Research,” *Fuel Cells*, vol. 6, no. 3-4, pp. 284–292, 2006.

[28] J. Fleig, “The grain boundary impedance of random microstructures: numerical simulations and implications for the analysis of experimental data,” *Solid State Ionics*, vol. 150, no. 12, pp. 181 – 193, 2002.

[29] A. Opitz, *Oxygen Exchange Pathways of Platinum Model Electrodes on Yttria-stabilised Zirconia.* PhD thesis, Vienna University of Technology, 2011.

[30] W. Demtröder, *Demtröder Experimentalphysik 2 Elektrizität und Optik.* Springer, Berlin, 4. auflage ed., 2006.

[31] J. Fleig, “On the current-voltage characteristics of charge transfer reactions at mixed conducting electrodes on solid electrolytes,” *Phys. Chem. Chem. Phys.*, vol. 7, pp. 2027–2037, 2005.

[32] M.G.H.M. Hendriks, J.E. Elshof , H.J.M. Bouwmeester, H. Verweij, “The electrochemical double-layer capacitance of yttria-stabilised zirconia,” *Solid State Ionics*, vol. 146, pp. 211–217, 2002.

[33] F. S. Baumann, J. Fleig, M. Konuma, U. Starke, H. U. Habermeier, J. Maier, “Strong Performance Improvement of $La_{0.6}Sr_{0.4}Co_{0.8}Fe_{0.2}O_{3\delta}$ SOFC Cathodes by Electrochemical Activation,” *Journal of the Electrochemical Society*, vol. 152, pp. A2074–A2079, 2005.